공학박사학위논문

불꽃점화 엔진에서의 난류 특성 예측을 위한 물리기반 준차원 텀블 모델 개발

Development of a Physics-Based Quasi-Dimensional Tumble Model for Predicting Turbulence Characteristics in Spark-Ignition Engines

2019년 8월

서울대학교 대학원

기계항공공학부

김 이 룹

불꽃점화 엔진에서의 난류 특성 예측을 위한 물리기반 준차원 텀블 모델 개발

Development of a Physics-Based Quasi-Dimensional Tumble Model for Predicting Turbulence Characteristics in Spark-Ignition Engines

지도교수 송 한 호

이 논문을 공학박사 학위논문으로 제출함

2019 년 4 월

서울대학교 대학원
기계항공공학부
김 이 룹

김이룹의 공학박사 학위논문을 인준함

2019 년 6 월

위 원 장 : 민 경 덕

부위원장 : 송 한 호

위　　원 : 도 형 록

위　　원 : 한 동 희

위　　원 : 박 성 욱

Abstract

Development of a Physics-Based Quasi-Dimensional Tumble Model for Predicting Turbulence Characteristics in Spark-Ignition Engines

Yirop Kim

Department of Mechanical Engineering

The Graduate School

Seoul National University

A variety of new technologies for internal combustion engines have been and are being developed in response to the fuel economy regulations that are being stringent. In order for these new technologies to be applied with their maximum utility, the optimization of engine design, as well as driving strategies for each operating condition, should be preceded. Such optimization can be a very demanding and time-consuming process to be implemented experimentally, especially when so many interactive technologies are involved, thus utilization of simulation is essential for practical optimization. The one-dimensional (1D) simulation model is suitable for this purpose because it can analyze the operation of the overall engine system at high computation speed. In 1D models, the in-cylinder phenomena, which dominates

the engine performance, are simulated by a zero-dimensional (0D) model. However, the 0D model cannot predict the performance of yet-developed engines because it generally has a high dependency on the correction factors and requires an engine-specific calibration process for proper operation.

In order for the 0D model to be predictive, it should be improved to reflect the physics associated with in-cylinder phenomena through a more physical approach. Among others, the turbulence characteristics are the key factors to be captured for accurate prediction because they have a decisive influence on the flame propagation speed, heat transfer rate and mixing quality in spark-ignition (SI) engines. In recent years, it has been an industrial trend to utilize the tumble for turbulence enhancement. Therefore, it is important that the model can adequately predict the tumble flow, which can be sensitively manipulated by the engine design and the operating strategy.

The objective of this study was to develop a 0D model that predicts the tumble flow of a given engine without engine-specific calibration, as well as the corresponding turbulence characteristics. First, the tumble generation model is developed based on the phenomenological investigation of intake flow behavior after introduced. The tumble strength is estimated in the conventional model by applying the tumble coefficient to the total incoming flow rate, and this requires a flow measurement experiment to obtain the tumble coefficient. In the present study, it was attempted to replace this tumble coefficient by reflecting the fact that a stronger tumble is formed when the valve flow is concentrated towards a particular direction. A new approach using a steady-state three-dimensional computational fluid dynamics (3D CFD) simulation is proposed to characterize a specific cylinder head design, and the obtained valve flow characteristics are applied to the 0D model, allowing the consideration of the individual influence of flows in different directions.

To model the generated tumble being transformed into turbulence, a velocity field is assumed within the given combustion chamber geometry and the turbulence production rate by the internal shear is coupled with the tumble decay rate, rather than employing correction factors. A modified velocity profile has been proposed to more precisely reproduce the actual in-cylinder flow structure, and a more realistic combustion chamber geometry is also reflected in the model calculations.

The developed tumble model is combined with the standard k-ε model to complete the 0D turbulence model. The final model is validated with the 3D model, and the results suggest that the developed model can successfully predict the tumble and turbulence behavior under variations of the engine design and operating conditions, at a single calibration point. In addition, validation with experimental data was also performed. For a total of 194 experimental points with various engine design, engine speeds, loads, and valve timings, the correlation between the model predicted turbulence and the measured combustion duration could sufficiently be represented by a single fitting curve.

As a practical model that takes into account for core physics associated, the final product of the present study is expected to assist the design optimization by predicting the effect of design modification, and further, to serve as a part of the virtual engine.

Table of Contents

List of Figures

vi

List of Tables

Nomenclature

A	area
a	pentroof slope
B	cylinder bore
CA10, CA50, CA90	10, 50, 90% burn angle
C_T	tumble coefficient
C_{KE}, C_α, C_β, C_3, C_{out}	model constants
D_{IV}	intake valve diameter
E	kinetic energy
H	cylinder height
h, w	vertical/horizontal distance from tumble center
I	moment of inertia
K	non-tumble mean kinetic energy
k	turbulent kinetic energy
L	angular momentum
L_g	geometric length scale
L_{IV}	intake valve lift
$\dot{m}$	mass flow rate
n_d	number of divisions
P	pressure
P_k	TKE production from non-tumble MKE
P_ε	dissipation production from non-tumble MKE
R	gas constant
R	cylinder radius

R_f	flame radius
r	moment arm length
$S_T,\ S_L$	turbulent and laminar flame speed
T	temperature
T	torque
$U_x,\ U_y,\ U_z$	axial velocities
U	characteristic velocity
u'	turbulent intensity
V	volume
v	velocity

Greek Letters

β	pentroof angle
ε	dissipation rate
$\phi,\ \theta$	flow angles
ν_T	turbulent viscosity
ρ	gas density
Ψ	term related to tumble decay
ω	angular speed

Subscripts

1050	averaged value over CA10-50
eff	effective
i	division number

non	non-tumble
pent	pentroof
rot	rotational

<u>Abbreviations</u>

0D/1D/3D	zero-, one-, and three-dimensional
BD	burn duration
BDC	bottom dead center
CAD	crank angle degree
CFD	computational fluid dynamics
EGR	exhaust gas recirculation
GMEP	gross indicated mean effective pressure
IVO/IVC	intake valve open/close
MFB	mass fraction burned
MKE	mean kinetic energy
RMF	residual mass fraction
TDC/fTDC	top dead center/firing top dead center
TKE	turbulent kinetic energy
VO	valve overlap

Chapter 1. Introduction

1.1. Background

The internal combustion engine is an energy conversion device that converts the chemical energy in fuel into useful mechanical work. The engine is basically driven in such a way that a mixture of fuel and oxidizer (e.g. air) is burned, and high-temperature, high-pressure combustion gases push the piston to produce mechanical work. The internal combustion engine, which has been developed for commercial use since the late 19th century, has been steadily developed for over 150 years and made a great contribution to the transportation sector. However, environmental problems of internal combustion engines have recently been raised due to the problem of environmental pollution.

Figure 1.1 shows the global trend of CO_2 emissions since 1751. This consistent increase of CO_2 emission is considered to be the main cause of climate change, and efforts are being made worldwide to raise awareness and improve this problem. Unlike the last Kyoto Protocol, which imposed sanctions on developed countries only, the Paris Agreement in 2015 obliged all 195 countries, including developing countries, to participate in greenhouse gas reduction, aiming for temperature increase from before industrialization to be within 2 degrees by 2100.

Petroleum-based fuels used in internal combustion engines have a high energy density and are advantageous in that they can be easily transported and stored because they are liquid at ambient condition. However, it contains carbon in its molecular structure, which inevitably generates CO and CO_2 during the oxidation process.   shows the share of greenhouse gas emissions from each sector of OECD

member countries in 2016 [1]. Transportation accounts for over one-fourth of the total CO_2 emissions, inferring the importance of GHG cut-off from internal combustion engine operations.

Figure 1.3 shows the past performance, the current enacted target, and the projected target of CO_2 emission and fuel consumption by different countries. Although there exists some difference in the extent, it is evident the mutual interest in emission reduction and corresponding regulation being made.

With the introduction of BEV owing to the development of energy storage technology, the diesel gate was sufficient to drive the attention of the next generation powertrain to electricity. However, while it is true that electric cars and fuel cell vehicles emit zero tailpipe emissions, it can not be overlooked that GHG occurs in the process of making energy sources (electricity generation) and hydrogen (reforming, electrolysis, by-product hydrogen, etc.). Elgowainy [2] compared the life cycle emissions of HEV, BEV, FCEV, and ICEV, and Choi [3] conducted a case study on Korea for the analysis of oil-importing countries. As a result of these LCA studies, ICE is considered to be still competitive. In particular, because EVs have disadvantages in terms of energy density (power density capability), hybrid vehicles are regarded as the most suitable technology for the transition period. In addition, ICE is considered to be far ahead of electricity or hydrogen fuel cell vehicles in terms of the infrastructure. Therefore, in the future, the internal combustion engine will still be a large part, and continuous efforts for low-emission, high-efficiency are required.

Annual CO₂ emissions by world region

Annual carbon dioxide (CO_2) emissions measured in billion tonnes (Gt) per year

Note: Emissions data have been converted from units of carbon to carbon dioxide (CO2) using a conversion factor of 3.67. Regions denoted "other" are given as regional totals minus emissions from the EU-28, USA, China and India. Here, we have rephrased the general term "bunker (fuels)" as "international aviation and maritime transport" for clarity.

Figure 1.1 Global trend of CO_2 emissions [1]
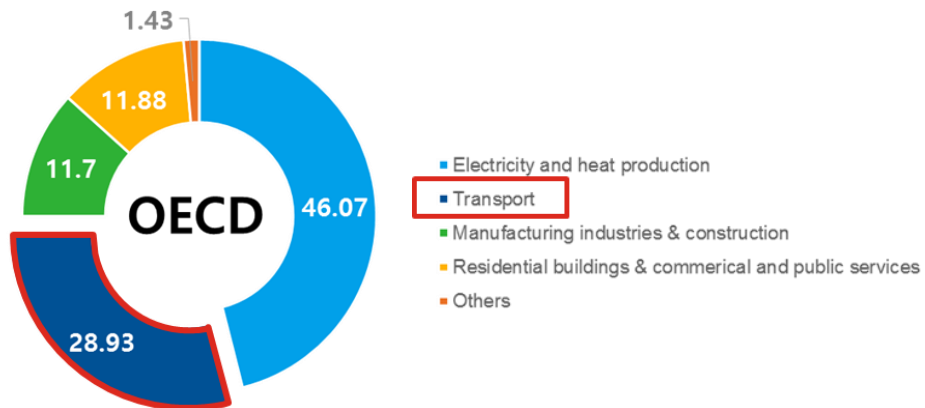
Figure 1.2 Greenhouse gas emission by sector of OCED members (2016)

Passenger car CO$_2$ emissions and fuel consumption, normalized to NEDC
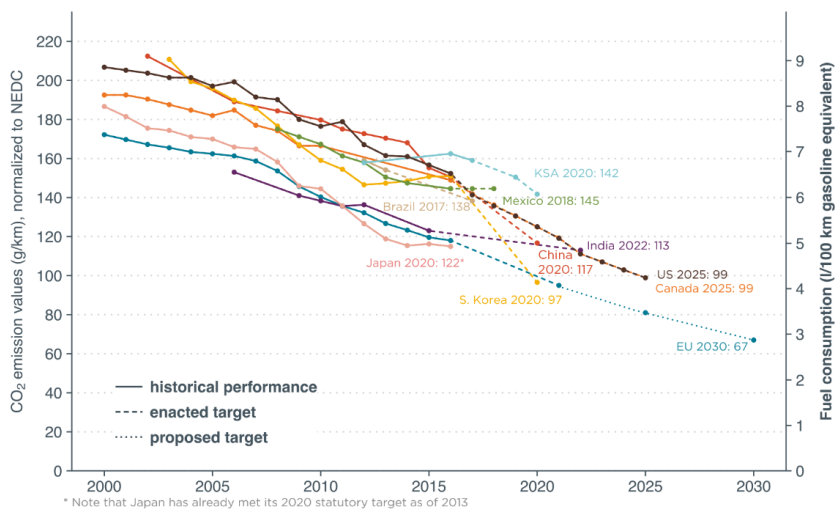
Figure 1.3 Passenger car CO$_2$ emissions and fuel consumption, normalized to NEDC [4]

1.2. Motivations

1.2.1. Recent engine technologies

<u>Boosting and downsizing</u>

Intake boosting using a turbocharger can raise the torque and power at the same displacement volume by increasing the density of the intake charge. Also, the equivalent performance can be achievable with a smaller engine when combined with downsizing. The downsized boosted engines have advantages over naturally-aspirated engines, especially for the friction loss reduction, and are known to improve the efficiency of the engine by over 10% [5]. Due to such benefit, the turbocharger is being increasingly popular in internal combustion engines. The market share of gasoline turbocharged vehicles in the United States is shown in Figure 1.4, and about 30% of gasoline engines vehicles in 2017 are equipped with a turbocharger according to this statistics [6]. However, there also exists drawbacks. The first is the turbo lag, which is the physical time consumed until the compressed air actually starts to affect the engine operation. The turbo lag is problematic especially in low load conditions, and the rotating inertia of the turbine blades is deemed to be the major cause. Advanced turbocharger with a variable nozzle or geometry has been developed in order to achieve a faster response over the entire engine operation map [7]. Another disadvantage of the turbocharger is that it raises the backpressure. This complicates the gas dynamics in gas exchange, especially when large valve overlap is employed, and it also affects the residual mass fraction, thus changing the combustion characteristics. Recently, 48V mild-hybrid vehicles equipped have also been developed, and the electric supercharger became a quite

attractive substitute for turbochargers as the high-voltage batteries allow sufficient reduction in electric loss [8].

Variable Valve Actuation

The valve actuation strategy, including its timing, lift, and duration, is another key aspect in terms of engine operation, especially in SI engines where throttling is normally utilized to control the engine load. The appropriate throttle angle for a certain work output target is determined by the intake/exhaust valve profile, and the combination of valve profiles and throttling is what determines the internal EGR (i.e. exhaust backflow), the charging efficiency, and the pumping loss, all of which can have a major impact on burn duration and final engine performance. Engines have a wide operating range and the optimal valve actuation strategy is different for each operating point. For example, in low-speed conditions, the intake valve closing (IVC) should occur near TDC in order to prevent the excessive reverse flow of the fresh mixture to the intake manifold. However, a later IVC maximizes the charging efficiency under high-speed conditions due to the "ram effect" caused by the momentum of the incoming charge. In addition, larger valve overlap under partial load conditions increases the internal EGR increases, which reduces the pumping loss while lowering the combustion temperature at the same time. So the presence of burned gas in the fresh mixture can be beneficial in terms of improving emission characteristics, but only within the tolerable range of EGR, beyond which the combustion stability is not guaranteed. Such complexity being involved with the valve actuation, it is inevitable that some inefficiencies do occur in certain operating points if a fixed valve profile is used.

The mechanistic developments of recent decades have increasingly enabled

flexible valve actuation. The variable valve timing (VVT), which can shift the timing by adjusting the cam rotation, allowed manipulating the gas exchange dynamics to be suitable for each operating condition. Although the cam profile itself was kept fixed, VVT was widely adopted (as shown in Figure 1.4) for its capability of pumping loss reduction, knock suppression, and emission characteristics.

In recent years, the further advancement of the technology has allowed a more delicate control of the valve lift as well as its duration. The great potentials of such fully-variable valve train have been demonstrated by many researchers. Takemura showed the variable valve motion being able to achieve low fuel consumption with improved emission characteristics, particularly the hydrocarbon in cold-start [9]. The fully-variable valve train also enables the "unthrottled load control," which can resolve the issue of pumping loss, the intrinsic drawback of the SI engine [10]. Moreover, the individual control of effective compression/expansion ratio can avoid knocking phenomena, and the combination of unthrottled load control and cylinder deactivation (CDA) can produce an additional fuel efficiency gains [11].

1.2.2. The necessity for optimal engine design

When applying the aforementioned modern technologies to the engine, the designs of engine components (e.g. combustion chamber, intake/exhaust port, etc.) must be considered concurrently because they can have a various effect on engine operation. For example, the bore size determines the contact area between the piston ring and the liner, which directly influences the amount of mechanical loss due to friction.

Especially in SI engines, where the combustion is based on the propagation of

the flame, the geometry of the combustion chamber is one of the most important features determining flame sheet area, thus the burning rate. Also, the corresponding geometry of burned gas volume is determinative in the cooling loss as it determines the "wetted area" between the burned gas and chamber wall.

Besides these, the charge motion is another major aspect controlled by engine geometry. The intake port geometry primarily decides how the intake charge is introduced into the cylinder, and the consequent charge motion can cause a notable difference in engine performance, even at the equivalent fuel mass. Additionally, the evolution of the generated charge motion along with the compression process would also be dependent on the combustion chamber geometry.

Such charge motion is very important in SI engine mainly due to its transition into turbulence. Turbulence is a random fluctuation of flow velocity, and interpreted to be produced as a large-scale vortex with kinetic energy is gradually cascaded into smaller vortices. Such turbulence can affect SI engine performance in several ways.

The first reason that turbulence is important in SI engine is its influence on the rate of combustion. These small-scale vortices play a role in wrinkling the flame sheet during the combustion process, which can stretch the reaction area and consequently promote flame propagation. Such faster burn rate can be beneficial in terms of thermal efficiency. Unlike in ideal Otto cycle, the combustion takes place over a finite duration in actual engine operation. Therefore, to maximize the work output, combustion phasing by adjusting the ignition timing is necessary. In general, the maximum break torque (MBT) is achieved when the 50% burn angle (CA50) is within the range of 6 to 9 crank angle degrees after top dead center (CAD aTDC). If the flame propagation speed is slow, ignition timing should be further advanced from the firing TDC, which will increase the compression work (or negative work) due to

8

heat release occurring during the compression stroke. In addition, the slow-burning rate can lead to greater loss in the expansion work as the chemical energy release of the fuel proceeds with a longer volume expansion involved. The loss due to this slow-burning rate is also termed as "time loss", which is graphically described in Figure 1.5. Thus, as the turbulence becomes stronger and the burning rate increases, it becomes more and more close to the constant-volume combustion of the ideal cycle (sometimes expressed as the degree of constant volume), which can increase the thermal efficiency by reducing this time loss.

In addition, sufficient improvement of flame propagation speed is known to mitigate knocking phenomena [12, 13]. Knocking is an abnormal phenomenon in which as the flame propagation proceeds, the temperature and pressure of the end gas rise, and unintended spontaneous ignition occurs. This self-ignition generates a pressure wave to create a knocking sound, which can cause serious damage to the engine depending on its strength. Therefore, knock is a factor that must be avoided, and it is the biggest obstacle to increase the efficiency of the SI engine because it limits the MBT operation as well as the increase of compression ratio. However, if the propagation is completed before the ignition delay of the end gas at a sufficiently fast flame speed, some positive effect on knock mitigation can be expected by not allowing enough dwell time for auto-ignition to occur. In fact, Hirooka et al. induced high turbulent flow by direct injection of high-pressure air, and due to the fast-burning rate, it was possible to extend the lower limit of engine speed for MBT operation. In addition, even under the knock-limited conditions, a 10% engine torque increase was obtained due to the effect of rapid combustion [12]. One thing to notice is that rapid combustion causes a steep increase in temperature and pressure, which shortens the ignition delay. Thus, it is yet to understand whether faster combustion

is always beneficial in regards to knocking resistance.

Furthermore, turbulence enhancement is known to increase the tolerance for exhaust gas recirculation (EGR) rate [13-15]. EGR is exploited to dilute the air-fuel mixture by recirculating the product gas of the combustion. This increases the specific heat capacity of the in-cylinder gas and lowers the flame temperature. In the CI engine, EGR is commonly used to prevent NO_x formation. On the other hand, in SI engine, which is operated at stoichiometric conditions, it is possible to use three-way catalyst (TWC) with high conversion efficiency, so there is relatively less concern about NO_x. However, EGR can be still favorable in SI engines for its capabilities in the reduction of cooling loss due to lowering of combustion temperature, a decrease of pumping loss at partial load, and mitigation of knock by lowering the combustion temperature. Another fact to note is that dilution slows the laminar flame speed, which affects the combustion rate (especially the initial kernel development stage), which can lead to a serious decline in combustion efficiency or even misfire in the worst case. It has been demonstrated by many researchers that turbulence can resolve this combustion instability and increase EGR tolerance. The previous studies by Ogink [14] and Wheeler [15] showed that further emission reductions are possible by improved EGR tolerance, and higher EGR tolerance can also extend the utilization of LIVC or EIVC [16].

Next is how the engine design influences the so-important turbulence. In engine operation, the small-scale vortices, namely turbulence, is originated from the incoming flow induced by piston motion. When the flow is introduced into a constrained volume of the engine cylinder, it soon encounters the boundary wall and creates circular motions [17]. Depending on its direction of rotation, the circular charge motion can be classified as swirl, tumble or cross-tumble (see Figure 1.6). It

10

is important for an engine how the charge motion is built inside the cylinder because even the same amount of intake mass can have different influences on the engine combustion.

Among different types of large-scale motion, tumble possesses several advantageous structural characteristics for turbulence enhancement: (1) Tumble is spontaneously generated with pentroof cylinder head, which is most common for recent four-valve engines, (2) as a relatively stable mean motion, tumble can store a certain amount of the intake kinetic energy, and (3) having rotation axis perpendicular to the cylinder axis, even well-ordered tumble cannot avoid its breakdown into small-scale motions (or turbulence) near the end of compression, at which high turbulence is desired [14, 18-21]. In summary, the intake-generated tumble can preserve the turbulence potential and release it in a timely manner. Hence, tumble motion is increasingly being utilized in modern engines.

1.2.3. Motivations for predictive 0D model development

As modern engines increasingly become diverse and complex in their configuration, component design, and manufacturing process, the optimization process accordingly becomes complicated. For the outcome that is optimal in both efficiency- and emission-wise, it is necessary to choose the technologies to apply, optimize the design of engine components, and evaluate for the best operating strategies. This overall optimization process can be extremely time-consuming. In particular, design optimization requires significant efforts and resources to implement experimentally as it involves the series of fabrication, installation, and

testing of every target design. Although the testing efforts can be reduced by design of experiments (DoE), such an optimization result is based on mathematical fitting, which lacks the physical intuition, and is most likely case-specific.

Hence, the development of a more fundamental but practical approach is encouraged. The simulation model that can reproduce the physical phenomena associated in engine operation would not only save a significant amount of time, effort, and resources but also assist to obtain a better understanding of the phenomena rather than just suggesting the optimal output. Therefore, a model that properly predicts the engine performance with varying operating conditions and geometry modification is needed.

3D CFD model has very high accuracy and provides the results with spatial resolution, allowing detailed investigations on fluid motion. However, despite the continuous advances in computing power, the computation cost of 3D CFD is still very high. Therefore, 3D CFD is not a suitable tool to be utilized for the design optimization process, in which numerous combinations of operating condition and strategy should be examined for various designs.

The 0D model, on the other hand, is far superior to 3D CFD in terms of computation speed, which is why it is widely employed in industrial applications. But the 0D model basically gains its advantage in computation speed at the expense of the accuracy. Due to its structural restriction, the 0D model must involve many assumptions and severe simplifications, which in return, decreases the model accuracy. Although 0D model can promise a reasonable fidelity over a wide range of operating condition, it still requires some calibration process, implying the

absence of the predictability. Thus, it cannot be utilized for the design optimization process, which requires performance prediction of yet-developed engines.

Various efforts have been made in order to improve the predictability of the 0D model, and the extension to the 1D model is one of them. The 1D model simulates the overall fluid flow within the entire engine configuration (from the air in the atmosphere being inhaled into the intake duct to the exhaust gas exits through the tailpipe), and this enables more accurate estimation in the amount and composition of the cylinder gas with an account of detailed flow dynamics.

Figure 1.7 shows the sample 1D model of a full 4-cylinder SI engine, modeled in GT-Power, a commercial 1D model software. As seen in the figure, the 1D model generally consists of numerous blocks, each of which represents a particular component or a part of it. But while the 1D model can include very fine details of flow path geometry, the engine cylinder is still represented by a single block. In other words, even the 1D model solves the in-cylinder phenomena as in 0D, and the purpose of all the blocks other than the 'cylinder' block is primarily for calculating the precise in-cylinder gas properties.

Precise estimation of the mass flow rate is indeed very important, but a reliable prediction about the in-cylinder phenomena (e.g. the in-cylinder flow motion, the combustion, and the heat transfer, etc.) should also follow, as they are crucial in determining the overall engine performance. Thus, it is essential to advance the 0D submodels so the 0D model can also reproduce the in-cylinder phenomena in a predictive manner. And this would be achievable by a more physics-based modeling approach.
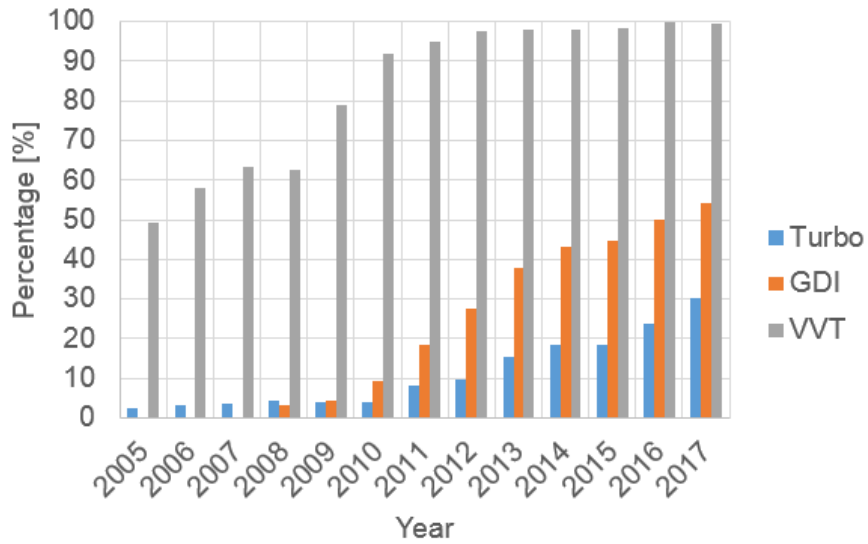
Figure 1.4 Product share of light-duty gasoline engine technologies [6]
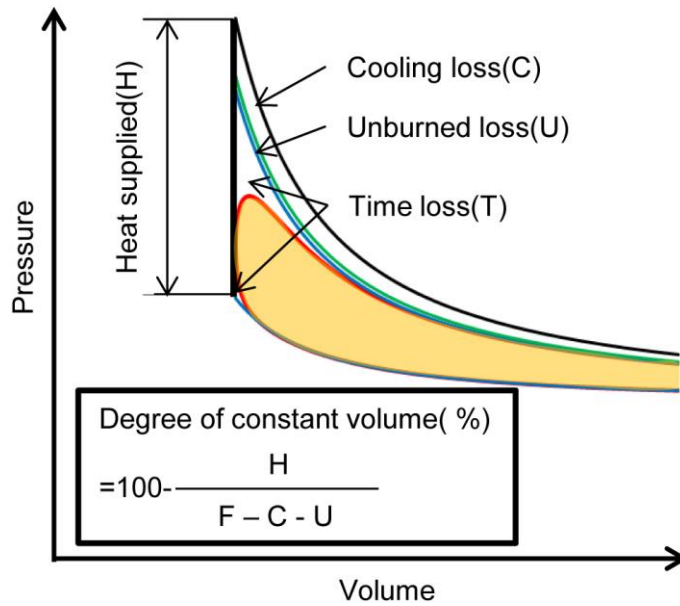
Figure 1.5 Sources of loss within the engine cycle [22]

14
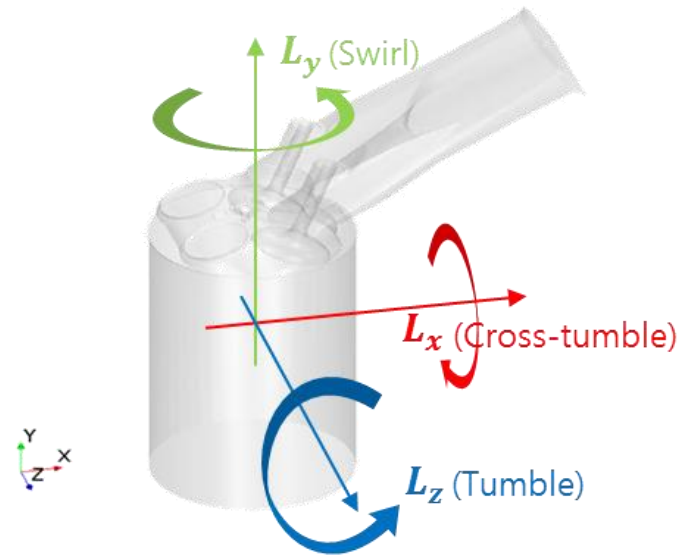
Figure 1.6 Classification of charge motions
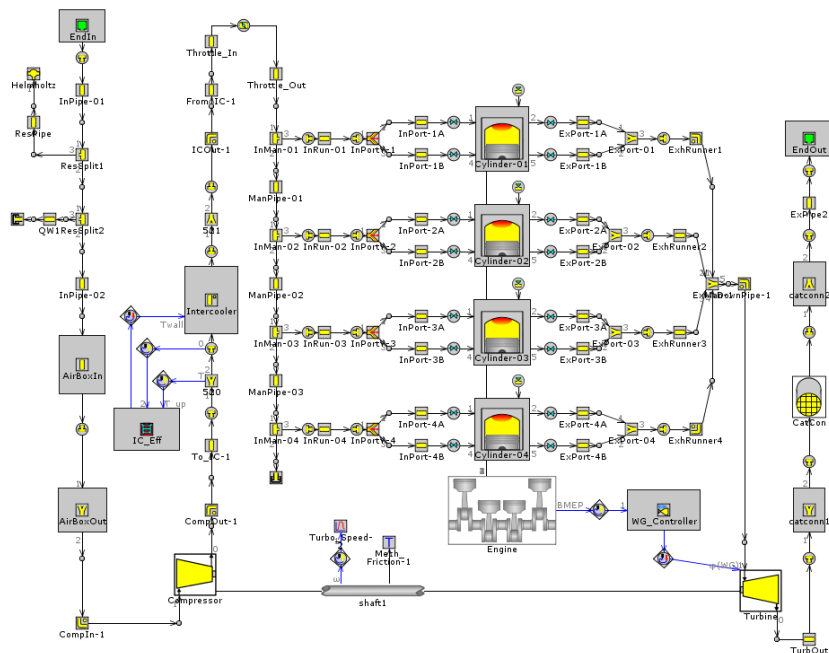
Figure 1.7 1D Model of 4-cylinder turbo direct-injection SI engine

1.3. Literature survey

The simplest way to simulate the combustion process in 0D model is to use a single zone model. In single zone models, the combustion progress of the trapped fuel is prescribed by the Wiebe function. Once the burning curve is defined, the heat release from the combustion can be computed as a function of time, which is then applied to the 1st law of thermodynamics to calculate the performance parameters. The Wiebe function has an S-shaped curve whose shape is determined by the burn duration and the two coefficients, which are calibrated to give the nearest pressure trace from the specific test result. It is difficult for the single-zone model to predict any change of flow dynamics by valve actuation or geometry modification, hence it is usually only used for simple combustion analysis of tested operation.

To overcome such limitations, a multi-zone model can be utilized. In case of SI engine, a two-zone model is used to separate the mass inside the cylinder into the burned and unburned zone in the calculation (sometimes three-zone, including intermediate reacting zone). The multi-zone model possesses the predictive capability as the flame propagation speed and resultant burn rate are modeled as a function of laminar flame speed, turbulent intensity, Taylor microscale, etc. In this type of model, it is assumed that the flame initiated from the spark plug propagates outwardly, generating spherical flame volume enclosed in chamber volume, and the overall burn rate, as well as the transfer rate, is calculated accordingly. It is also referred to as a "quasi-dimensional" (QD) model because it considers dimensional information such as the chamber geometry and location of the spark plug in the calculations.

One of the most popular QD combustion models is the entrainment model (also

called eddy-burning model), which is initially proposed by Blizard and Keck [23]. This model assumes that the flame front propagates at the turbulent flame speed and that the unburned mass entrained within the flame front burns over a characteristic burning time. Also, the turbulent flame speed was supposed to be equivalent to the laminar flame speed at the beginning, and develop to the full turbulent flame speed over a certain time scale. The turbulent flame speed and characteristic length scale need be evaluated for calculation of burn rate, which is simply assumed in this initial model to be proportional to the mean gas inlet velocity and the valve lift, respectively. Flame propagation speed, as mentioned earlier, is in fact closely related to turbulence, but this definition cannot properly account for the effect of turbulence on combustion phenomena. Keck's follow-up research has proposed an empirical formula to correlate cylinder density changes to evaluate these two parameters [24].

Later, Tabaczynski [25, 26] refined the entrainment model. By applying the conservation of angular momentum, he expressed the turbulent intensities and integral length scales after ignition as a function of the density ratio. In addition, the spacing between turbulent vortex tubes described by the Taylor microscale, and the laminar flame speed calculations were improved to reflect the composition of the air-fuel mixture. Through these refinements, the turbulent flame speed could be predicted and the eddy burn-up time could reflect the EGR rate and compression ratio, which granted a better predictive capability to the model. The initial turbulent intensities and integral length scales at the ignition timing are roughly assumed to be proportional to the mean piston speed and the instantaneous chamber height, respectively.

Poulous [27] investigated the effect of chamber geometry and the spark plug location. In this study, simulations of several representative combinations of

17

chamber geometry and spark plug location are implemented and their impacts on combustion behavior are analyzed. This study utilized the advantageous of QD combustion model and demonstrated its strength in predicting the burned mass fraction profile and the additional effect on the heat transfer rate with engine design modifications, however, the effect of the geometry on the charge motions or the subsequent turbulence characteristics were not considered

Since the turbulence has a dominant influence on the calculations in the QD combustion model, its precise prediction is required for high-degree of predictive capability. For this purpose, a turbulent sub-model is employed as a method for predicting turbulence in a more sophisticated manner. The 0D turbulence model can be largely classified into the k-ε model and energy cascade model. The k-ε model is a model that includes compressibility during the compression process and anisotropic behavior of the flow field. Borgnakke [28] calculated the turbulence characteristics in the internal combustion engine by presenting a simplified two-zone k-ε model. In this model, the rate of change in TKE and epsilon are calculated based on the concept of conserving angular momentum of turbulent eddies. Morel [29] proposed correcting the dissipation rate calculation of the standard k-ε model. In this study, the authors modified the dissipation rate equation appropriately for uni-directional compression by referring to combining the fact that the dissipation in spherical compression should be different from that in the engine. Referring to the argument of Reynolds that dissipation in spherical compression should be different, the authors modified the dissipation rate equation to fit the specific situation of uni-directional compression of reciprocating engines. This modified expression is utilized in many engine model studies until recently.

The energy cascade model proposed by Mansouri [30] describes the mean kinetic energy (MKE), representing the large scale motions generated by the intake flow, is cascaded and produce the turbulent kinetic energy. The production rate of TKE is caused by the shearing force, and the internal shear in the flow field is proportional to the velocity gradient. Since no information about the velocity field is given in 0D model calculation, the velocity gradient term is simplified by using the average flow velocity of MKE and geometric length scale

One of the biggest differences between the k-ε model and the energy cascade model is how the dissipation rate is calculated, at which the turbulent kinetic energy is dissipated into internal energy. While the k-ε solves a separate differential equation for ε, the energy cascade assumes an integral length scale and uses it backward to compute the dissipation. The integral length scale can be assumed to be the instantaneous cylinder height for the simplest method [27, 30], or it can be modeled proportionally to $V^{1/3}$ [31, 32]. Further, Kim claimed that the integral length scale comparable to the 3D CFD was obtainable by a more sophisticated correlation based on the analysis of local minimum and maximum of integral length scale [33, 34].

The aforementioned models show the continuous development of the 0D model for the improved predictability. However, it is still true that numerous assumptions are accompanied by state-of-the-art 0D models. It clearly seems insufficient to represent the complex in-cylinder charge motion by only the two terms of MKE and TKE, especially for the modern engines in which the in-cylinder charge motion is manipulated for the purpose of turbulence enhancement. In order to function as a predictive model considering the detailed charge motion in keeping with the modern engine development, it is imperative to encourage the model to capture the associated

19

physics with charge motion, especially the tumble.

For this reason, several researchers have attempted to differentiate the tumble (sometimes swirl, as well) and consider its unique structural characteristics into calculations rather than treating all mean motions as a single variable (MKE) as the general 0D turbulence models do. In order to express the circular charge motion in 0D space, the tumble motion is typically approximated as a solid-body rotation of a single elliptical macro-vortex and to have the vortex center at the geometric center of the cylinder. Then the tumble strength can be represented by the angular momentum of this macro-vortex, and the conservation of angular momentum can be applied.

$$\frac{dL}{dt} = \left(\frac{dL}{dt}\right)_{in} - \left(\frac{dL}{dt}\right)_{out} - \left(\frac{dL}{dt}\right)_{decay}$$ (1.1)

Benjamin [35] was the first to model the decay of the tumble vortex caused by external couples. He prescribed a simple velocity profile to assume the flow field inside the cylinder, and the shear stress acting on the field are calculated. The expressions for the tumble decay rate and the turbulence production rate could be derived as a function of the cylinder dimension.

Dai [36] applied the conservation of the tumble angular momentum and solved for the overall generation of angular momentum and its decaying within the engine cycle. Using the measured torque from the flow bench and calculated the tumble flux induced by intake flow based on the derived tumble coefficient. He noted that the tumble vortex is far from being close to a solid-body rotation as the piston approaches TDC, and suggested correlating the TKE production with the tangential

20

velocity of tumble vortex.

Achuth and Mehta [18], in their calculation of the tumble angular momentum flux, computed the tumble effective velocity component and the effective moment arm considering the pentroof angle and valve seat angle. In addition, to simulate the stronger tumble generation occurs in high valve lift condition, they applied a coefficient to the mass flow rate and distinguished the effective mass flow that contributes to tumble generation. The attempt to reflect the physical phenomena of realistic geometry was worthwhile, but the effective mass flow coefficient was too elementary to be accurate. Also, the pentroof geometry was only applied to the calculation of tumble generation rate, but not the tumble decay rate.

Ramajo [37] adopted the model of Achuth and Mehta and implemented the simulation two different port configurations under part load and full load conditions, which are then compared to the results of 3D CFD. He pointed out that the model does not properly reflect the tumbling enhancement of the port geometry change because it cannot predict the upstream valve flow behavior and has insufficient sensitivity to it. He proposed the velocity distribution obtained from CFD and suggested that the velocity distribution according to the port geometry should be reflected in the calculation of tumble generation. By dividing the curtain area into two zones, a new tumble generation rate equation could be proposed with the supplement of the CFD results. This method was able to reflect the tumble initial build-up trend due to the port shape change but still showed a poor prediction on the tumble and turbulence thereafter.

21

Falfari [38] took a similar approach to Achuth to account for the impact on the incline angle of the tumble port. By correlating this port incline angle, he tried to obtain a tumble-effective tangential velocity. Also, he added a coefficient to the inlet velocity to reflect the velocity loss that occurs when the flow is introduced into the cylinder after passing the valve.

Grasreiner [39-42] developed a turbulence model and a combustion model considering a detailed charge motion for the purpose of virtual calibration of an engine using a fully variable valve train. For the virtual engine calibration, it is important to have a predictive capability that correctly captures the effects of engine operation alteration. Therefore, the Grasreiner aimed to develop a physics-based fast-working model that requires minimal tuning effort. First, the 0D turbulence model was improved to account the tumble and swirl motion simultaneously for the given the valve actuation, then the information needed for the calculations of the tumble generation and decay rate was obtained through 3D CFD [39, 40]. Based on this model, he has been successful in applying the ignition delay kernel model [41] and the overall virtual calibration of the engine [42].

Fogla [43] combined the energy cascade model and k-ε model to K-k-ε model. With this modeling approach, not only the source terms of turbulent kinetic energy and its dissipation rate could be clearly identified, but also eliminated the need for any additional modeling for integral length scale. Here, the effect of tumble motion is accounted by using an additional equation for angular momentum, and thus, the source term includes the TKE production from tumble decay as well as the TKE production from MKE cascade, and compressibility term (RDT).

Bozza [19, 44] has refined the 0D turbulence model through conjoint study with 3D analysis. From the results of 3D CFD, the tumble coefficient was obtained through the analysis of velocity distribution over the given cycle. The computed tumble coefficient, together with discharge coefficient, are utilized as the 0D model input, the results are compared with those of 3D CFD under motored condition. The good agreements were observed with variation of engine speed, compression ratio, and stroke-to-bore ratio, which validated that the 0D model could take into account the effect of intake port orientation.

1.4. Objective

In order to help the optimization of operating strategies and engine design, that are being increasingly complex along with technology developments, a predictive 0D model is desired. Until recently, much progress has been made for the 0D models, however, even the state-of-the-art models rely heavily on engine-specific calibration in calculating the tumble and turbulence characteristics. Such calibration requires the reference experimental data, and since it is an extremely demanding process to go through the entire process of fabrication, installation, and testing, for all engines to be examined, the current 0D models are not suitable for utilization in design optimization.

Therefore, the objective of this study is to develop a predictive 0D turbulence model that can reflect the effects of design modifications as well as various operating strategies. For this particular purpose, the use of adjustable modeling constants is to be eliminated from the calculations by considerations of the flow structure and a more realistic combustion chamber geometry. The resultant physics-based predictive 0D model is expected to be appreciated in the design optimization process, and also, to contribute as a part of a virtual engine.

Chapter 2. Development of Tumble Generation Model

As briefly mentioned in section 1.2.3, the in-cylinder tumble act as a storage for turbulence potential. Hence, the strength of tumble implies how much kinetic energy, namely turbulence potential, is preserved in the large-scale motion. The development of tumble is driven by the incoming flow through the intake valves, and the associated fluid dynamics are strongly influenced by the engine component geometry, especially the intake port. Therefore, it is a key concern that the model has the capability to predict the generation rate of tumble motion correctly.

2.1. Modeling concept

During the induction process, the fresh charge introduced into the cylinder generates the tumble motion. Angular momentum (L) is what is typically used to represent tumble motion in 0D space, and its generation rate by the intake charge $(\dot{L}_{in})$ is estimated by general expression as below in most 0D tumble models found in previous literature [18, 19, 32, 36, 39, 40, 43].

$$\dot{L}_{in} = C_T \dot{m}_{in} v_{in} r \tag{2.1}$$

where C_T, $\dot{m}_{in}$, v_{in}, and r denotes the tumble coefficient, intake mass flow rate, intake flow velocity, and the tumble moment arm, respectively (refer to Figure 2.1 for the schematic). The tumble coefficient is normally obtained by tumble torque measurement from the steady-state flow bench similar to that shown in Figure 2.2. Although this type of measurement itself is not a difficult task in procedure-wise, if any design modifications are made on certain component related to the flow dynamics (e.g. intake port, bore, stroke, etc.), the corresponding tumble coefficient

must be newly found. Repeating the process of fabricating and testing for all the target engines can be highly unfavorable, especially in the design optimization process. In addition, the standard tumble measurement technique is not well-established, which raises difficulties in interpreting the characterized data of others.

Several researches have been conducted to eliminate the dependence of the experimental measurements so that the 0D tumble model can be operated in a predictive manner. Grasreiner utilized a steady-state CFD to find tumble coefficient of given engine geometry [39, 40]. He obtained a characteristic curve by evaluating the quasi-static flow field at each valve lift. Bozza computed the tumble coefficient from by analyzing velocity distribution around the valve from the results of cyclic simulation with 3D CFD [19, 44]. Utilization of CFD is advantageous that the tumble coefficient at each valve lift can be obtained even in the very early stage of the engine development process when only the CAD geometries are available. By comparing the results of 0D and 3D models, both researchers demonstrated their method to be promising in terms of providing appropriate tumble coefficient and predicting the tumble and the subsequent turbulence.

Abovementioned studies focused to measure the tumble coefficient, either experimentally or numerically, and how it affects the charge motion behavior. However, looking into the physical meaning of this equation, the entire intake mass flow is assumed to be introduced at a single inlet point in one identical direction, which is quite far from what actually occurs around the valve. In order to compensate any error from such critical assumption, they adopted a single coefficient C_T. This tumble coefficient basically implies the fraction of linear momentum of intake flow contributed to the generation of tumble angular momentum, but it is not clear how

26

this tumble coefficient is determined. In other words, there lacks in physical intuition how each design parameter affected the tumble motion.

It is thought that a phenomenological approach is needed to develop the capacity of 0D to predict the tumble flow change due to design change without engine-specific investigation on the tumble coefficient. For this purpose, it was visualized how the tumble is created. Modulation of tumble strength can be implemented by altering the head design (eg, straight intake port, intake port angle, valve masking, etc.) or by using some auxiliary device (shrouded valve, tumble flap, etc.). In spite of a variety in the approach, the basic mechanism that enhances the tumble is to change the structure of the flow through the valve. Intake flow through valves have various directions, and there can be an apparent variation of mass flux in each direction, as shown in Figure 2.3.

When the valve curtain area is divided into the upper and lower side as illustrated in Figure 2.4, it can be easily imagined that the flow through the upper side of the valve curtain creates the "forward" tumble. Conversely, the lower side flow creates the "reverse" tumble, which disrupts the forward tumble from being stabilized. Therefore, as more flow is directed, or concentrated, toward the upper side, not only a greater amount of flow contributes to generating the forward tumble, but also less reverse tumble are caused at the same time. The structure of the incoming flow at the valve curtain area is a crucial factor that determines the tumble strength, and it was thought that the tumble generation rate would possibly be estimated if the detailed valve flow characteristics are known.

The quasi-dimensional approach can be applied to this situation. By "quasi-dimensional," it means to divide the curtain area into several divisions so that each

division represents flow in different directions, and implement further calculations individually. Figure 2.5 illustrates the curtain area divided into eight divisions.

If the flow distribution is known across the divisions, the corresponding mass flow rate and the velocity can be derived. And if the appropriate tumble moment arm is given, the rate of angular momentum generation by each intake flow division can be expressed as:

$$\dot{L}_{in,i} = \dot{m}_i v_{tum,i} r_i \tag{2.2}$$

where i is the division number. Note that the velocity is denoted with subscript tum, meaning it is the tumble-effective velocity. This tumble-effective velocity only consists of xy-component because z-component of velocity rather creates cross-tumble, which should not be counted in this calculation of tumble generation. The cross-tumble is classified as non-tumble mean kinetic energy, which will be further discussed in section 4.1.

Figure 2.6 visually explains the concept of QD approach. Here,

- The valve curtain area is evenly divided into eight divisions

- The center points of each division surface are assigned to be the representative flow inlet point. This allows the flow inlet points to reflect various features such as the pentroof angle, valve diameter, and valve lift.

- The location of tumble center is assumed to be the midpoint of total chamber height, which continuously changes over the engine cycle along with piston motion.

- Tumble moment arms are the perpendicular distance between the flow velocity and the tumble center. It is determined by the locations of inlet point and the tumble center, as well as the flow angle θ, so take into

28

account the combustion chamber geometry and the valve actuation strategy.

Since the tumble motion is treated as a single unidirectional macro-vortex in 0D model, the angular momentum by each divisional flow is aggregated simply as:

$$\dot{L}_{in} = \sum_i \dot{m}_i v_{tum,i} r_i$$

(2.3)

With the QD approach, the intake flow no longer needs to be assumed as a single "chunk," and the detailed valve flow is more physically reflected. This leads to the elimination of the necessity for somewhat ambiguous tumble coefficient. This method does require some new additional information on flow distribution and angles, however, these are supposed to be the intrinsic characteristics of particular head design. Thus, the preliminary task to obtain this additional information would only be needed when modifications are made to the head geometry, which is a huge reduction compared to the engine-specific computation of tumble coefficient.

A similar approach could be found only in the study of Ramajo et al. [37]. Ramajo emphasized the influence of the orientation of incoming velocity and divided the valve curtain into two zones. After simplifying the intake flow into three components, he suggested expressing the total tumble generation rate by the sum of tumble momentum flux of each component. For detailed characteristics of each component, he used the tabulated parameters extracted from the CFD. The results, however, showed inadequate correlation with the cyclic CFD results. The reason for the failure in precise prediction can be the use of inappropriate decay model, but it is also questionable whether the two zones were sufficient to represent the flow directions.

The method presented in this study is reckoned much more advanced than the existing models as it requires much reduced preliminary task and reflects more detailed valve flow characteristics and realistic chamber geometry. This method is expected to be the base of a very practical tool as it is responsive to any design modifications or tumble enhancement techniques. The following sections of this chapter describe the methodology to obtain the necessary information for this newly suggested approach.

Figure 2.1 Sectional view of pentroofed cylinder showing the typical 0D approach of the tumble generation rate estimation
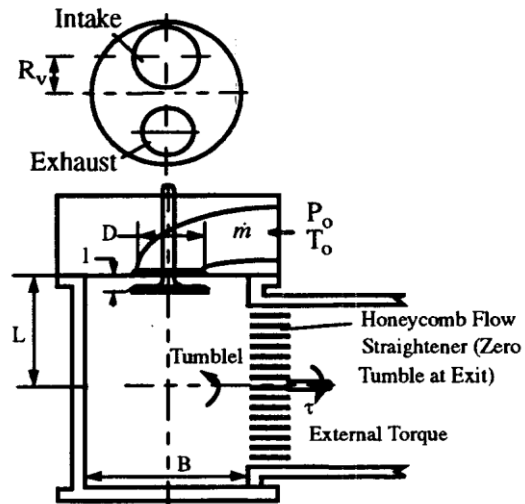
Figure 2.2 Flow bench for tumble torque measurement [36]
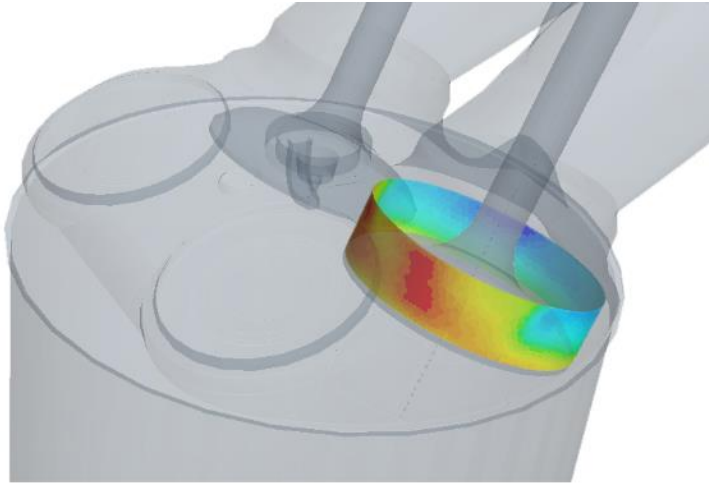
Figure 2.3 Mass flux computed on the valve curtain area

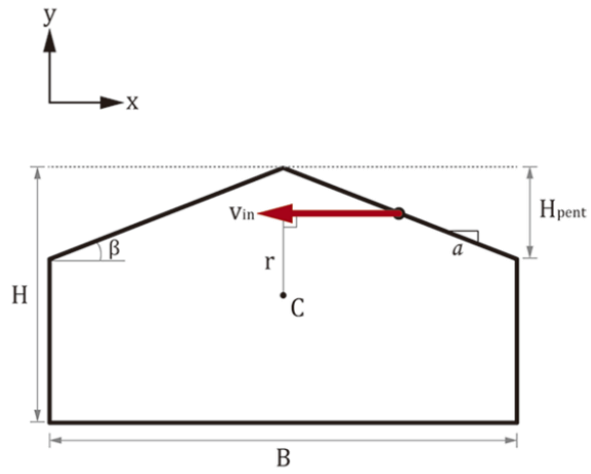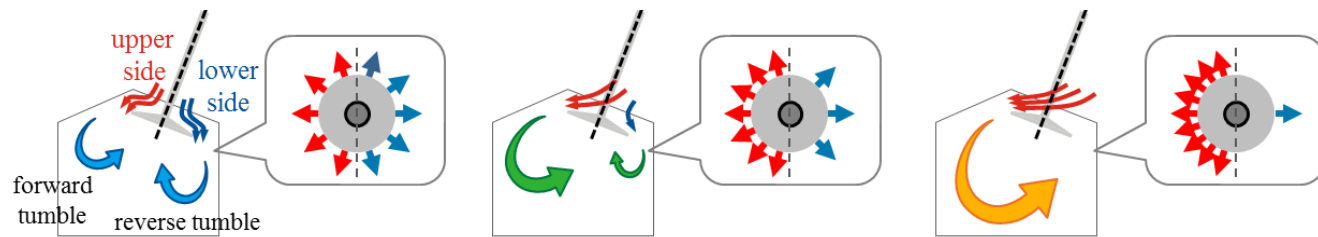Figure 2.4 Mass flux distribution and the tumble strength

Figure 2.5 Valve Curtain Area Division

Figure 2.6 Sectional view of pentroofed cylinder showing the QD approach of the tumble generation rate estimation
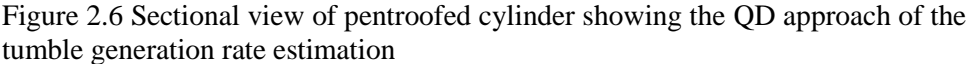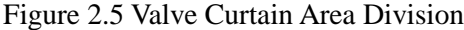
2.2. Head characterization

2.2.1. Simulation setup

As mentioned in the previous section, the flow distribution is deemed to be the characteristic feature of a cylinder head. In order to analyze the detailed flow characteristics across the valve curtain of particular head design, a simple steady-state simulation with 3D CFD is planned. First, the CAD geometry of the target cylinder head is imported in CD-adapco STAR-CCM+, and an elongated cylinder has been attached. Here, the purpose is not to examine the interaction of the flow with the wall surface after introduced nor the flow motion generated in the cylinder, thus the size of the cylinder was not a sensitive matter. The valve curtain area is divided into eight divisions, each of which is set as the measurement plane. Then, the upstream and downstream pressures were assigned as boundary conditions at the end of the intake manifold and elongated cylinder, respectively, and the simulation was continued until it reached a steady state. Figure 2.7 is a snapshot of the simulation.

Figure 2.8 shows the CFD results of the velocity magnitude at low and high valve lifts. Owing to the orientation of the intake port, there exists a sharp edge along the lower side of the flow pathway (circled in the figure). When the flow velocity is sufficiently fast, flow separation is likely to occur at this "cliff" due to the momentum as in Figure 2.8 (right). In case of such flow separation, the momentum of charge naturally leads a highly concentrated flow toward the upper-side and the deficiency in lower-side. This is the major cause of uneven distribution, and the extent of the variance is proportional to the velocity.

The flow velocity is mainly affected by the lift. Figure 2.9 shows the qualitative results on the mass flux on the "unrolled" valve curtain area from the simulations performed with the valve lift increase from 1 to 8 mm. The divisions are consecutively numbered from 1 to 8 that the uppermost divisions being divisions 4 and 5. It can be observed that the mass flux is fairly uniform at lower lifts, but as the valve lift increases, the upper-side remains highly concentrated (red) while the lower-side reveals some region of deficiency (blue). These results provide an intuition of detailed valve curtain flow being introduced into the cylinder, however, is yet too complex to be utilized in the 0D model. Therefore, they need to be further processed into a form friendly to 0D.

2.2.2. The mass flow rate of each division

The results of the mass flux field (previously shown in Figure 2.9) can be computed into the mass flow rates (either the total or of each division), simply by taking the surface-integral. Having the information on the mass flow rate, two 0D-friendly parameters can be extracted: the discharge coefficient and the fractional distribution.

First, the discharge coefficient can be obtained from the total mass flow rate. In 0D engine models, the mass flow rate through the valves is estimated by multiplying the discharge coefficient to the theoretical mass flow rate. The theoretical mass flow rate at given pressure condition and flow area can be calculated by compressible isentropic flow model, which writes as:

$$
\begin{cases}
\dot{m}_{isentorpic} = \dfrac{A_r P_0}{(RT_0)^{\frac{1}{2}}} \left(\dfrac{P_T}{P_0}\right)^{\frac{1}{\gamma}} \left\{ \dfrac{2\gamma}{\gamma-1} \left[1 - \left(\dfrac{P_T}{P_0}\right)^{\frac{\gamma-1}{\gamma}} \right] \right\}^{\frac{1}{2}} & \text{, when unchoked} \\[4ex]
\dot{m}_{isentropic} = \dfrac{A_r P_0}{(RT_0)^{\frac{1}{2}}} \gamma^{\frac{1}{2}} \left(\dfrac{2}{\gamma+1}\right)^{\frac{\gamma+1}{2(\gamma-1)}} & \text{, when chocked}
\end{cases}
\tag{2.4}
$$

The mass flow rate not only affects the estimation on the trapped mass, which eventually determines the performance attributes such as work output and efficiency, but also the tumble generation rate, which influences the combustion and heat transfer rate. Therefore, the discharge coefficient is definitely one of the major factors of concern. As mentioned previously, a stronger tumble is attained when the lower-side flow is restricted [45]. In other words, a smaller effective flow area is utilized in high-tumble condition, implying the trade-off relationship between the tumble strength and flow coefficient [20]. Thus, when port geometry is altered to manipulate tumble, its consequential impact on discharge coefficient must be considered concurrently. Since the mass flow rates computed from steady CFD results already reflect all effects of tumble modifications techniques (e.g. port geometry, valve masking, etc.), the appropriate discharge coefficient can be obtained as:

$$
C_D = \frac{\sum \dot{m}_i}{\dot{m}_{isentropic}}
\tag{2.5}
$$

Figure 2.10 depicts the discharge coefficient of the reference engine with Head A. The details of engine specifications can be found in Table 2.1. The discharge coefficient was observed to decrease as the valve lift increases. This agrees with the trade-off relationship between the flow concentration (i.e. tumble strength) and the

charging efficiency mentioned earlier.

Next, the fractional mass flow rate (Π) can be obtained by dividing each divisional mass flow rate with the total mass flow rate:

$$\Pi_i = \frac{\dot{m}_i}{\sum \dot{m}_i} \tag{2.6}$$

Applying this computation, the mass flux field in Figure 2.9 can be reproduced into simple intuitive plot shown in Figure 2.11, in which each dot represents for individual divisions at given valve lift. Up to valve lifts of 2 mm, the fraction of all divisions lie near $1/n_d$ (=0.125), and as the valve lift increases, a greater fraction of intake flow evidently passes through the upper-side of valve curtain (divisions 3 to 6). Division 1 even experiences fraction below 0, which implies the direction of the net flow rate was from the cylinder into the intake port for this division. In addition, the fraction shows a nearly monotonic trend of increase or decrease within each division as valve lift increases. From this observation, it could be justified to interpolate the fraction value for other valve lifts within the overall tested range.

So far, the valve lift is concerned as the only variable affecting the discharge coefficient and flow distribution. But if the discharge coefficient and flow distribution also have a dependency on other parameters, their derivation should be modified correspondingly. Looking at the Eq. (2.4), the valve flow rate is expressed with flow area, temperature, specific heat ratio, and pressure terms, and the valve lift corresponds to the flow area. The specific heat ratio and fluid temperature may vary with injection type (port fuel injection or direct injection) or operating condition (engine speed, boosting, or EGR rate), but their change can be deemed as quasi-

steady within the engine cycles. The pressure condition, however, dramatically changes due to the continuous piston motion. Therefore, the effect of the pressure condition should be investigated.

Various combinations of upstream and downstream pressures are tested with the valve lift fixed of 8 mm, at which the difference in the fractional distribution, if any, would be clearly observed. Figure 2.12 and Figure 2.13 show the results of mass flow rate under pressure difference variation ($\Delta P = P_{in} - P_{out}$) with fixed upstream pressure, and upstream pressure variation with fixed pressure difference, respectively. For all tested conditions, the magnitude of mass flow rate plot changes with respect to the pressure condition but the general shape of the distribution remained throughout. If each result is converted in the form of fractions of total mass flow rate as shown in Figure 2.14, and all curves nearly collapse into a single curve with CoV of 1.751%. This CoV can be reduced down to 0.435% by excluding the pressure difference of 0.1 kPa, which may be too low to yield a stable outcome. The consistent discharge coefficient is also observed with pressure variations with a standard deviation of CoV of 0.8% (Figure 2.15). This infers both the fractional distribution and discharge coefficient can be deemed to be independent on the pressure conditions and the characterization can be implemented for any representative pressure condition.

In engine operation, the upstream and downstream pressures correspond to intake manifold and cylinder pressure, respectively, which are determined by factors such as load, engine speed, and valve timing. Thus, being independent of the pressure condition indicates that the fractional distribution of mass flow can be also concluded as an intrinsic attribute independent of load, engine speed, and valve timings. This supports the postulation that the valve lift is the only variable affecting the fractional

39

distribution.

The discharge coefficient and flow distribution are shown to be independent of pressure conditions. Next, the effect of the head design is to be examined. Table 2.2 summarizes the specifications of cylinder heads with design variations, and Figure 2.16 shows the outline of Heads A, B, and C. Figure 2.17 shows the discharge coefficient versus the valve lift curve for four different head designs, and Figure 2.18 illustrates the fractional distribution of the same head designs at each valve lift.

From the results in Figure 2.17 and Figure 2.18, it can be seen that a very subtle modification to the intake port curvatures can affect quite a difference in the discharge coefficient and the flow distribution behavior at each valve lift. For both top and bottom curvatures, the flow concentration toward upper side occurred when the curvature induces the upward motion of the flow. Thus, a greater concentration was attainable with Head A than with Heads B and C, however, the discharge coefficient had to be sacrificed. Heads B and C happened to yield comparable discharge coefficient but a difference is observed in the flow distribution. Hence, it could be claimed that changing the top curvature was advantageous in tumble enhancement, in this particular case. The sensitivities of design parameters will be further discussed in Chapter 5.

Valve masking is a physical wall that blocks a certain portion of the valve curtain area (see Figure 2.19). Head D is the same with Head C with the only addition of a 2.5mm-tall valve masking, which blocks the lower-side of valve curtain. This masking has a crucial influence at low valve lift condition. For the valve lift smaller than the masking height, the masked head showed almost 60% of reduction in discharge coefficient compared to the unmasked case. In case of flow distribution, the masking disturbed the nearly uniform flow distribution observed with all

40

unmasked head at the low valve lifts. As the valve lift increases above the height of the masking, the impact of masking on discharge coefficient gradually diminishes and eventually become negligible above lift of 6mm. However, its effect on flow distribution still remains at these high lift conditions, weakening the flow concentration toward the uppermost divisions (divisions 4 and 5).

In summary, the intake flow characteristics may be sensitivity to very small design modification, but fortunately, it was demonstrated that the characterization method suggested in this study is able to sufficiently capture the associated phenomena.

With the discharge coefficient and fractional distribution characterized, it is possible to predict both the total and divisional mass flow rates within the engine operation cycle of given engine geometry. The characterization results are integrated into the GT-Power, a commercial 1D tool for engine simulation, and preliminary simulation is performed with a reference engine. Figure 2.20 depicts the results of mass flow rate calculated in GT-Power model, compared with the results of transient CFD performed with identical conditions. Except for some pulsation near the opening of the intake valve, the total mass flow rate ($\dot{m}_{in}$) in Figure 2.20 (left) showed very high agreement with the transient CFD, verifying the reliability of the discharge coefficient obtained by the head characterization process. By combining the fractional distribution in Figure 2.11 with the total mass flow rate, the divisional mass flow rates ($\dot{m}_i$) can be obtained and they are illustrated in Figure 2.20 (right). One deficiency of GT-Power results is that the flow inversion occurs at an identical instant for all divisions, but other than that, it showed an excellent correspondence with the CFD. Plus, it could also be concluded that a few runs of steady CFD (five,

41

in this case) are sufficient to characterize a given cylinder head. The similar level of predictabilities was observed in additional simulations implemented with varying engine speed, load, and port design, which confirms this 0D model can respond to any change in head geometry and predict the detailed valve flow comparable to transient CFD, once characterization results are supplemented.

2.2.3. Flow angles of each division

In addition to the fractional distribution and discharge coefficient, the average velocity is another parameter that can be extracted from steady CFD simulation. Knowing x-, y- and z-components of the average velocity, the representative flow angles θ and ϕ can be drawn for each flow division (the angle configuration shown in Figure 2.21). The effects of changing the pressure conditions and changing valve lift are investigated, and the results of valve lift sweep are shown in Figure 2.22. Thought some deviation exists across the valve lifts, the general trend is interpreted to be consistent compared to the case of concentration. A similar insignificant influence was observed with the pressure variation, hence the flow angle is considered to be independent of the operating conditions.

The angle ϕ is used to decompose the intake velocity into xy- and z-components, each of which constitutes tumble motion and non-tumble mean motion, respectively, while the angle θ is used to calculate tumble moment arms.

Prior to the decomposition, the intake velocity should be found. The velocity across each valve curtain division can simply be estimated for given mass flow rate as:

$$v_i = \frac{\dot{m}_i}{\rho A_i} \qquad (2.7)$$

Since the curtain area is evenly divided, the area of each division (A_i) is simply $\pi D_{IV} L_{IV} / n_d$, where D_{IV}, L_{IV}, and n_d are intake valve diameter, intake valve lift, and the number of divisions, respectively. Compared to the mean velocity from the steady CFD simulation, it was shown that the representative velocity calculated by Eq. (2.7) falls within a reasonable range despite the assumption of constant density (see Figure 2.24). The biggest error is observed in the lower side at high lift condition, and the major reason is the simultaneity of incoming and outgoing flow motion in these divisions. Since the net mass flow rate is used in the calculation, the representative velocities tend to be underestimated for divisions with such bidirectional flow, compared to the CFD results. However, since these velocities are multiplied by the relatively small mass flow rates in further calculations, this error will only have a minor impact on the final results.

One thing to note is that these "isentropic" velocities at the valve opening do not wholly contribute to the tumble generation. As the flow experiences an abrupt expansion of the flow path immediately after passing through the valve opening, thereby the velocity decreases. A coefficient (denoted here as C_{KE}) is typically applied to the kinetic energy flux term to take account of such velocity loss:

$$\dot{E}_{in} = \frac{1}{2} C_{KE} \dot{m} v^2 \qquad (2.8)$$

Since this loss is due to the decrease of velocity, the effective velocity can be interpreted to be $(C_{KE})^{1/2} v$. Therefore, the xy-component of effective velocity, which contributes to tumble generation, can be decomposed written as:

$$v_{\text{tum,i}} = (C_{KE})^{1/2} v_i \cos\phi \qquad (2.9)$$

Similarly, the z-component can be obtained by multiplying $\sin\phi$. Determination of C_{KE} will be discussed in later sections along with other modeling coefficients.

2.2.4. Simulation setup variation

Since the cell size can be a critical factor that decides the accuracy of the CFD results, the same simulation was carried out with cell size variation. By reason of computational cost, the cell size within the interested volume is changed from 2mm to 0.1mm while the general base size was kept constant. Figure 2.25 shows the cross-sectional view of the created mesh for a cell size of 1, 0.5 0.2, and 0.1mm, respectively. The number of faces on the curtain area and the total number of cells in the mesh are listed in Table 2.3.

The simulation was performed with Head A under high lift conditions where a clear distribution deviation between divisions are observable. Figure 2.26 shows the mass flux through the valve curtain when the steady-state is reached. Despite the fact that the number of curtain faces differs by more than 28 times, the general distribution does not seem to have much different. The results processed into the flow distribution are shown in Figure 2.27, which came out to be remarkably coinciding. It could be inferred that the finer spatial resolution provided by smaller cell size is not necessarily beneficial because the results are averaged over the relatively large area of the curtain divisions. Therefore, setting a moderately large cell size would yield satisfactory results with reduced computation time.
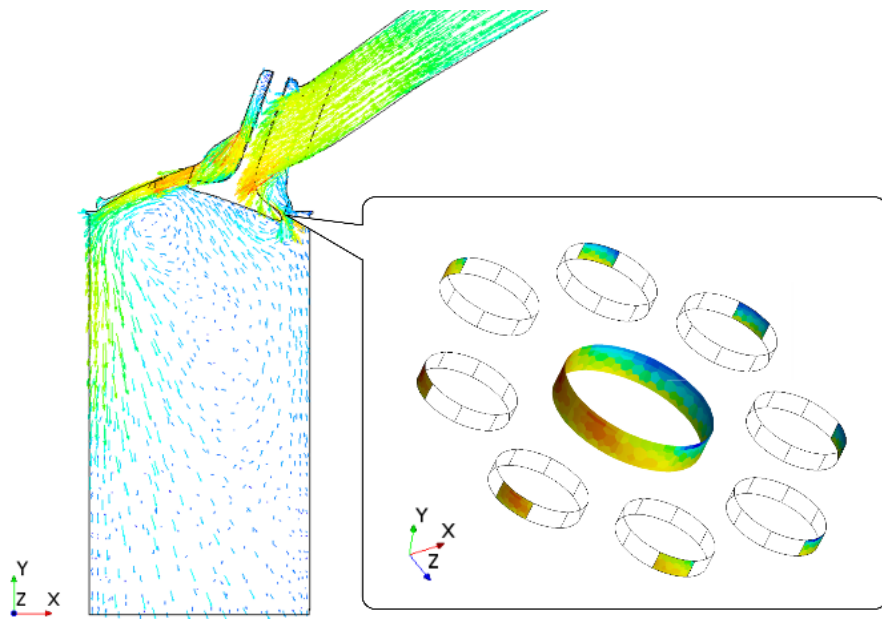
Figure 2.7 Snapshot of Steady CFD Simulation Setup
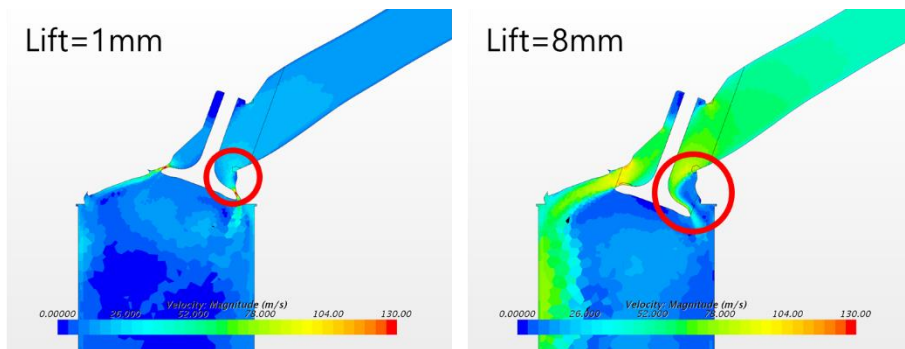
Figure 2.8 Velocity magnitude at valve lift of 1 mm (left) and 8 mm (right)
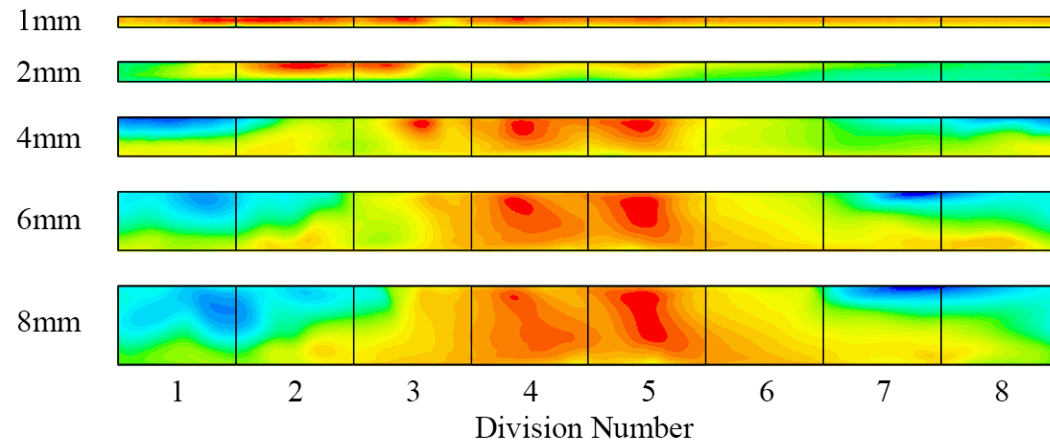
Figure 2.9 Mass flux field across the valve curtain area at different valve lifts
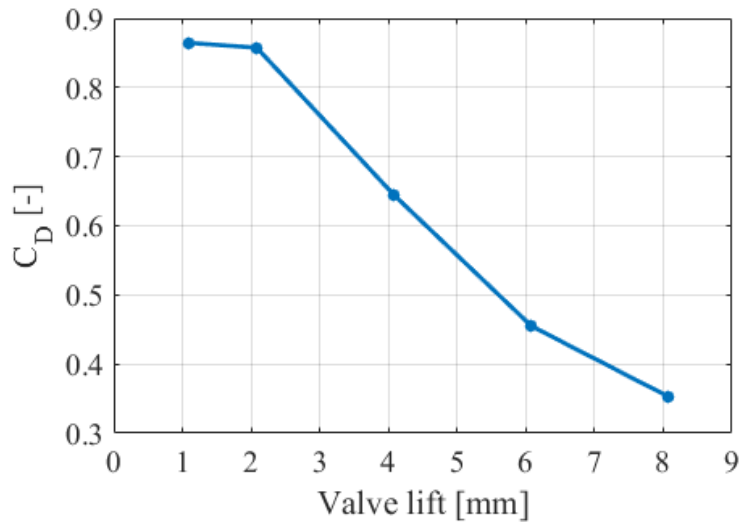
Figure 2.10 Discharge coefficient at each valve lift (Head A)
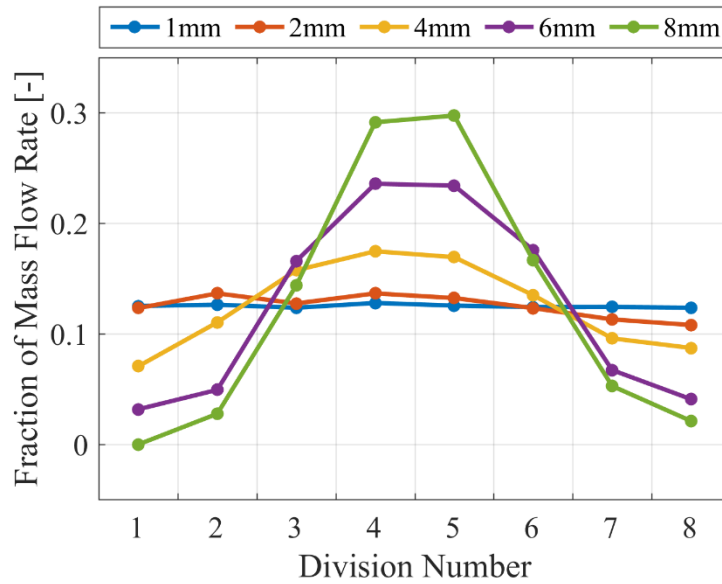
Figure 2.11 Fractional distribution of intake mass flow rate through each curtain area division (Head A)
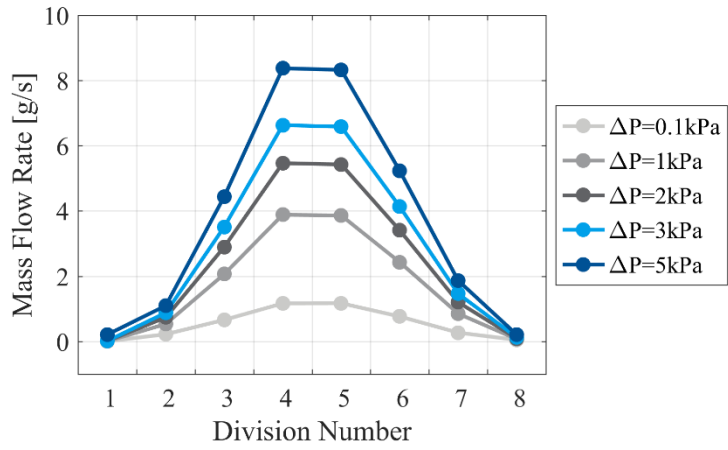
Figure 2.12 Mass flow rates via each division (constant P_{in} at 60 kPa)
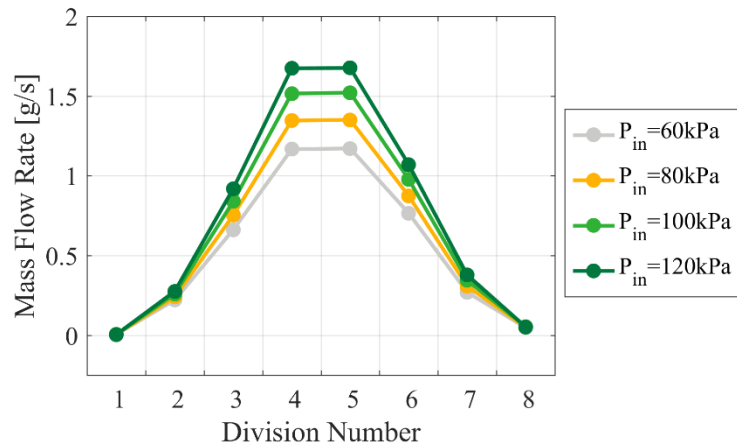
Figure 2.13 Mass flow rates via each division (constant ΔP at 0.1 kPa)
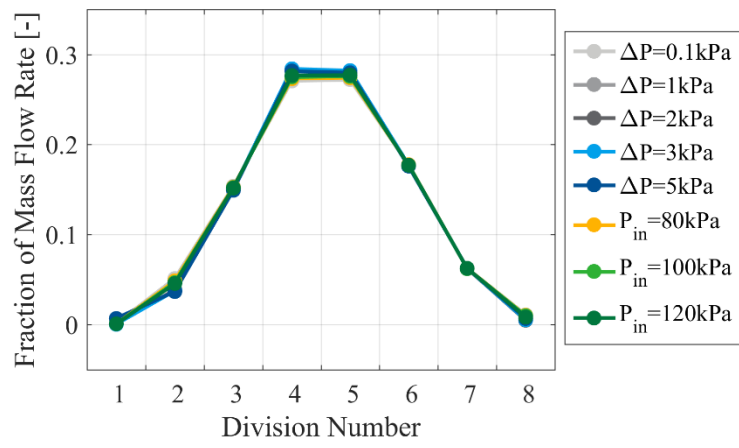
Figure 2.14 Fractions of mass flow rate with pressure condition variation
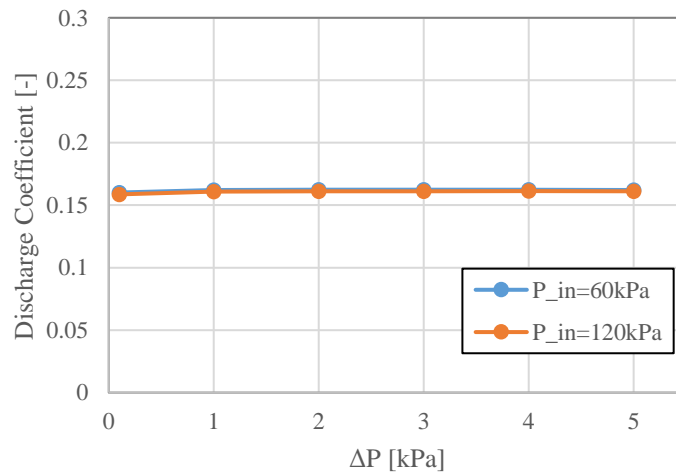
Figure 2.15 Discharge coefficient with pressure condition variation

49
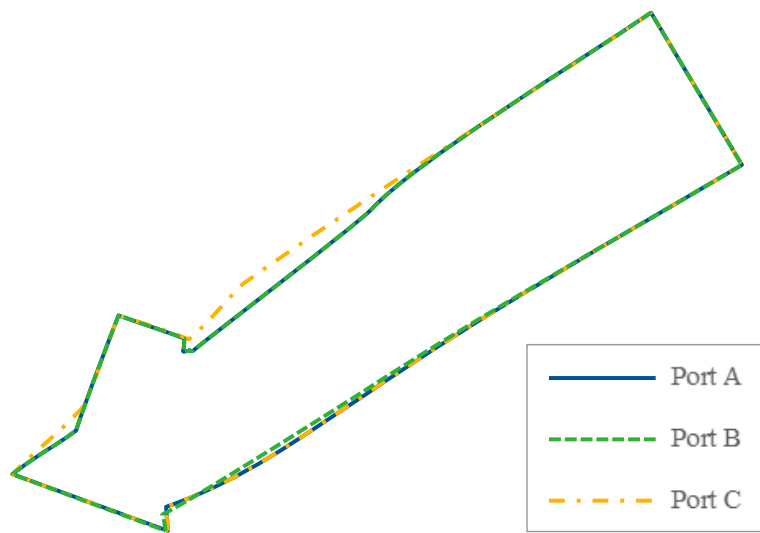
Figure 2.16 Outlines of intake ports of Heads A, B, and C
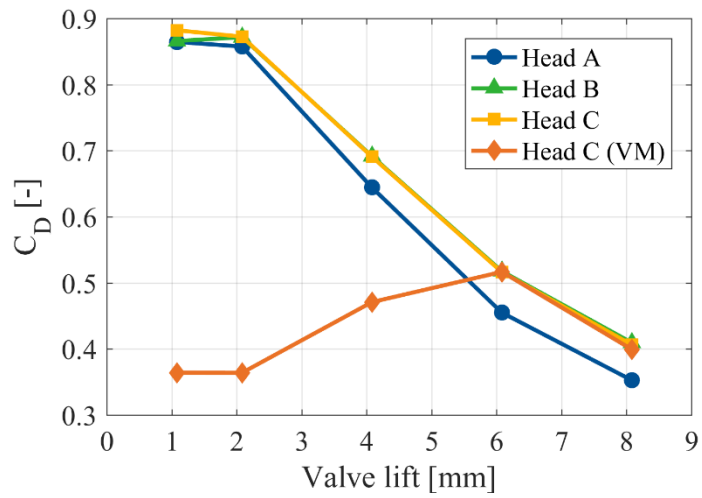
Figure 2.17 Discharge coefficient with head design variation
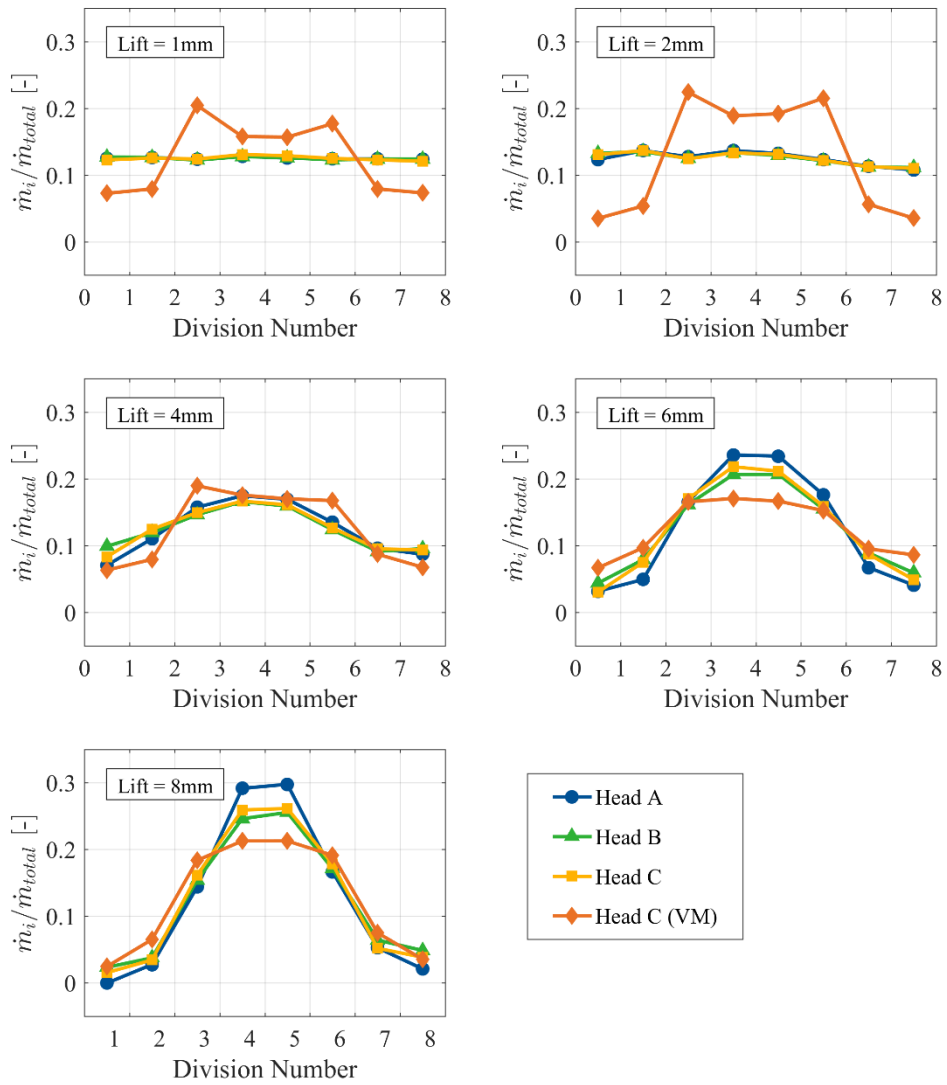
Figure 2.18 Fractions of mass flow rate with head design variation
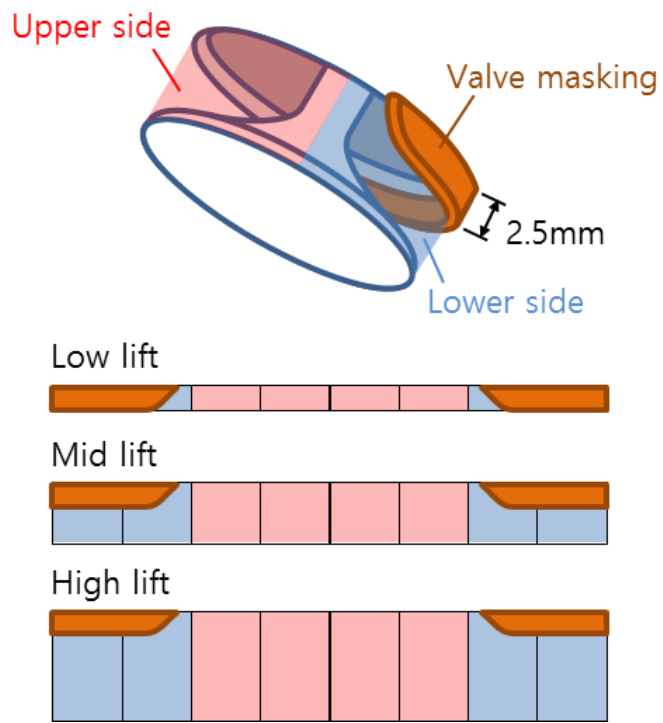
Figure 2.19 Valve masking and its impact on flow area
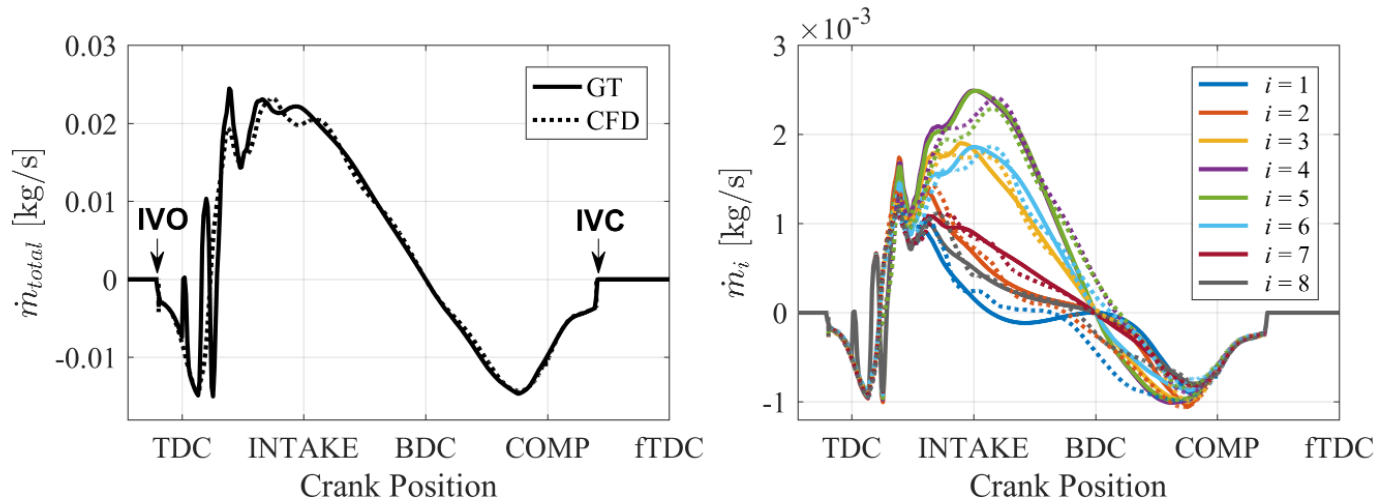
Figure 2.20 Total (left) and divisional (right) mass flow rate over the gas exchange process (solid lines: GT-Power, dotted lines: transient CFD)
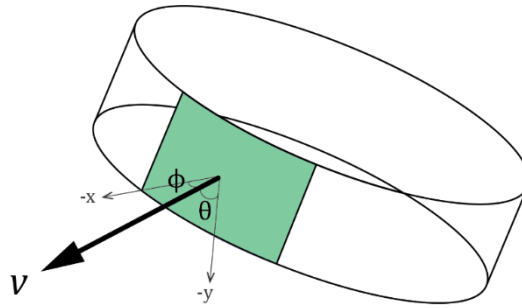
Figure 2.21 The flow angles orientations
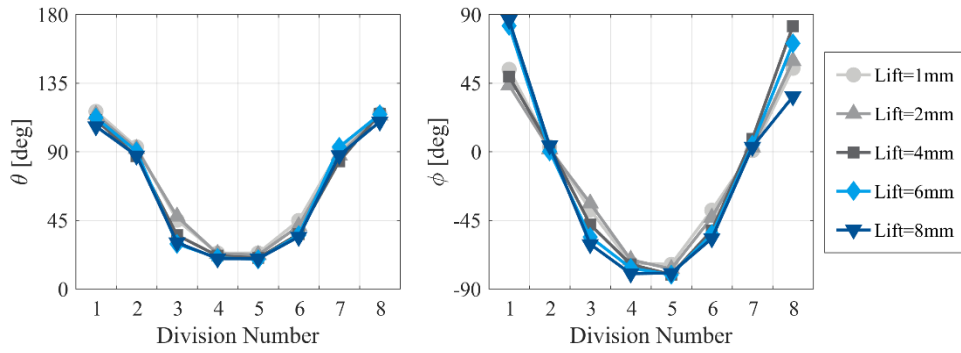
Figure 2.22 Flow angles with valve lift variation
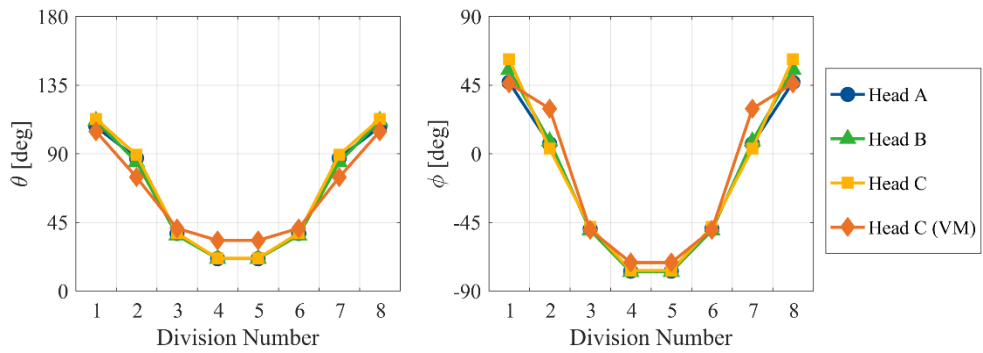
Figure 2.23 Averaged flow angles with head design variation
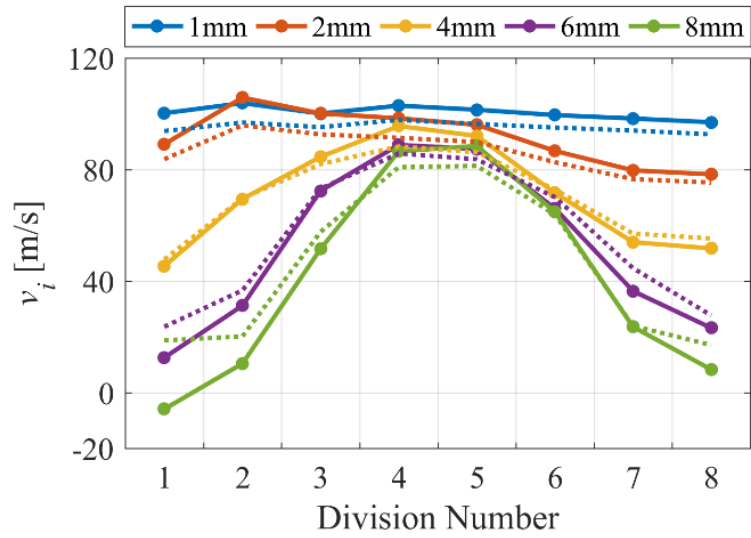
Figure 2.24 Divisional flow velocities passing valve curtain area (solid: 0D, dotted: steady CFD)
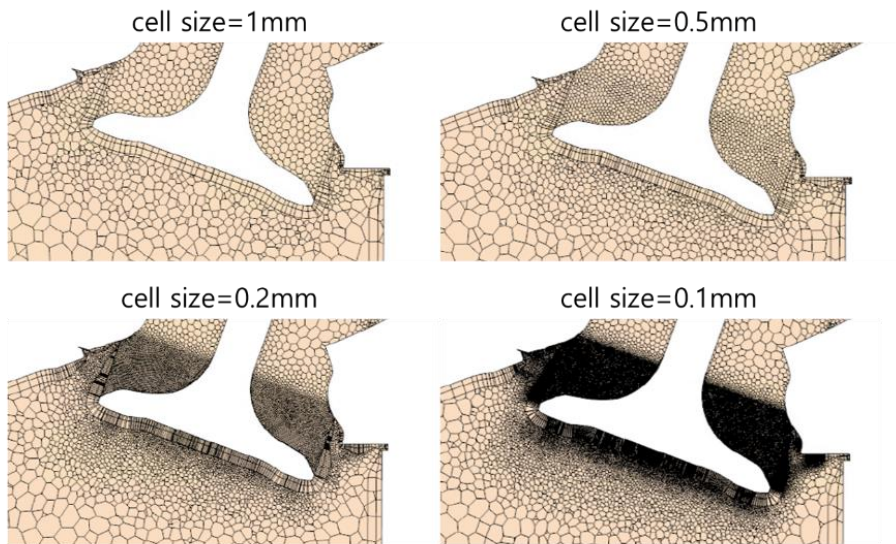
Figure 2.25 Cross-sectional view of created mesh with cell size variation

55
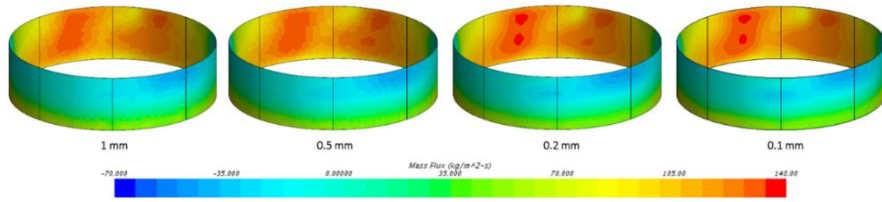
Figure 2.26 Results of mass flux with different cell base sizes
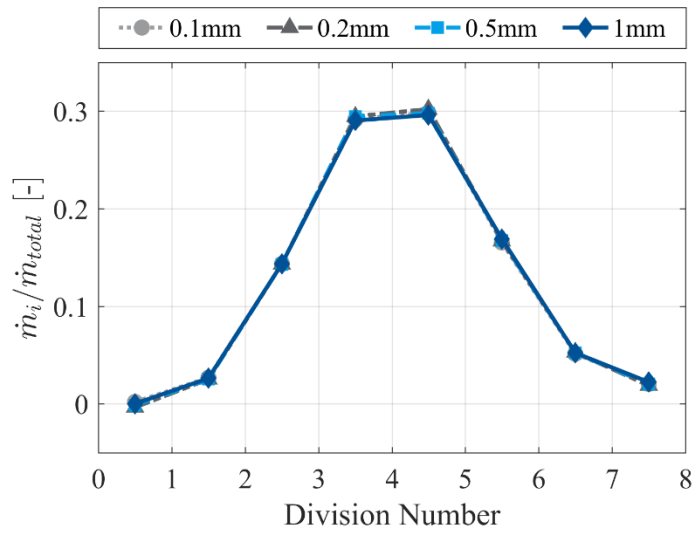
Figure 2.27 Results of fractional mass distribution with different cell base sizes

Table 2.1 Specifications of reference engine

Displacement [cc]	399.5
Bore [mm]	75.6
Stroke [mm]	89
Connecting rod length [mm]	145
Compression ratio	10.5
Intake valve diameter [mm]	30.5
Exhaust valve diameter [mm]	25
Pentroof angle [degree]	20

Table 2.2 Design specifications of tested heads

Head ID	Top curvature [a.u.]*	Bottom curvature [a.u.]
A	-1	2
B	-1	0
C	1	2

* arbitrary unit. a positive value indicates curved outwardly (convex) and a negative value indicates curved inwardly (concave)

Table 2.3 Number of curtain faces and total cells for each cell size

Cell size [mm]*	Number of curtain faces	Number of total cells
2	2,524	287,147
1	2,627	292,298
0.5	3,083	353,399
0.2	17,987	1,122,024
0.1	71,774	5,044,713

* within the control volume only

2.3. Application of pentroof geometry

As mentioned earlier, the model is aimed to be also considerate of the effects of combustion chamber geometry because it can influence both the generation and decay of the tumble motion. In most 0D models, the combustion chamber is assumed to be a pancake shape, which could be misleading in some respects. For example, the postulated locations of representative inlet point for each division can be inadequate when pancake shape is assumed, resulting in the errors on the calculation of tumble generation. In addition, pancake shape with uniform cross-sectional area underestimates the combustion chamber height, especially near TDC, and this significantly affects the flow field and corresponding tumble decay rate (further discussed in chapter 3). Therefore, a correct reflection of the pentroof geometry is strongly encouraged within the calculation process.

As the example shown in Figure 2.28 (upper), the geometry of actual pentroof head is rather complicated for various reasons such as manufacturing process, cooling channels, slots for valves, spark plug, and/or injector, etc. In this model, a smooth, symmetrical pentroof was assumed for the sake of simplicity (illustrated in right schematic in Figure 2.28), and then it could be defined only by the pentroof angle (β), as shown in Figure 2.1.

To assess this simplified pentroof geometry, the moment of inertia, which is the quality that reflects the rotational characteristic in the three-dimensional space, has been chosen for comparison. For typical pancake-shaped combustion chamber, the moment of inertia about the z-axis is written as:

$$I_z = \iiint_{vol} \rho(x^2 + y^2)dV$$

$$= m\left(\frac{B^2}{16} + \frac{H^2}{12}\right)$$

(2.10)

where B and H are cylinder bore and height, respectively. When the simplified pentroof geometry is applied, the volume integral becomes:

$$I_{z,pent} = 8\int_0^R \int_0^{\frac{H}{2}} \int_0^{\sqrt{R^2-x^2}} \rho(x^2 + y^2)dz\, dy\, dx$$

$$- 4\int_0^R \int_{\frac{H}{2}+ax}^{\frac{H}{2}} \int_0^{\sqrt{R^2-x^2}} \rho(x^2 + y^2)dz\, dy\, dx$$

$$= \rho\left[\frac{(64a^3 + 192a)R^5 + (45\pi a^2)HR^4 + 120aH^2R^3 + 30\pi H^3R^2}{360}\right]$$

(2.11)

where a is the pentroof slope defined as $-H_{pent}/R$. Also, note that the volume is no more equal to $\pi R^2 H$. The moment of inertia calculated for each geometric assumption are plotted in Figure 2.29 along with that calculated by the 3D CFD. At the cylinder volume sufficiently large, the assumption of pancake geometry provides a highly accurate moment of inertia, but a distinct increase of error was observed as compression proceeds toward TDC (~55% of error at TDC). Such overestimation in the moment of inertia can be a critical issue because a significant error in the calculation of tumble decay rate would follow. But the pentroofed cylinder yields a result with the error considerably relieved (~70% reduction), from which the assumed simplified pentroof head can be justified.
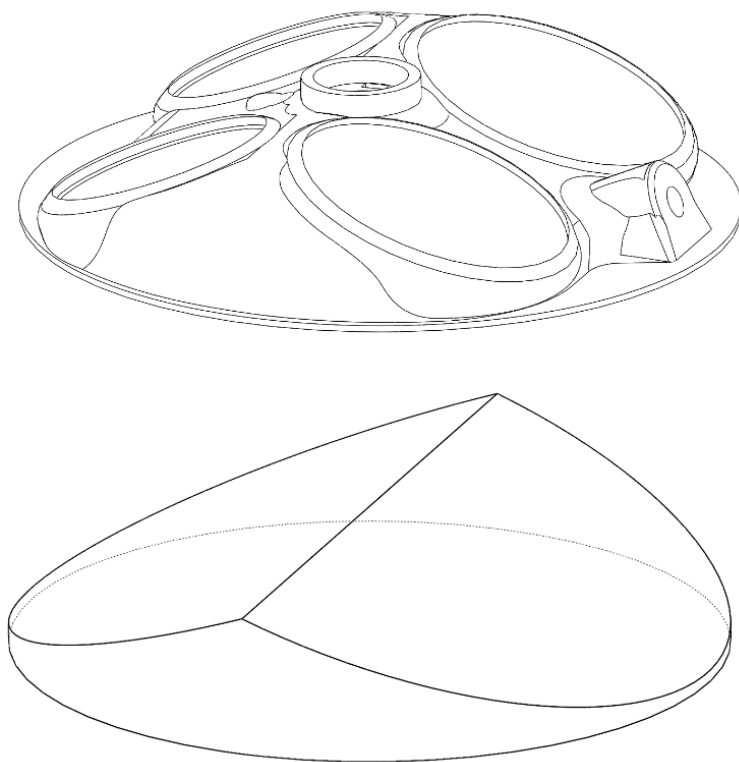
Figure 2.28 Outline of actual (upper) and simplified (lower) pentroof geometry
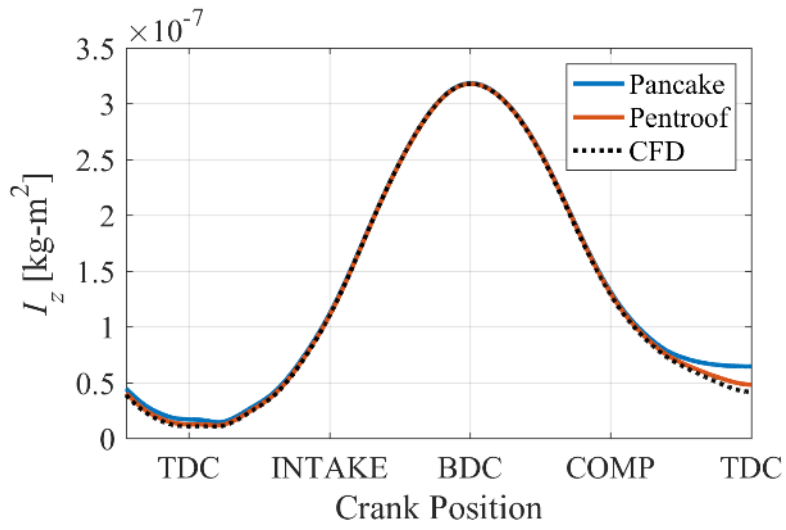
Figure 2.29 Comparison of the moment of inertia calculated by 0D and 3D models

Chapter 3. Development of Tumble Decay Model

With regard to the impact of the tumble motion on engine operation, it is quite common to directly relate the tumble coefficient (or strength) to the flame propagation speed. But precisely speaking, it is not the tumble itself that affects the flame speed, and the tumble should be converted to a useful form, the turbulent kinetic energy, to enhance the flame speed. Thus, how the developed tumble motion is preserved and decays is just as important as inducing a stronger tumble. This chapter includes the conceptualization and development of a tumble decay model that operates in a predictive manner.

3.1. Modeling concept

In previous studies, the tumble decay rate was modeled via several different approaches. The first approach is to consider the large-scale MKE as the source of TKE production, following the energy cascade concept. The TKE production rate by internal shear is defined as:

$$P_\Psi = -\overline{u_i' u_j'} \frac{\partial \overline{U}_i}{\partial x_j}$$
(3.1)

By Boussinesq's eddy viscosity hypothesis, the tensor is simplified and the (3.1) becomes:

$$P_\Psi = \nu_T \left(\frac{\partial \overline{U}_i}{\partial x_j} + \frac{\partial \overline{U}_j}{\partial x_i} \right) \frac{\partial \overline{U}_i}{\partial x_j}$$
(3.2)

In 0D models, the flow structure is not accounted and the velocity gradient is unknown. Therefore, the equation should be further simplified with the

representative velocity (usually the average velocity) and the geometric length scale:

$$P_\Psi = C_\beta \, v_T \left(\frac{\overline{U}}{h}\right)^2$$

(3.3)

This TKE production rate can be assumed as equivalent to the decay rate of tumble motion. Such relation is employed in the models with no clear distinction between tumble and other mean motions and the MKE is deduced to majorly consist of tumble [32, 36]:

$$\left(\frac{dK_{tumble}}{dt}\right)_{decay} = -C_\beta v_T \left(\frac{U}{h}\right)^2$$

(3.4)

Note that C_β is an adjustable coefficient that scales the tumble decay (or TKE production).

Another approach, chosen in the models that separately calculates the tumble with angular momentum, is using a decay function (f_d). Bozza [19]. defined the decay function using two tunable constants: one setting an offset that is active over the entire engine cycle, and the other as a multiplier for the tumble breakdown rate as the compression progresses. In contrast, Grasreiner [39, 40] obtained the decay function by using steady CFD. He gave an initial charge motion in a specific static geometry (with no piston movement) and measured the decaying of the given motion over time. In such a way, a decaying curve was completed as a function of dimensionless height (H/B). In the studies using the decay function, it is commonly correlated that the decay rate is proportional to the instantaneous angular momentum and turbulent intensity ($\sim\sqrt{k}$):

$$\left(\frac{dL}{dt}\right)_{decay} = -\frac{f_d L \sqrt{k}}{r_t} \qquad (3.5)$$

But either way, when any modification in the engine geometry is made, a new decay function must be obtained for different engines by calibrating with the corresponding experimental data or by performing the CFD. Because of this engine-specific nature, the approach of decay function is considered unacceptable for the purpose of the present study.

The last approach is to assume the velocity field inside the combustion chamber and calculate the resistive forces acting on it. Typically, 0D models cannot take into account the flow structure, but Benjamin [35] suggested the assumption of the velocity field inside the combustion chamber. This so-called "barrel-swirl" model calculates the torque due to the wall friction and fluid internal shear on the velocity field prescribed as:

$$\begin{cases} U_x = U\left(1 - \frac{z^2}{R^2}\right)\frac{y}{h} \\ U_y = -U\left(1 - \frac{z^2}{R^2}\right)\frac{x}{w} \\ U_z = 0 \end{cases} \qquad (3.6)$$

where h and w are the halves of the cylinder height and width, respectively (see Figure 3.1). The same 2D linear velocity field is also adopted by Achuth [18] and Ramajo [37]. To fully define this velocity field, the tangential velocity U must be found, and this can be obtained for a given angular momentum (or tumble strength) by using the angular momentum equation for this field:

$$L = \iiint\limits_{vol} \rho(-U_x y + U_y x)dV$$

By applying the above velocity profile, the tangential velocity U can be expressed in terms of angular momentum L. Once the tangential velocity is found for the given angular momentum, the velocity field is fully defined, and the opposing torque due to the wall friction and internal shear can be calculated.

This method of defining the velocity profile and predicting the shear rate based on the corresponding flow field is considered to be suitable for use in the predictive model since it is obtained by the physical relations in a given cylinder geometry with no any additional calibration other than velocity profile assumption. However, several controversies may be raised with this method.

The first issue is the energy balance. In the barrel-swirl model, both the tumble decay rate and TKE production rate are calculated using the prescribed velocity field, however, there is no rational connection between the two. This appears to disagree with the energy cascade concept.

Secondly, the defined velocity profile is somewhat impractical. Although the velocity profile of the original barrel-swirl model can properly represent the basic structure of the tumble vortex, which has greater velocity as it gets further away from the vortex center, this profile postulates that boundary velocities at the top, bottom, and wall side are all equal, which seems impractical for certain piston positions.

Lastly, it assumes a simplified chamber geometry. In all studies employed the barrel-swirl model, the tumble decay due to internal shear was calculated with

formulas derived with the assumption of disk-shaped geometry. This can possibly be a source of considerable error, and more realistic pentroof geometry may be considered.

Therefore, in this study, it is proposed a decay model that considers both the tumble flow structure and the energy balance. Also, the model is improved to reflect more realistic velocity profile and chamber geometry.
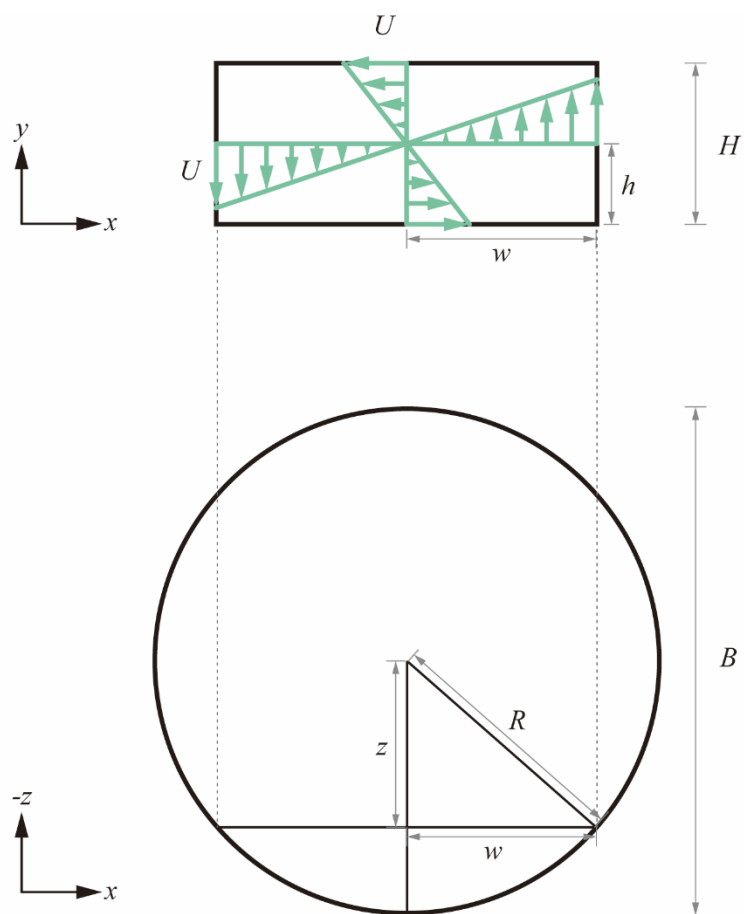
Figure 3.1 Velocity profile of the original barrel-swirl model

3.2. Application of energy cascade concept

In the barrel-swirl model, the prescribed velocity profile is utilized to compute the characteristic velocity at given angular momentum, and the corresponding momentum loss and TKE production rate. First, the velocity field should be fully defined by finding U, which can be implemented by solving (3.7). With the assumption of disk-shaped chamber geometry, this writes as:

$$L = -8 \int_0^R \int_0^{\frac{H}{2}} \int_0^{\sqrt{R^2-x^2}} \rho \left(U \left(1 - \frac{z^2}{R^2} \right) \frac{y^2}{h} + U \left(1 - \frac{z^2}{R^2} \right) \frac{x^2}{w} \right) dz \, dy \, dx \tag{3.8}$$

and by applying the velocity field,

$$L = \frac{\rho U \pi R^2 H}{8} \left(H + \frac{256}{45\pi} R \right) \cong \frac{mU}{8} (H + 1.81R) \tag{3.9}$$

By solving Eq. (3.9) for U, the characteristic velocity can be expressed as a function of mass, angular momentum and geometric dimensions only:

$$U = \frac{8L}{m(H + 1.81R)} \tag{3.10}$$

The original barrel-swirl model estimates the tumble decay rate by calculating the fluid shearing stress (T_s) and the wall shear stress (T_w). The fluid shearing stress is expressed as:

$$T_s = \int_{surf} \left(\tau_{xy} dz + \tau_{yz} dx \right) WH \tag{3.11}$$

where

$$\begin{cases} \tau_{xy} = \rho \nu_T \left(\dfrac{\partial U_y}{\partial x} + \dfrac{\partial u_x}{\partial y} \right) \\[3mm] \tau_{xy} = \rho \nu_T \left(\dfrac{\partial u_x}{\partial y} + \dfrac{\partial u_y}{\partial z} \right) \end{cases} \tag{3.12}$$

As can be seen in the equations, this method only accounts for the shear stress acting on the surface of the vortex. By applying the velocity profile described above, the fluid shearing stress is computed as

$$T_s = \frac{3U m \nu_T}{2} \left(\frac{1}{H} + \frac{16}{9\pi B} \right) \tag{3.13}$$

On the other hand, the TKE production within the cylinder can be expressed as:

$$m\dot{k}_\Psi = \iiint\limits_{vol} \rho P_\Psi \, dV \tag{3.14}$$

Substituting Eq. (3.2) and the velocity profile, it becomes:

$$m\dot{k}_\Psi = \rho \nu_t \iiint\limits_{vol} \left[\left(\frac{\partial U_x}{\partial y} \right)^2 + \left(\frac{\partial U_y}{\partial x} \right)^2 + \left(\frac{\partial U_x}{\partial z} \right)^2 + \left(\frac{\partial U_y}{\partial z} \right)^2 \right.$$
$$\left. + 2 \left(\frac{\partial U_x}{\partial y} \right) \left(\frac{\partial U_y}{\partial x} \right) \right] dV$$
$$= 8\rho \nu_t \int_0^R \int_0^{\frac{H}{2}} \int_0^{\sqrt{R^2 - x^2}} \left[\left(\frac{U}{h} \left(1 - \frac{z^2}{R^2} \right) \right)^2 + \left(-U \left(1 - \frac{z^2}{R^2} \right) \frac{x^2}{w} \right)^2 + \left(-\frac{2U}{hR^2} yz \right)^2 \right.$$
$$\left. + 2 \left(\frac{U}{h} \left(1 - \frac{z^2}{R^2} \right) \right) \left(U \left(1 - \frac{z^2}{R^2} \right) \frac{x^2}{w} \right) \right] dz \, dy \, dx$$
$$= \frac{5}{2} m \nu_t U^2 \left(\frac{1}{H^2} + \frac{28}{15B^2} - \frac{512}{75\pi BH} \right) \tag{3.15}$$

It can be easily noted that the opposing torque by shear stress in Eq. (3.13) differs with the TKE production rate. But according to the energy cascade concept, the large-scale mean motion, namely tumble, is converted into the TKE. Therefore,

the decline rate of rotational energy can be directly linked with the TKE production by internal shear:

$$\frac{dE_{rot}}{dt} = -m\dot{k}_\Psi$$

(3.16)

The rotational kinetic energy of tumble can be expressed simply as

$$E_{rot} = \frac{1}{2}I\omega^2 = \frac{L^2}{2I}$$

(3.17)

and taking time derivative, the rate of change in rotational energy is expressed as

$$\frac{dE_{rot}}{dt} = \frac{L}{I}\left(\frac{dL}{dt}\right) - \frac{L^2}{2I^2}\left(\frac{dI}{dt}\right)$$

(3.18)

Assuming no moment of inertia change by tumble decay, the second term on the right-hand side becomes zero, and the formula for tumble decay rate can be obtained by combining Eqs. (3.14), (3.16), and (3.18),

$$\left(\frac{dL}{dt}\right)_\Psi = -\frac{I}{L}\iiint_{vol}\rho P_\Psi dV$$

(3.19)

This method is similar to that used by Grasreiner [39, 40] in the sense that they both relate TKE production and tumble decay. The difference is either TKE production is determined from the computed tumble decay rate, or the tumble decay rate is determined from the calculated TKE production. In the method of Grasreiner, however, the tumble decay rate is computed from an engine-specific CFD simulation, inferring low predictive capability. On the other hand, the method suggested in present study utilizes the general TKE production equation used in Reynolds-Averaged Navier-Stokes (RANS) simulation and does not require any additional process other than the assumption of the velocity field structure. A similar method

has also been employed in Yang's quasi-dimensional diesel engine model for calculation of swirl decay rate [46].

3.3. Modification of velocity profile

As mentioned in section 3.1, the original velocity profile seems impractical as it assumes equal velocity at top/bottom and wall side regardless of the piston position The suspicion on the original velocity profile is also be supported by the CFD results. Figure 3.2 shows a snapshot of velocity field calculated by 3D CFD during the compression process, in which a clear difference between in velocity magnitudes are observed. This implies that if the original velocity profile is used, the tangential velocity is underestimated for a given angular momentum, and therefore the decay rate is likely to be underestimated accordingly. In consistence with this hypothesis, considerable underestimation of tumble decay was observed in the study of Ramajo, which compared cyclic simulation results of the 0D model to the CFD results [37]. This tumble decay rate and the resultant turbulence can exert a critical influence on the calculations on engine performance, thus it seems essential to improve the flow field for better representation of the real situation.

Seeing from perspective of the continuity about rotation, the velocity of the shorter side should be greater than the longer side to allow the same mass flow rate. Hence, the velocity profile is modified so that the boundary velocities at top/bottom sides and wall side are related using the ratio between cylinder height and width [47]. The prescript of modified velocity is as below, and this is also illustrated in Figure 3.3:

$$\begin{cases} U_x = U\left(1 - \dfrac{z^2}{R^2}\right)\dfrac{y}{h} \\[3mm] U_y = -\dfrac{h}{w}U\left(1 - \dfrac{z^2}{R^2}\right)\dfrac{x}{w} = -\dfrac{Uh}{R^2}x \\[3mm] U_z = 0 \end{cases} \tag{3.20}$$

If the new velocity profile is applied to the angular momentum equation,

$$L = -8\int_0^R \int_0^{\frac{H}{2}} \int_0^{\sqrt{R^2-x^2}} \rho\left(U\left(1 - \frac{z^2}{R^2}\right)\frac{y^2}{h} + \frac{Uh}{R^2}x^2\right)dz\,dy\,dx$$

$$= \frac{\rho U\pi R^2 H^2}{4} \cong \frac{1}{4}mUH \tag{3.21}$$

thus,

$$U = \frac{4L}{mH} \tag{3.22}$$

Similarly, the TKE production becomes

$$m\dot{k}_\psi = \iiint\limits_{vol} \rho P_\psi\, dV$$

$$= \rho\nu_t \iiint\limits_{vol} \left[\left(\frac{\partial U_x}{\partial y}\right)^2 + \left(\frac{\partial U_y}{\partial x}\right)^2 + \left(\frac{\partial U_x}{\partial z}\right)^2 + \left(\frac{\partial U_y}{\partial z}\right)^2 + 2\left(\frac{\partial U_x}{\partial y}\right)\left(\frac{\partial U_y}{\partial x}\right)\right]dV$$

$$= 8\rho\nu_t \int_0^R \int_0^{\frac{H}{2}} \int_0^{\sqrt{R^2-x^2}} \left[\left(\frac{U}{h}\left(1 - \frac{z^2}{R^2}\right)\right)^2 + \left(-\frac{Uh}{R^2}\right)^2 + \left(-\frac{2U}{hR^2}yz\right)^2\right.$$

$$\left. + 2\left(\frac{U}{h}\left(1 - \frac{z^2}{R^2}\right)\right)\left(-\frac{Uh}{R^2}\right)\right]dz\,dy\,dx$$

$$= \frac{5}{2}m\nu_t U^2\left(\frac{1}{H^2} - \frac{28}{15B^2} + \frac{8H^2}{5B^4}\right) \tag{3.23}$$

which can be substituted into Eq. (3.19) to yield the new tumble decay rate.
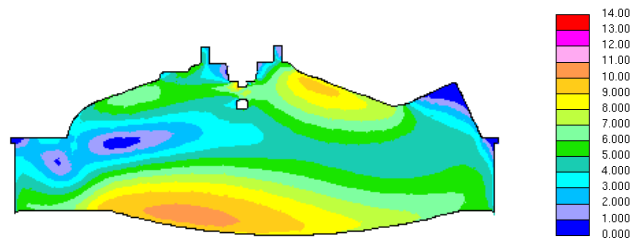
Figure 3.2 Velocity field estimated by CFD near the end of the compression
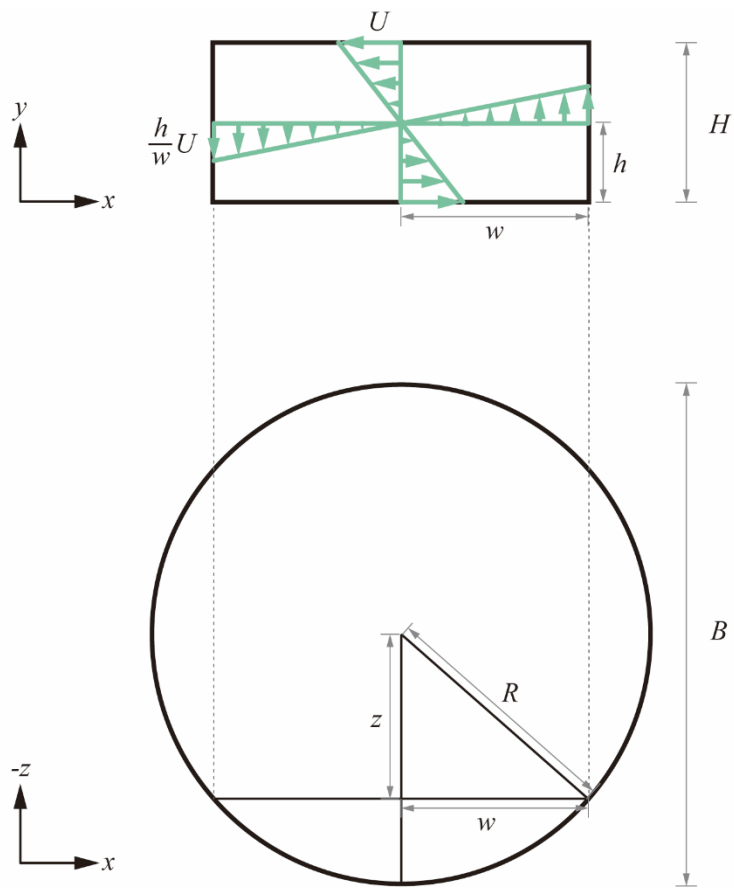
Figure 3.3 Modified velocity profile

3.4. Application of pentroof geometry

When the disk-shaped chamber is assumed, as in the most 0D models, the cylinder height is smaller than the actual case with the pentroof chamber, and the calculation error becomes exaggerated, especially near the TDC. This is because the lower cylinder height not only causes an overestimation of the tangential velocity U but also increases the velocity gradient, leading the decay rate to be excessively high. The experimental study by Hadded [48] demonstrated the fact that the tumble survives longer in the pentroof chamber.

So the simplified pentroof, described in chapter 2, was considered in the calculation of the characteristic velocity and TKE production rate (Figure 3.4). As mentioned in section 2.4, the tumble center is assumed to be the mid-point of the maximum height along the cylinder axis, and the upper boundary in y-direction for the volume integral needs to be modified as follows:

$$L = 8 \int_0^R \int_0^{\frac{H}{2}} \int_0^{\sqrt{R^2-x^2}} \rho\left(-U_x y + U_y x\right) dz \, dy \, dx$$

$$- 4 \int_0^R \int_{\frac{H}{2}+ax}^{\frac{H}{2}} \int_0^{\sqrt{R^2-x^2}} \rho\left(-U_x y + U_y x\right) dz \, dy \, dx$$

$$= 8 \int_0^R \int_0^{\frac{H}{2}} \int_0^{\sqrt{R^2-x^2}} \rho U \left(\frac{(R^2-z^2)y^2}{hR^2} + \frac{hx^2}{R^2}\right) dz \, dy \, dx$$

$$- 4 \int_0^R \int_{\frac{H}{2}+ax}^{\frac{H}{2}} \int_0^{\sqrt{R^2-x^2}} \rho U \left(\frac{(R^2-z^2)y^2}{hR^2} + \frac{hx^2}{R^2}\right) dz \, dy \, dx$$

$$= \frac{1}{4}\rho U \pi R^2 H^2 + \frac{\rho U R^3(256a^3R^2 + 175\pi a^2 HR + 672aH^2)}{840H} \qquad (3.24)$$

and

$$U = \frac{840H}{\rho R^2 (256a^3 R^3 + 175\pi a^2 HR^2 + 672aH^2 R + 210\pi H^3)} L \qquad (3.25)$$

And similarly, overall TKE production within the cylinder is:

$$m\dot{k}_\Psi = \rho v_t \iiint\limits_{vol} \left[\left(\frac{\partial U_x}{\partial y}\right)^2 + \left(\frac{\partial U_y}{\partial x}\right)^2 + \left(\frac{\partial U_x}{\partial z}\right)^2 + \left(\frac{\partial U_y}{\partial z}\right)^2 \right.$$

$$\left. + 2\left(\frac{\partial U_x}{\partial y}\right)\left(\frac{\partial U_y}{\partial x}\right) \right] dV$$

$$= \rho v_t U^2 \left[\pi R^2 H \left(\frac{5}{2H^2} - \frac{7}{6R^2} + \frac{H^2}{4R^4} \right) \right.$$

$$\left. + \left(\frac{(128a^2 + 1152)aR^3}{315H^2} + \frac{\pi a^2 R^2}{3H} - \frac{16aR}{15} + \frac{H^2}{3R} \right) \right] \qquad (3.26)$$

Eqs. (3.24) to (3.26) are the new expression for tumble angular momentum, characteristic velocity, and TKE production. Note that this equation includes the pentroof slope a, which reflects the cut-out portion of the cylindrical volume.
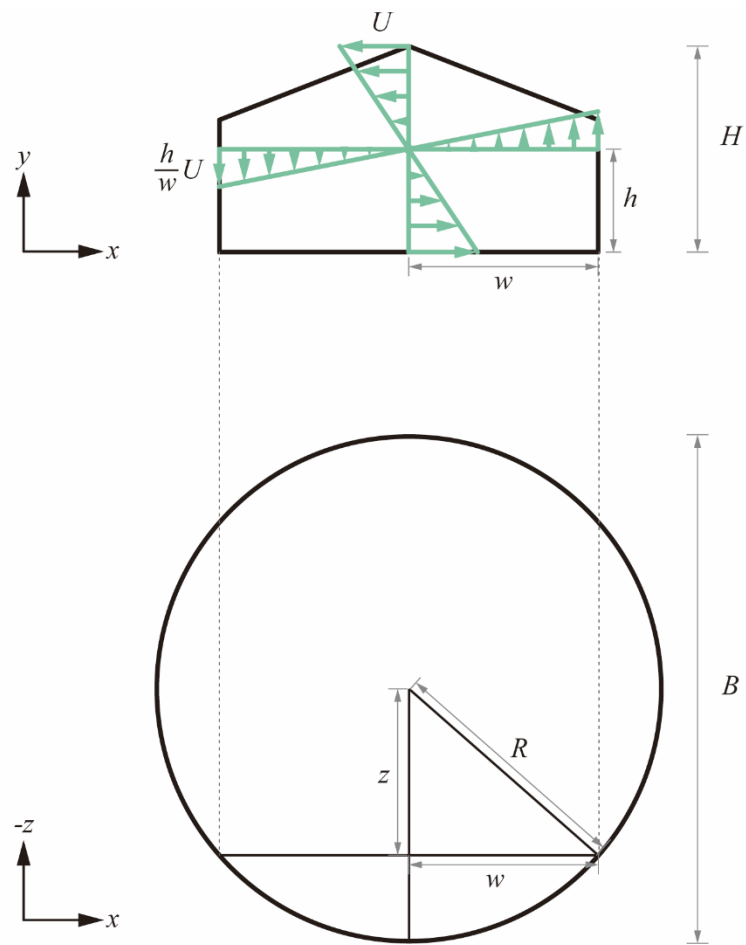
Figure 3.4 Modified velocity profile in the pentroof chamber

3.5. Comparison between decay models

3.5.1. Qualitative comparison of decay models at fixed tumble

Figure 3.5 shows how the characteristic velocity varies with modifications of the velocity profile and chamber geometry. The cylinder mass and tumble angular momentum is computed from CFD results of a sample motored case. The cylinder volume was kept constant, which resulted in a slightly larger chamber height for the pentroof chamber.

Figure 3.5 provides a qualitative comparison that shows how each decay model differs under constant mass and tumble conditions. The cylinder mass and tumble angular momentum of a sample motored CFD simulation is used for this comparison, and the top plot shows the temporal evolution of the two qualities. The middle plot shows the cylinder height when assuming the disk shape and the simplified pentroof. The pentroof angle is set at 20 degrees, and slightly larger cylinder height is indeed computed for the pentroof chamber with equivalent cylinder volume. The bottom plot shows the calculated characteristic velocity U for three different models: the original velocity profile in the disk chamber, and the modified velocity profile in the disk chamber and pentroof chamber, respectively.

When H is greater than $1.81R$ (BDC $\pm$ 80 CAD), U is calculated slightly higher for the original profile. In the case of using a modified velocity profile, the y-direction velocity becomes relatively small compared to the original profile as cylinder height decreases along with compression. subsequently, the x-direction

79

velocity increases in order to match the same angular momentum. Near TDC, where the major tumble breakdown occurs, the x-direction tangential velocity U vary by up to four times, and when the pentroof chamber is additionally considered, the new geometric boundary relieves the difference and causes a slight drop in the characteristic velocity. Figure 3.6 provides the 2D view of the velocity field in each case at a particular incident close to TDC (boxed in Figure 3.5).

As can be seen from Eq. (3.26), TKE production is proportional to the square of tangential velocity U, inferring much greater tumble decay rate would be calculated for the modified velocity profile. And the pentroof geometry may cause a notable attenuation of the tumble decay rate since it causes an increase in cylinder height as well as a decrease in tangential velocity. Here, only qualitative trends of characteristic velocity were assessed with given angular momentum trace, but when the tumble decay rate in each decay model comes into play, the angular momentum and turbulence level would also be affected. Further analysis with such overall impact will be discussed in the next section.

3.5.2. Cyclic simulation with different decay models

The engine cyclic simulation was performed by applying each of the decay models, and the results were analyzed. First, from the results of the tumble generation rate of Figure 3.7, a greater generation rate is observed when the pentroof chamber is applied. This is due to the combined effect of the longer cylinder height and the individual flow angles/inlet points. This is a demonstration of the same mass flow rate and distribution causing a different tumble strength, which was described earlier in chapter 2. Because of this high tumble generation, the modified profile with

pentroof chamber revealed a higher characteristic velocity than in the disk chamber, which slightly differs from that shown in Figure 3.8.

Figure 3.9 shows the tumble decay rate calculated based on the velocity field and chamber geometry. Comparing the two velocity profiles in the disk chamber, the modified profile produces a strong decay rate because it has a higher characteristic velocity than the original profile. This results in a greater decrease of the angular momentum near BDC and TDC, despite the same tumble generation (Figure 3.10). The greater decay rate indicates more TKE production, and thus the turbulent intensity rise in the second peak (~30 degrees bTDC) is greater (Figure 3.11).

When the chamber geometry is changed from disk to pentroof, the tumble decay rate is observed to be greater around BDC and smaller near TDC (Figure 3.9). The major reason for higher decay at BDC is the greater angular momentum being built in case of pentroof chamber. However, a weaker magnitude in the decay rate is observed for the pentroof chamber near TDC despite the higher tumble angular momentum. Instead, the tumble decay occurred for a longer period. Such a trend is interpreted to be because of the increased cylinder height. Compared to the disk chamber, the chamber volume undergoes a moderate distortion with the pentroof chamber, and the relieved decay rate caused the TKE level to be sustained for a longer period as shown in Figure 3.11. In summary, the pentroof geometry caused increased and prolonged the tumble breakdown period, which resulted in increased TKE level near TDC.

In general, the circular motion is most stable when it draws a perfect circle, and in the engine, this infers the point when the cylinder height equals the bore. The

target engine has a stroke-to-bore ratio of about 1.18, meaning the chamber height is longer than the bore near BDC, even when the disk chamber is assumed. Therefore, the increased height with pentroof chamber results in a severer tumble decay rate near BDC.
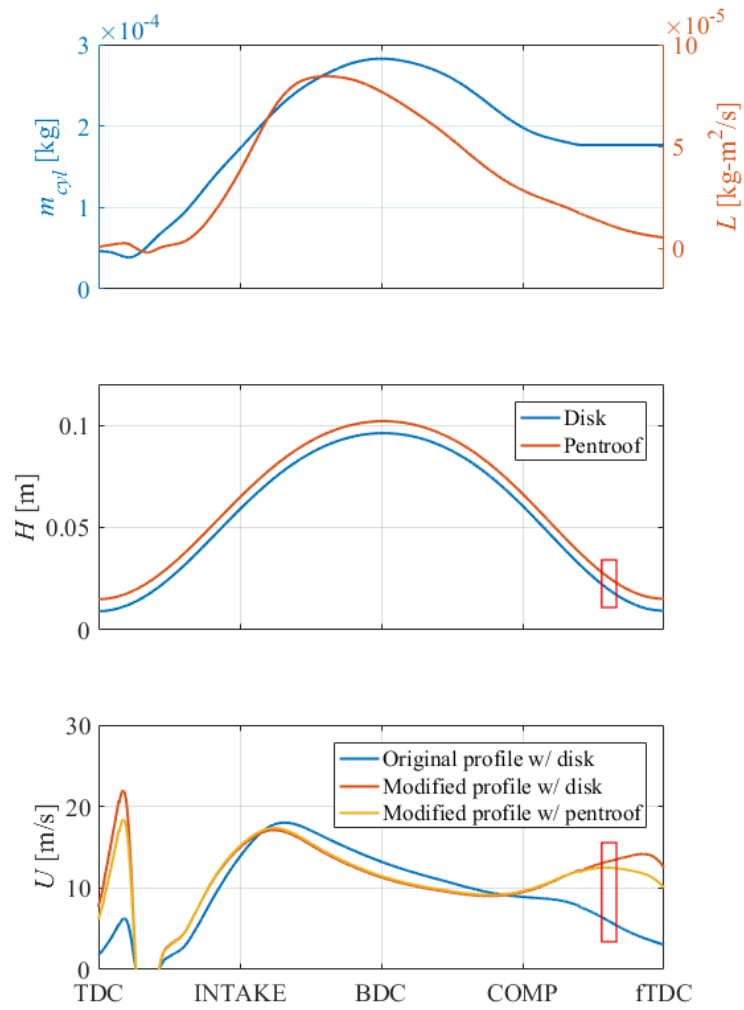
Figure 3.5 Comparison of decay model with fixed angular momentum
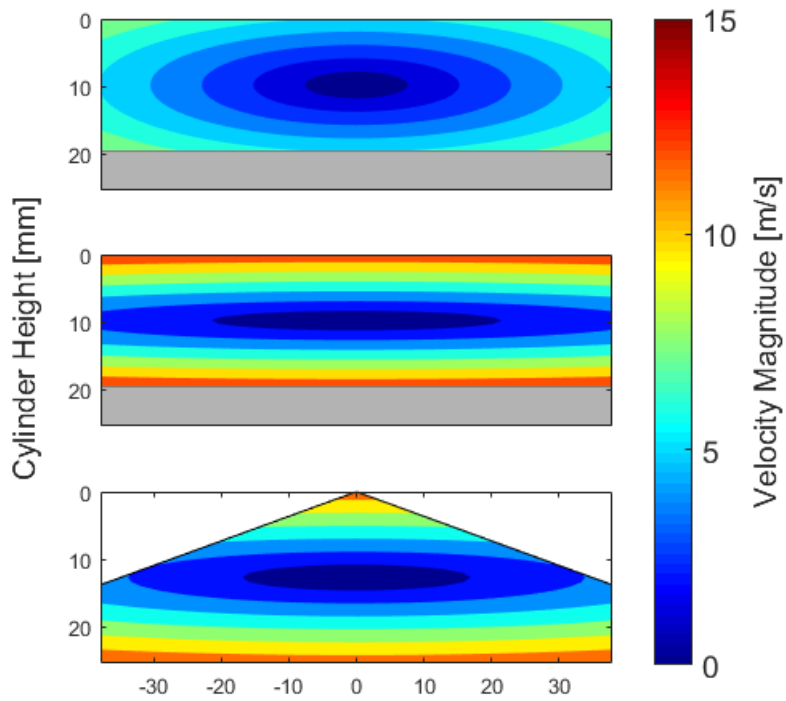
Figure 3.6 Velocity field for different decay models: Original profile with disk chamber (top), modified profile with disk chamber (middle), and modifield profile with pentroof chamber (bottom)

84
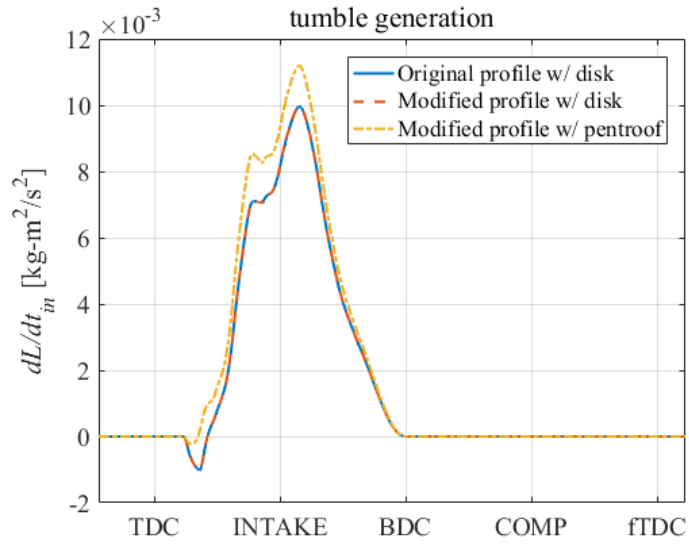
Figure 3.7 Results of tumble generation rate from cyclic simulation
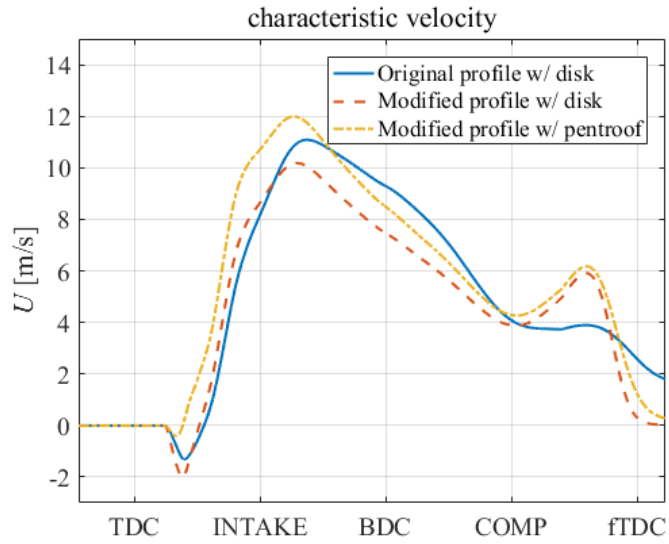
Figure 3.8 Results of characteristic velocity from cyclic simulation
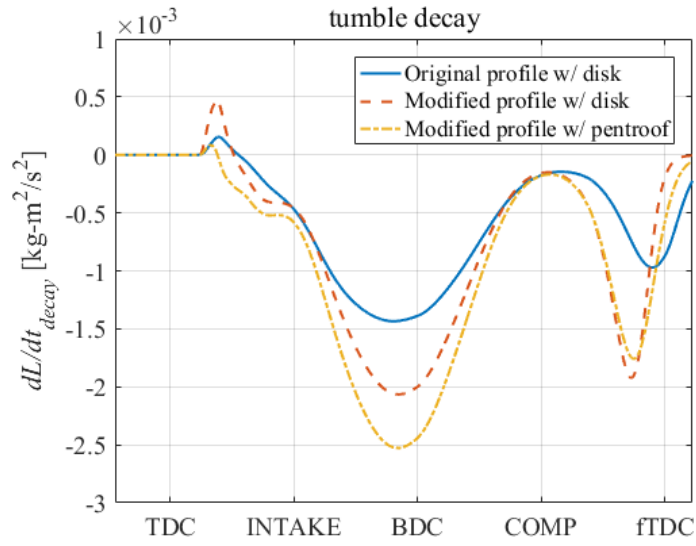
Figure 3.9 Results of tumble decay rate from cyclic simulation
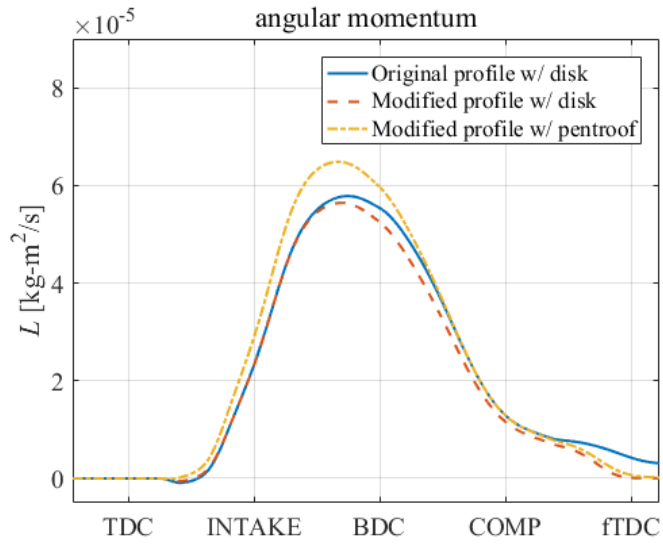
Figure 3.10 Results of tumble angular momentum from cyclic simulation

86
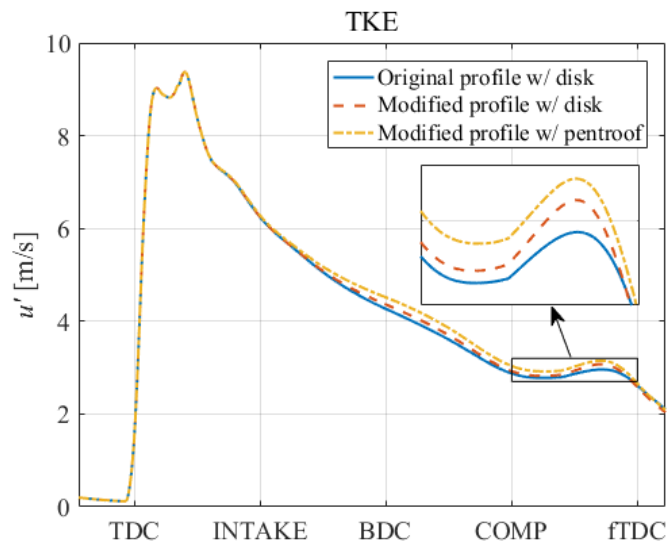
Figure 3.11 Results of turbulent intensity from cyclic simulation

Chapter 4. Model Integration and Validation

4.1. Integration into the turbulence model

The developed tumble model is integrated into the k-ε model to complete the new turbulence model, and Figure 4.1 describes the overall concept of energy flow. In this study, large-scale motions, generally classified as mean kinetic energy (MKE) in 0D turbulence model, are divided into a tumble and non-tumble components, so it can account for the unique generation and decay of tumble motion as well as the non-tumble mean kinetic energy in the energy balance. A certain amount of non-tumble component is modeled to participate in instantaneous TKE production, and the rest to create minor mean motions such as cross-tumble. Loss of each quality occurs along with the outgoing flow, and the TKE is dissipated into internal energy at the rate of ε.

The new turbulence model solves four differential equations of L, K, k, and ε, each representing the tumble, non-tumble mean kinetic energy, turbulent kinetic energy, and dissipation rate, respectively [49]:

$$\frac{dL}{dt} = \dot{L}_{in} - C_{out}L\frac{\dot{m}_{\text{out}}}{m} - \dot{L}_{\Psi} \tag{4.1}$$

$$\frac{dK}{dt} = (1 - C_\alpha)\frac{\dot{E}_{non}}{m} - K\frac{\dot{m}_{\text{out}}}{m} - P_k \tag{4.2}$$

$$\frac{dk}{dt} = C_\alpha\frac{\dot{E}_{\text{non}}}{m} - k\frac{\dot{m}_{\text{out}}}{m} + P_k - \varepsilon + \dot{k}_{\Psi} \tag{4.3}$$

$$\frac{d\varepsilon}{dt} = \frac{\varepsilon}{k}\frac{\dot{E}_{non}}{m} - \varepsilon\frac{\dot{m}_{out}}{m} + P_\varepsilon - 1.92\frac{\varepsilon^2}{k} + \frac{\varepsilon}{k}C_3\dot{k}_{\Psi} \tag{4.4}$$

The non-tumble MKE is treated as typical MKE in K-k models [34, 43], except

the fact that it is limited to the kinetic energy by the non-tumble velocity component $(\dot{E}_{non} = \sum \frac{1}{2} \dot{m}_i v_{eff,z,i}^2)$. The TKE production rate from non-tumble MKE and the corresponding term in the epsilon equation are:

$$P_k = C_\beta v_t \frac{2mK}{L_g^2} - \frac{2}{3} v_T \left(-\frac{\dot{\rho}}{\rho}\right)^2 - \frac{2}{3} k \left(-\frac{\dot{\rho}}{\rho}\right)$$

(4.5)

$$P_\varepsilon = \frac{\varepsilon}{k} \left[2.88 C_\beta v_T \frac{2mK}{L_g^2} - 0.88 v_t \left(-\frac{\dot{\rho}}{\rho}\right)^2 - 2k \left(-\frac{\dot{\rho}}{\rho}\right) \right]$$

(4.6)

Note that the coefficients in Eqs. 18 and 20 are from standard value for unidirectional compression with reference to [29].

As can be seen in Eqs. 15 to 20, there exist some modeling constants in addition to C_{KE}. The presence of any modeling constant involves calibration, any of which is not favored for a virtual engine. Hence, it is sought to eliminate calibration process by either assigning physical meaning to the coefficients or using a comprehensive value. As the basis for such a predictive model, the coefficients are designed as follows:

- C_{KE} is coefficient to take into account the flow velocity decrease as it passes the valve opening. Since the cause is interpreted to be the change of flow area, it may be correlated to the ratio of the valve curtain area to the cylinder bore area, as in [34]. This coefficient must be less than 1 because the velocity cannot be increased after expansion.

- C_α is the split factor of non-tumble intake kinetic energy between non-tumble MKE and the instantaneous TKE. The instantaneous TKE is interpreted as a consequence of significant shearing of inflow at valve opening [39, 43], so it seems plausible to express it as a function of valve

89

diameter and/or lift. As a split factor, it should lie between 0 and 1, as well.

- C_β is coefficient for the cascade rate of non-tumble MKE into TKE. It basically controls the residence time of the minor mean motion and the corresponding TKE production period. As it only comprises of minor mean motions, the cascade is presumed to be rather quick. Plus, since the extent of non-tumble MKE is dependent to C_α, the influence of C_β diminishes with the increase of C_α. Therefore, C_β can be considered as a subsidiary coefficient.

- C_3 is the coefficient of dissipation rate corresponding to tumble-generated TKE, which is newly added in the epsilon equation in our proposed model. This is adopted for structural consistency with the other terms in the standard k-ε model, so it is expected to also be universal, once specified. The coefficient for the non-tumble MKE term is 2.88 (Eq. 20), and the reasonable range for C_3 is supposed to be a similar order of magnitude.

- C_{out} is a multiplier of loss term caused by outgoing flow (e.g. back-flow into the intake port). This is applied particularly to the angular momentum because of the flow structure inside the cylinder. In case of a high tumble engine, it is unquestionable that flow in the outer side has greater velocity and the role of C_{out} is to compensate for the fact that outgoing mass has relatively higher velocity compared to the mass-averaged value. It would be possibly related to the boundary velocity and/or chamber dimension, which may affect the velocity gradient. A rough range of 1 to 5 seemed reasonable for this coefficient.

Figure 4.2 shows the results of tumble angular momentum L and turbulent intensity u' from ithe ndividual sweep of each modeling constant. Note that the

turbulent intensity is an indicator of the TKE because $u' = \sqrt{2k/3}$. A reasonable range has been set for each constant except for the C_β, which is tested with extreme range to demonstrate its insensitivity.

First, the effective flow velocity increases with greater C_{KE} as inferred in Eq. (2.9), which enhances the initial build-up rate of both angular momentum and turbulent intensity. The split factor C_α also affects the initial build-up of turbulent intensity, although it does not have a direct impact on the angular momentum. However, the enhanced TKE leads to an increase in turbulent viscosity ($= 0.09k^2/\varepsilon$), which in turn affects the tumble decay rate and reduces the overall angular momentum level. In addition, an insufficient TKE build-up was observed with C_α below 0.7. This sets the lower boundary of C_α, and the instantaneous TKE is within similar order of magnitude with that reported in other literature [39, 43] in terms of the fraction of total intake kinetic energy (including tumble component).

Next, smaller C_β value causes an increase of TKE level after the initial peak, but the effectiveness is relatively minor for the inputted value. It is also observed that C_β exerts negligible impact above a certain level, and this is because all of non-tumble MKE is cascaded immediately after being introduced. Both C_3 and C_{out} are related to TKE production from tumble decay, but C_3 adjusts the sensitivity of tumble decay, so it influences the TKE over the entire range where angular momentum exists. Meanwhile, C_{out} controls the amount of tumble angular momentum itself, and the height of second TKE peak is decided proportionally to the remaining tumble at IVC
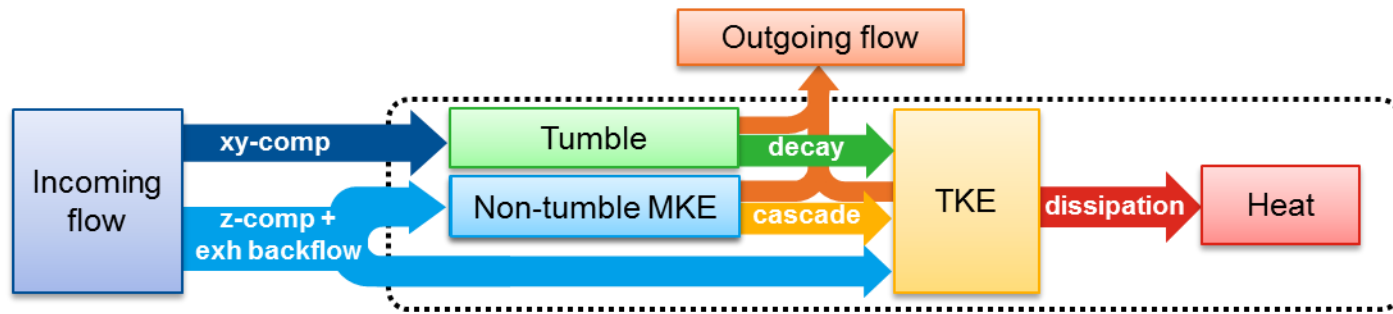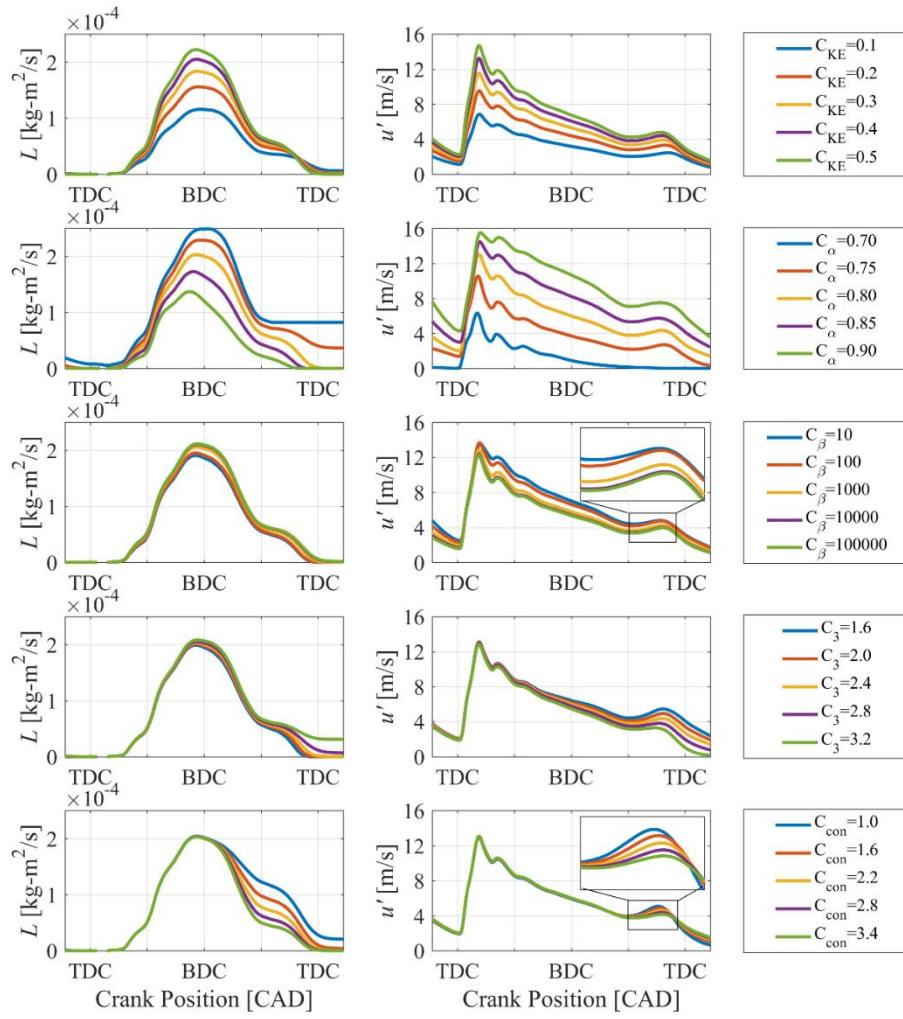
Figure 4.1 Flow chart of the new turbulence model

Figure 4.2 Results of tumble angular momentum and turbulent intensity under modeling constants sweep

4.2. Optimization of modeling constants

The five modeling constants were to be determined so that the developed model would correctly predict the tumble and turbulent intensity. The optimization of constants was carried out targeting to minimize the error between calculation results of the developed 0D model and 3D CFD, with the top priority at the turbulent intensity near the end of the compression process where the turbulence affects the flame propagation speed and thus engine performance. The CFD results reported in previous modeling study [49] cover variations in intake port geometry, engine speed and load, which makes them good reference data for model constants optimization.

The best modeling constants are found to be those listed in Table 4.1. Using this set of modeling constants, the 0D simulation has been performed with four different head designs (Head A, B, C, and C with valve masking). In Figure 4.3. the temporal traces of the normalized tumble angular momentum and the turbulent intensity are illustrated along with the results of transient CFD simulation. At the representative operating condition of 1600 rpm with an intake pressure of 0.55 bar, the prediction of the developed model was highly satisfactory, especially for the turbulent intensity near the end of compression. Therefore, it can be concluded that the suggested characterization method and the developed model together can successfully reflect the effect of design modifications including the top and bottom curvatures of intake port and valve masking. Moreover, each constant should be independent of changes in operating parameter such as engine speed, load, and cam timing shift, according to the physical meanings explained in section 4.1. Integration into the turbulence model., therefore, these optimized values in Table 4.1 are deemed as universal and used throughout the rest of this study.
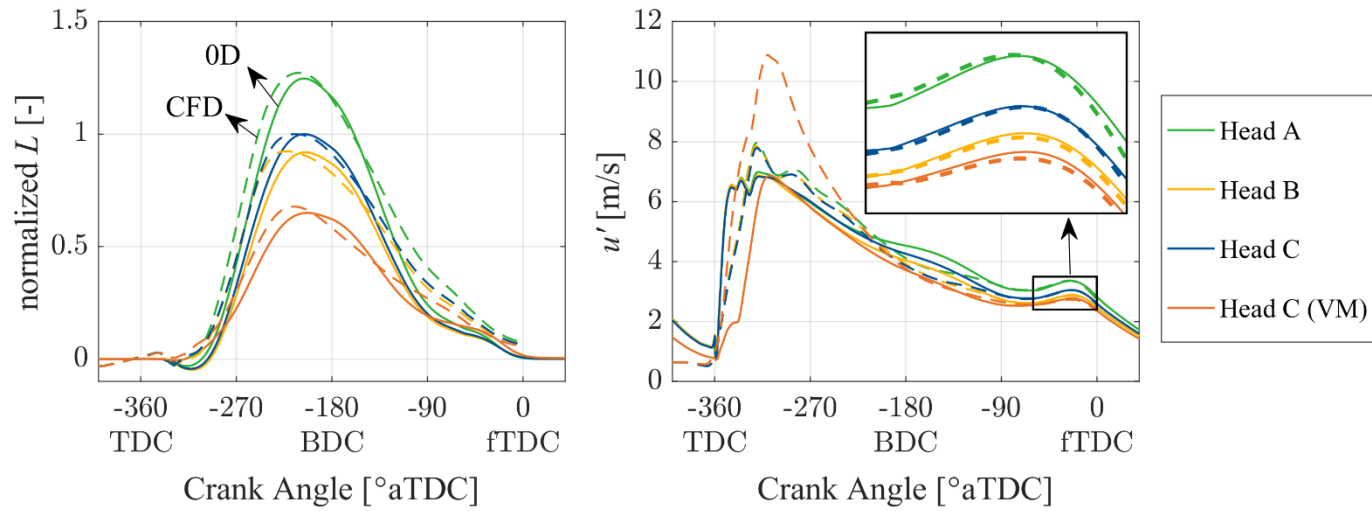
Figure 4.3 Results of calibrated 0D model compared with 3D CFD: Normalized tumble angular momentum (left) and turbulent intensity (right)

Table 4.1 Modeling constants calibrated for reference data of [15]

C_{KE}	0.5
C_α	0.8273
C_β	500
C_3	1.8125
C_{out}	3.5

4.3. Validation with experimental data

A comparative analysis with the experimental data has been planned to validate the predictability of the developed model. The experimental data of Oh [50] was chosen for the validation because their experiments cover not only a variety of operating parameters including engine speed, load, and intake/exhaust valve timing but also different port and chamber geometries. The three engines tested in this study have different stroke-to-bore ratios while displacement volumes and compression ratio kept equivalent. In addition, the same cylinder head is shared for Engines II and III, while Engine I has different head (i.e. port) geometry. More details on engine specifications and operating conditions are listed in Table 4.2 and Table 4.3.

4.3.1. 1D model setup

The 1D model of the single-cylinder engine is constructed in GT-Power as shown in Figure 4.4 using the dimensions of the target engine and its components. The cam phase shift, which can be critical in tumble calculation, is adjusted for the exact valve timing by using the cam position sensor signal. The newly developed turbulence model is converted to Fortran code, which is then integrated into the GT-Power model as a customized user code. The information on discharge coefficient, flow distribution, and flow angles obtained through characterization is retrieved from an external file. For the modeling constants in the turbulence model, the values of the reference engine in Table 4.1 are used consistently.

4.3.2. Validation method

The simulation was carried out to reproduce a total of 194 cases of experimental results. Figure 4.5 shows the comparison of 50% burn duration calculated by the developed model with that measured from the experiment.

Although the model prediction appears to follow the right trend, the accuracy is not quite satisfactory, with an R-square value of 0.6655. However, such poor correlation does not necessarily imply the model prediction was inaccurate. This study specifically aims to predict the flow dynamics during engine cycle rather than the consequent combustion behavior, thus, any further development and/or precise calibration of combustion model, other than the minimal calibration of the built-in combustion model of GT-Power, is deemed to be beyond the research scope. The inaccuracy of the combustion model possibly is the major cause of low agreement, and another validation approach was considered to validate the calculated turbulent intensity with no direct involvement of the combustion model.

Higher turbulent intensity is interpreted to enhance wrinkling of the flame sheet, thus the flame propagation speed. Since the flame propagation speed is the flame travel distance divided by the burn duration, the measured burn duration and calculated turbulent intensity would possibly be correlated. The relationship between turbulent flame speed (S_T) and turbulent intensity can be described with a general formula of:

$$\frac{S_T}{S_L} = 1 + C\left(\frac{u}{S_L}\right)^n \tag{4.7}$$

In order to approximate the average turbulent flame speed for a span of interest,

the corresponding flame travel distance and burn duration is necessary, but the flame travel distance (R_f) is not easily measurable in practice. Therefore, a rough estimation was to be made to quantify the flame travel distance, and it is implemented by utilizing the flame radius calculated from GT-Power. Figure 4.6 (left) depicts the temporal history of the relative flame radius (R_f/R) of each of all tested cases. As the operating conditions, including ignition timing, differ among the cases, the graph shows quite diverse flame radius profiles. But if the same relative radii are plotted over a fraction of burned mass (MFB), all profiles nearly collapse regardless of operating conditions as seen in Figure 4.6 (right). Taking the average suggests the flame radii at 10, 50, and 90 percent burn angles (CA10, CA50, and CA90) to be $0.538R$, $0.876R$, and $1.019R$, respectively.

Next, a reasonable range for validation was needed to be determined. It is well-known that flame kernels initially show laminar-like development, and gradually reach to fully-developed turbulent flame over a certain time scale. This infers that the turbulence does not wholly participate during this early stage of the combustion process, and makes it inappropriate to be used for validation of turbulence prediction. In the case of a later stage of combustion, the combustion can be disturbed by the expansion of cylinder volume, especially under high engine speed or slow-burn conditions. Therefore, the range for validation is somewhat arbitrarily chosen to be between 10 and 50 percent burn angles (CA10-50), and the Eq. (4.7) then becomes:

$$\frac{S_{T,1050}}{S_{L,1050}} = \frac{(R_{f,50} - R_{f,10})/\text{BD}1050}{S_{L,1050}} = 1 + C \left(\frac{u'_{1050}}{S_{L,1050}}\right)^n \qquad (4.8)$$

where the subscript 1050 indicates the average value of simulation result of over the same CA10-50 range. Then, the indirect validation according to Eq. (4.8) was

implemented to verify the correlation between calculated turbulent intensity and measured burn duration.

4.3.3. Results

The scatter plots of the dimensionless turbulent flame speed (S_T/S_L) and the dimensionless turbulent intensity $(u´/S_L)$ in Figure 4.7 summarize the validation results of Engines I, II and III. All 194 data points could adequately be described by a single curve with the C and n of 8.983 and 0.6405, respectively, with a much stronger correlation (R-squared value of 0.8328) than the direct comparison of burn duration in Figure 4.5. This verifies that the developed model with fixed modeling constants is fairly adaptive to changes in the chamber and head geometry as well as various types of engine operating conditions including engine speed, load, and valve actuation.

The improved correlation, on the other hand, evidences that the combustion model is erroneous. It should be noted that, despite the effort of the indirect comparison method, the overall validation results still are influenced by the combustion model because the combustion process is determinative to pressure, temperature, and consequently the laminar flame speed. Among others, the high RMF operation demonstrated the lowest accuracy in prediction. With no external EGR employed, the amount of burned gas in cylinder at IVC is determined majorly by the valve overlap. In the simulation results, a combination of long overlap duration and low load condition caused excessive RMFs near 30%, which would have caused inaccurate laminar flame speed. The gray 'x' markers in Figure 4.8

indicates data points with RMF above 25%, and just by excluding these 13 points, the R-squared value could be improved from 0.8328 to 0.8605. This infers that the variance of the scatter plot could be further alleviated by improving the combustion model.

4.3.4. Data analysis

In this section, it was examined what kind of physics were able to be captured by the model to predict the turbulence characteristics that correlate well with the experimental data. For this in-depth analysis, the effects of variations in engine speed, load, intake/exhaust valve shift, and engine geometry were analyzed individually.

<u>Effect of engine speed (4.5bar)</u>

Figure 4.9 shows the simulation results of two engine speed at fixed conditions of load and valve timings. The total mass flow rate through the intake valve and the intake/exhaust valve profiles are included in the plot on the top-left corner. Though there exists some difference in the pulsation, the final trapped mass was calculated to be equivalent. The plots on the bottom-left and top-right corners are the angular momentum and turbulent intensity, respectively. Since the velocity of incoming flow has a higher velocity at higher RPM, the tumble and turbulence intensity revealed proportional behavior to the engine speed. The asterisk symbol on the turbulent intensity plot indicates the ignition timing. From the fact that the ignition occurred near the peak of the turbulent intensity, it can be inferred that these sample cases made good use of the induced turbulence. Lastly, the plot on bottom-right is the same scatter plot as Figure 4.7 of only the interested data points. Due to the stronger tumble

at high engine speed, the corresponding turbulent intensity was computed to be increased with engine speed, which shows an adequate correlation with the flame speed estimated from the measured burn duration.

Effect of engine load (2000RPM)

Figure 4.10 illustrates the result of engine load sweep with the other conditions fixed. One major difference caused by load variation is gas exchange behavior. Around -360 CAD, where the valve overlap occurs, the greater negative flow rate is observed for lower load despite the same valve timing. This is because in part-load conditions, the intake charge is throttled to match the target engine load, thus the intake pressure is dropped below the atmospheric pressure. Consequently, the pressure difference between intake and exhaust manifold increases, which may lead to a greater amount of burned gas in the exhaust manifold to be reversed into the intake manifold during the valve overlap. Such backflow during the overlap is termed as "hot backflow" throughout the discussions. The hot backflow also caused the initial development of turbulent intensity, but not much impact on the angular momentum is observed because the cylinder mass at this time is fairly small.

Having a greater in-cylinder pressure, thus density, the higher load case loses more charge from the IVC being quite after the BDC. This reverse flow of fresh mixture into the intake manifold is termed as "cold backflow." The cold backflow evidently causes the loss in turbulent intensity and angular momentum between BDC and IVC, and this causes the smaller turbulent intensity peak near the ignition.

In this particular case, the peak turbulent intensity is observed to be the highest at the lowest load. The major reason was observed to be the initial turbulence build-up during the valve overlap. As the main inflow is introduced into a highly turbulent

environment, the tumble undergoes a more intensive shear than in the quiescent environment because of the greater turbulent viscosity. Although the breakdown of the greater remaining tumble strength in the higher load case caused a sharper increase of turbulent intensity near the ignition, it was not sufficient to reverse the result.

It is also noteworthy that the spark timing was retarded in the higher load cases due to the knock. Although a similar level of turbulence was achievable, the higher load could utilize only a part of that potential.

Effect of IV shift (low load)

Figure 4.11 shows the results of intake valve timing (IVT) sweep with fixed engine speed, load, and exhaust valve timing at 2000 rpm, GMEP 4.5bar, and -308 degrees aTDC, respectively. As IVT is advanced, the valve overlap is prolonged, which causes greater hot backflow. Since the valve duration is fixed, the IVT advance also causes earlier IVC, resulting in cold backflow decrease. Hence the combined effect of longer valve overlap and earlier IVC should be considered.

As in the load sweep simulation, the hot backflow causes initial turbulence build-up, which is observed to be greater for longer overlap cases. Also, the earlier IVC traps more angular momentum generated during the intake process and produces greater turbulence during the tumble breakdown stage. Combined, the turbulence intensity was calculated to be the highest at the earliest IVT.

Another important consequence of the longer valve overlap is the change in the composition of the in-cylinder charge. When a greater amount of burned gas in exhaust manifold flows reversely to the intake manifold, more burned gas happens to be included in the fresh mixture at IVC (also known as internal EGR). The residual

103

mass fraction (RMF) is the measure that indicates the comprised burned gas, and higher RMF slows down the laminar flame speed and lengthens the combustion duration. But if there is sufficient turbulence available to compensate for the effect of reduced laminar flame speed, the equivalent burn rates can be achieved. In consistence with this, a higher turbulent intensity level was calculated for the longer valve overlap, which explains how the tested cases could have a similar 50% burn angle (CA50). This demonstrates that the model adequately predicted the turbulent intensity that is needed for the high RMF mixture to have equivalent burn rate.

Effect of IV shift (high load)

In higher load condition, the overall trend by IVT shift changes as the occurrence of hot backflow diminishes. But the cold backflow still is sensitively dependent on the IVT shift, and the IVT advance caused greater tumble at IVC, thus greater increase of TKE near firing TDC (see Figure 4.12). Another difference was the initial build-up rate of turbulence at the beginning of the intake process. For the retarded IVT, the valve lift was relatively small, and this means a smaller valve curtain area. With comparable incoming mass flow rate, the velocity becomes faster for the smaller flow area, and this seems to cause greater turbulence build-up. This higher level of turbulence, however, was not sufficient to exceed the effect of stronger tumble breakdown. In addition, this benefits of turbulence in advanced IVT case was not very effective in the combustion process as the difference at peak attenuates as it gets to the knock-limited spark timing.

Effect of EV shift (low load)

Next is the effect of exhaust valve timing (EVT) shift. As EVT is retarded and

104

valve overlap is increased, a larger initial turbulence rise occurs as in the IVT shift (Figure 4.13). However, since the IVO timing is the same here, this initial rise starts at the same point, and for a longer period of time in retarded EVT. As the actual intake process starts at a later timing, the retarded EVT case showed slightly higher intake flow rate to meet the pressure equilibrium, and thus the tumble formation was slightly higher as well. However, there was no significant difference in IVC because higher tumble accompanies a higher tumble decay rate and greater loss due to the outflow. The secondary rise of turbulent intensity due to the tumble breakdown and compressibility effect was similar, and higher turbulent intensities were observed in the high overlap case where the initial formation was high.

Effect of EV shift (high load)

At higher load, the EVT shift did not have major sensitivities because there was not much hot backflow involved due to high intake pressure as shown in Figure 4.14. Except for the initial rise timing, the temporal turbulent intensity showed no significant difference with each other. The RMF also was calculated to be very low due to minimal hot backflow, and so the scatter showed almost coinciding points for EVT shift at high load condition.

Effect of engine geometry

Finally, the effect of engine geometry is examined. Having a comparable volume profile, the three tested engines showed no significant difference in intake mass flow rate, except for intermittent fluctuations by flow pulsation (see Figure 4.15). Despite the equivalent mass flow rate, a higher tumble generation rate is computed for the Engine III. This is because Engine III has the largest stroke-to-bore

ratio among three, thus the longest tumble moment arm. Subsequently, the more tumble-generated TKE is produced for Engine III, causing a higher mid-range turbulence level between -300 and -90. In addition, it can be seen that the tumble breakdown timing and its slope differs among the engines. This is mainly the effect of cylinder height. The velocity field inside the smaller but higher combustion chamber of Engine III causes a more gradual velocity gradient and causes the turbulence peak timing to be delayed.
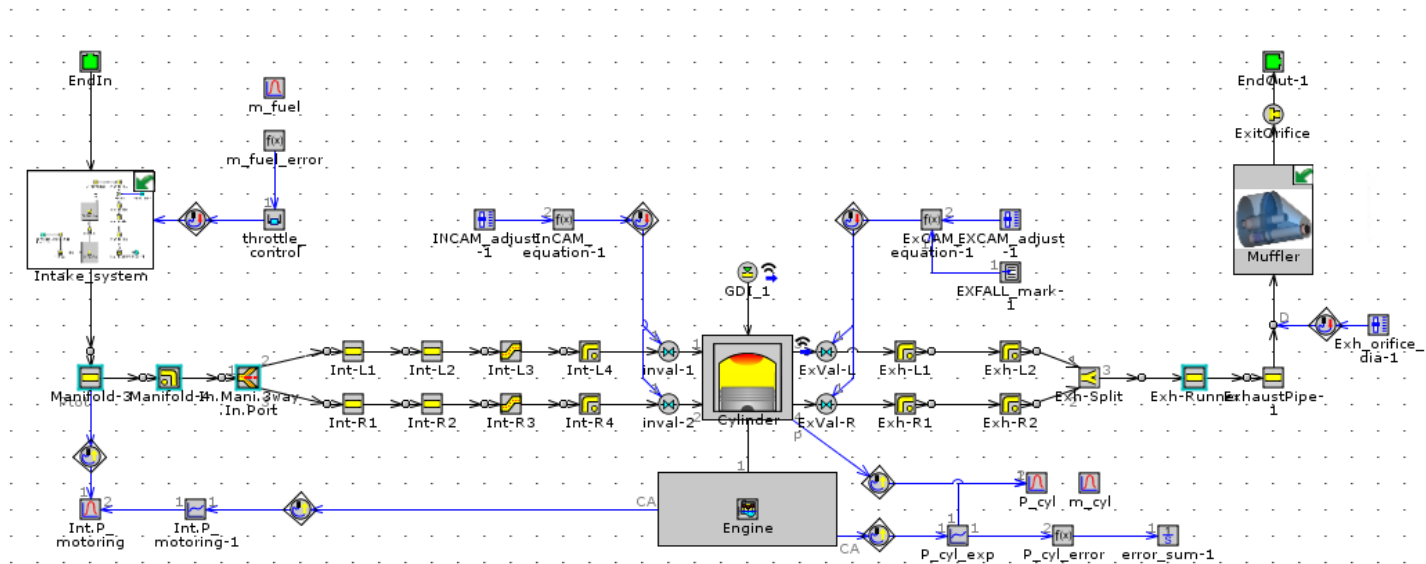
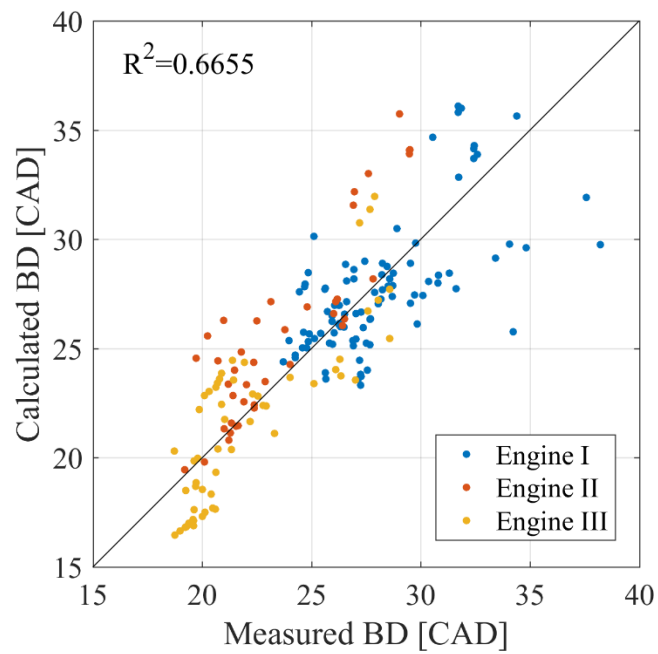Figure 4.4 GT-Power model for single-cylinder engine

Figure 4.5 Measured and calculated duration between ignition and 50% burn angle (BD0050)
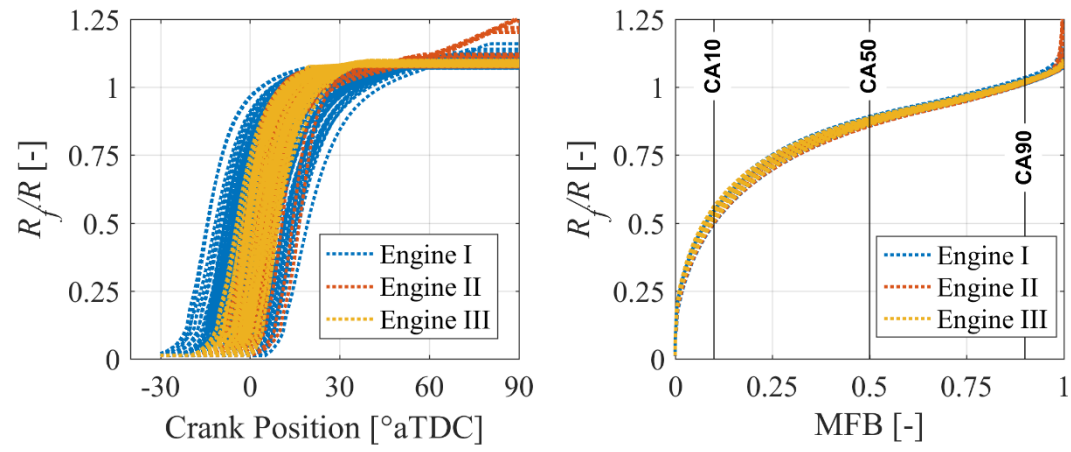
Figure 4.6 Development of flame radius
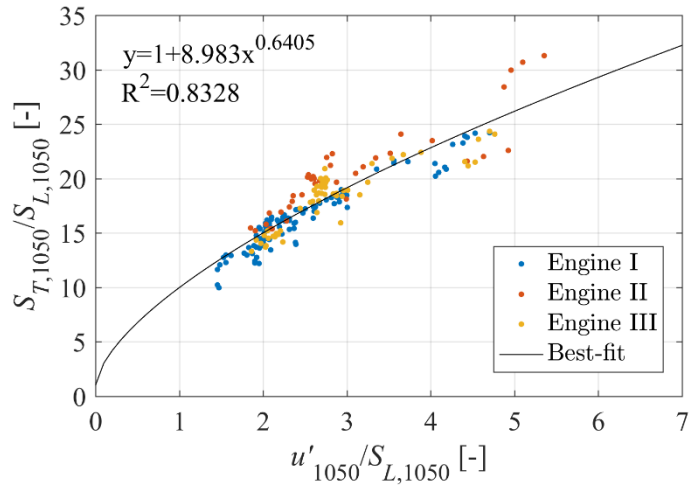
Figure 4.7 Correlation between simulation and experiment results (Engines I, II, and III)
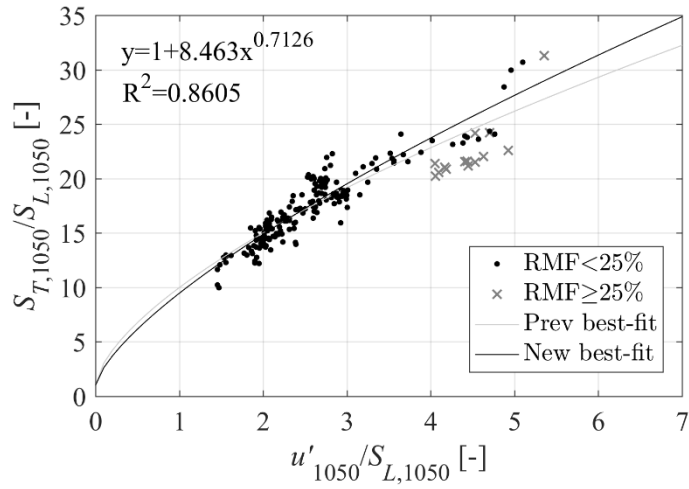
Figure 4.8 Correlation between simulation and experiment results (Engines I, II, and III, high RMF cases excluded)
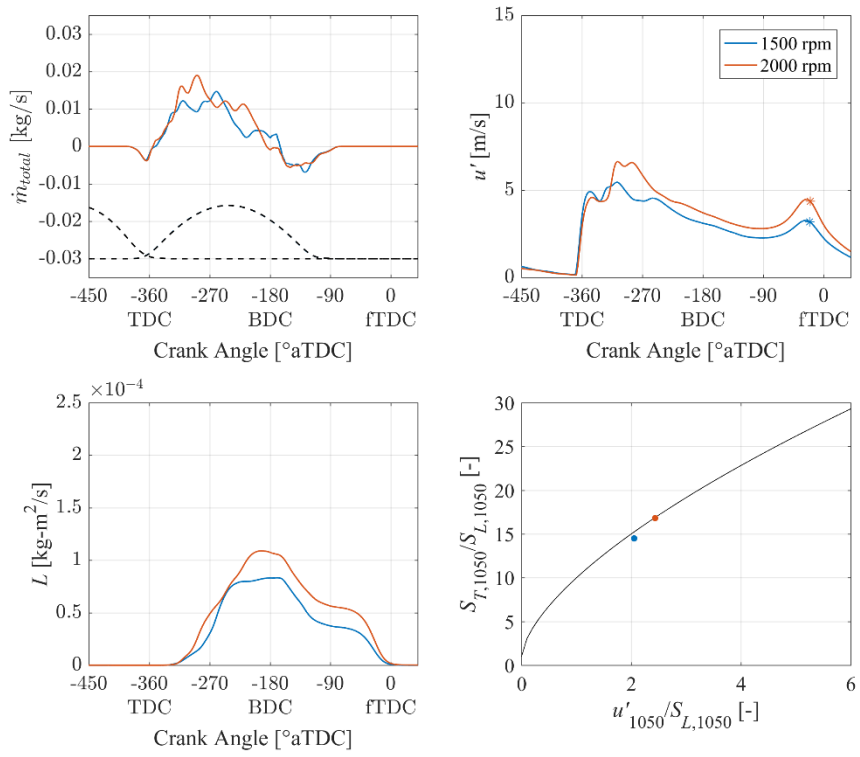
Figure 4.9 Simulation results with RPM variation (GMEP 4.5 bar)

111
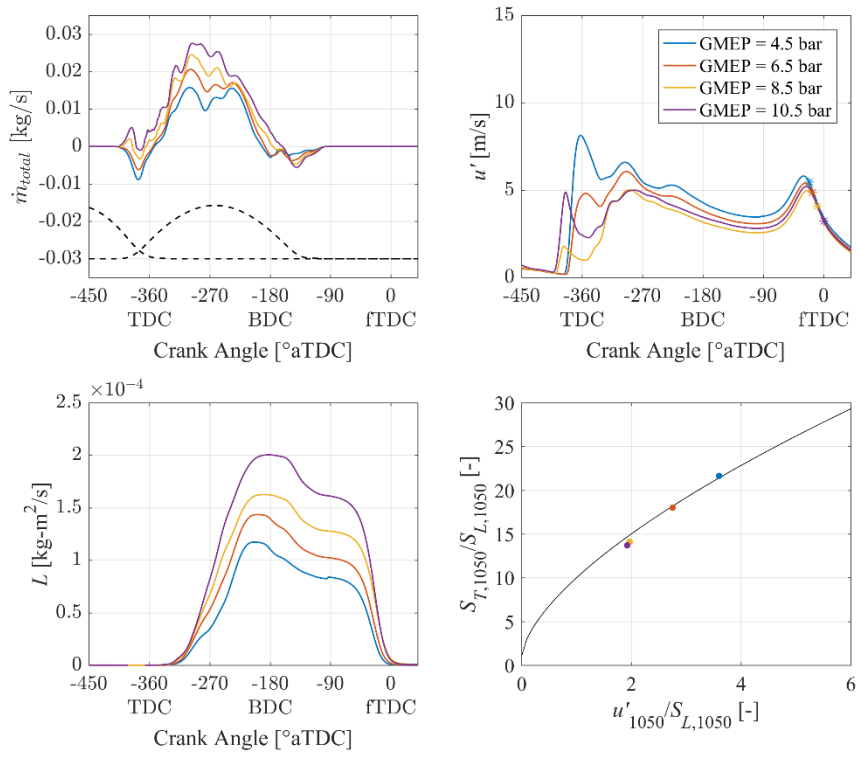
Figure 4.10 Simulation results with load variation (2000 RPM)
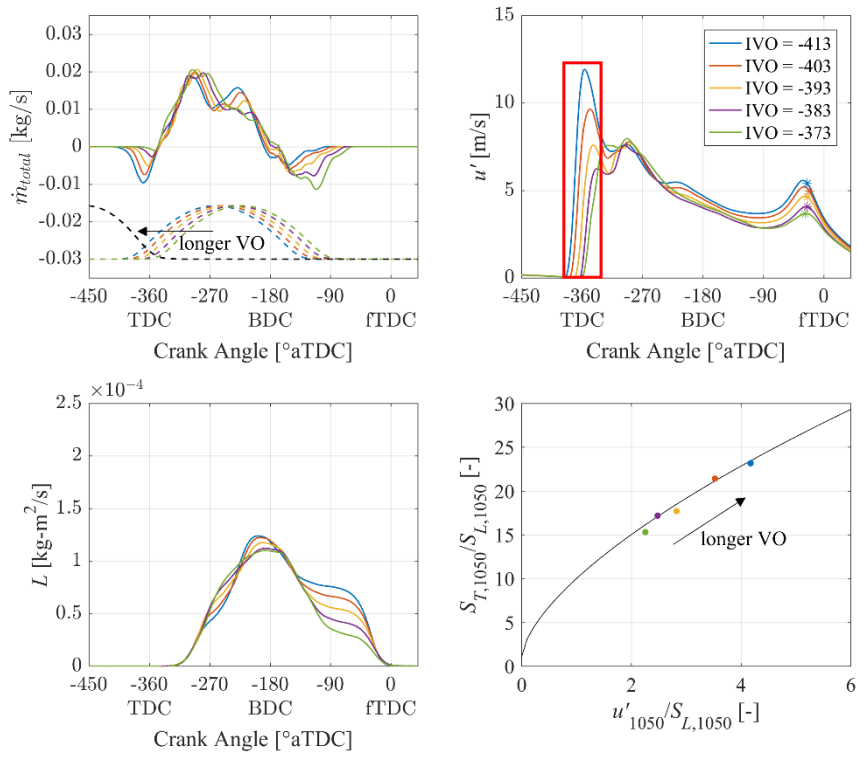
Figure 4.11 Simulation results with intake valve timing variation (GMEP 4.5 bar)

113
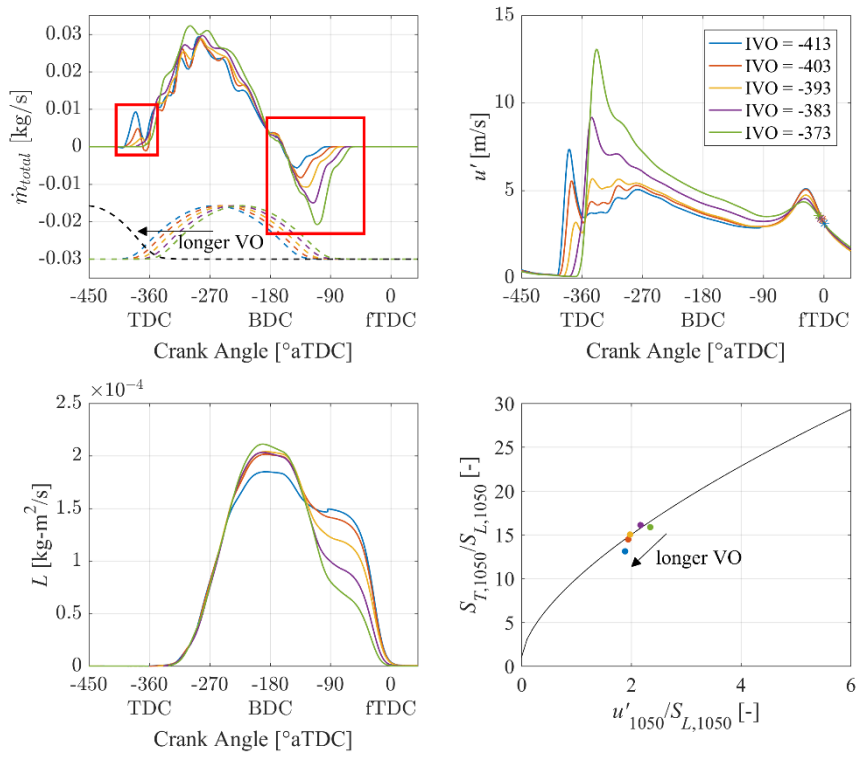
Figure 4.12 Simulation results with intake valve timing variation (GMEP 10.5 bar)
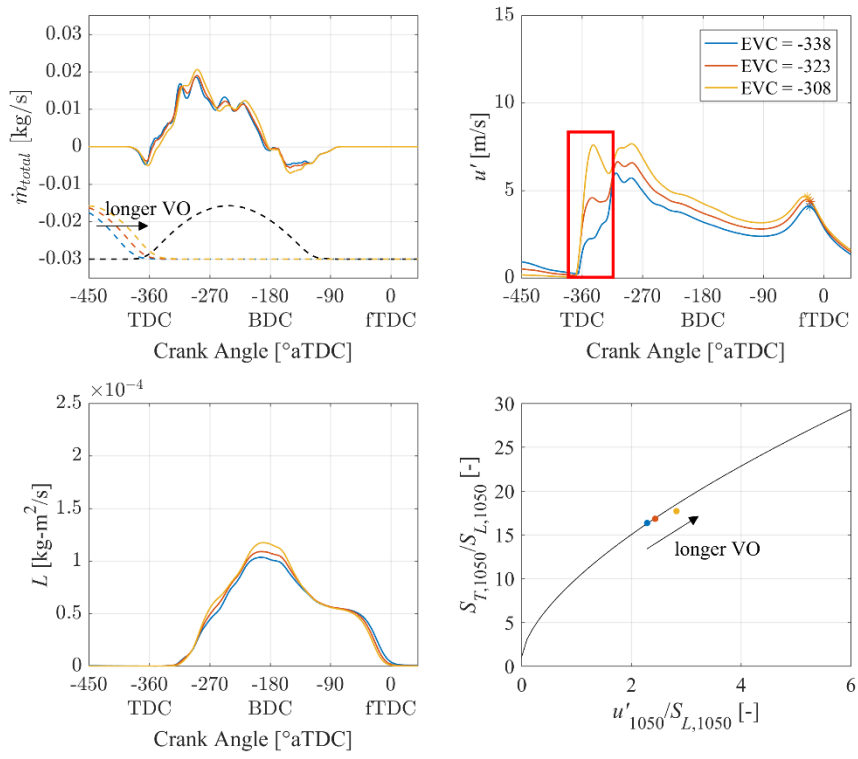
Figure 4.13 Simulation results with exhaust valve timing variation (GMEP 4.5 bar)
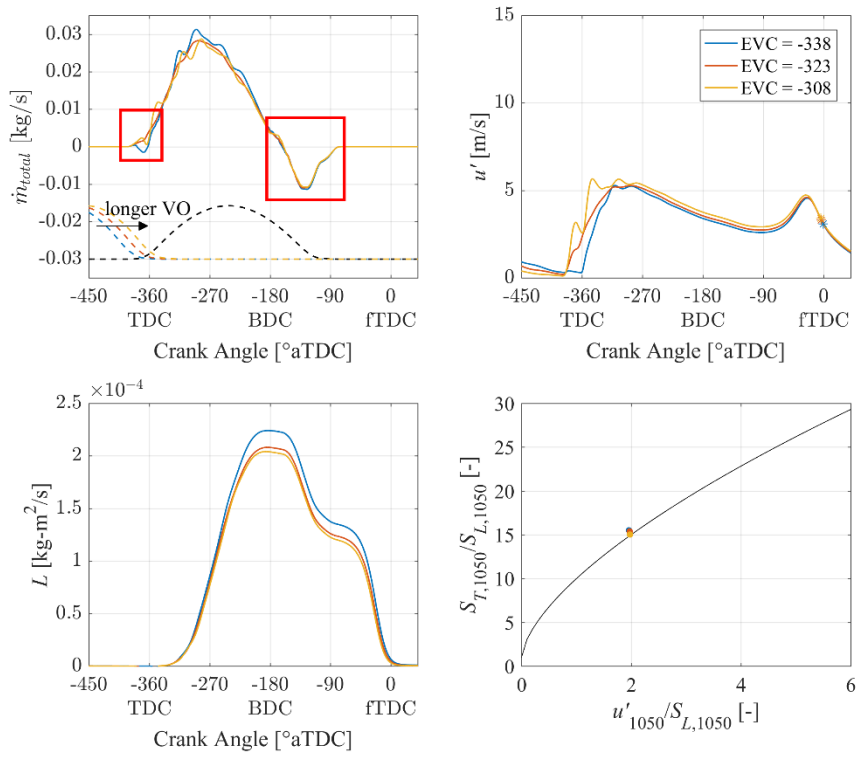
Figure 4.14 Simulation results with exhaust valve timing variation (GMEP 10.5 bar)
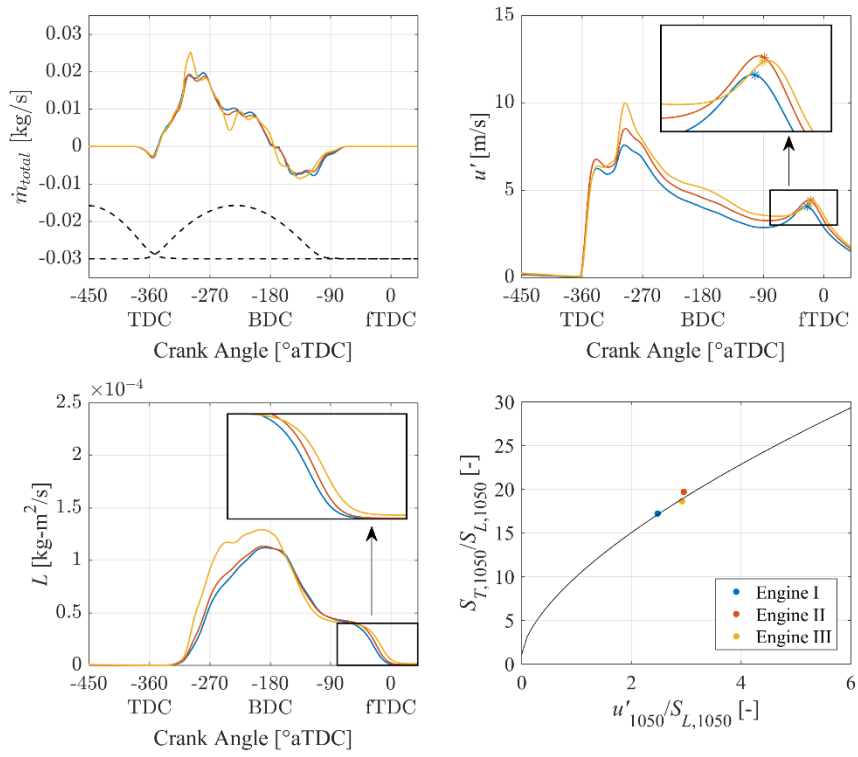
Figure 4.15 Simulation results with engine geometry variation (2000 RPM, GMEP 4.5 bar)

Table 4.2 Engine specifications

|	Engine I	Engine II	Engine III
Displacement [cc]	499.56	499.84	498.26
Bore [mm]	86	81	75.6
Stroke [mm]	86	97	111
Stroke-to-bore ratio	1.0	1.2	1.47
Connecting rod length [mm]	211.65	207.65	199.15
Compression ratio	12 ± 0.1		
Intake valve diameter [mm]	33	29	29
Exhaust valve diameter [mm]	33	27	27
Pentroof angle [degree]	15		

Table 4.3 Experimental conditions

Engine speed [rpm]	1500, 2000
GMEP [bar]	4.5, 6.5, 8.5, 10.5 (supercharged)
Valve open duration (In/Ex) [CAD]	280/240
InCam shift range [CAD]	-40 – 0(default*)
ExCam shift range [CAD]	0(default) – 30
Valve overlap [CAD]	35 – 105

* default valve timing: Intake valve open at 10 CAD before TDC, exhaust valve close at 1 CAD after TDC.

Chapter 5. Model Application

The most straightforward way of utilizing the developed model would be to predict the performance of certain engine design. Since the validation results suggest that the model can sufficiently predict the tumble and turbulent intensities at various operating points, one can use it to examine the performance behavior of a particular engine under varying operating conditions or investigate on the effect of design modifications on the final performance. The only requirement in this process is then to supplement the characterization results to the developed model, which is attainable given the CAD geometry as described in section 2.2. Head characterization Therefore, using this model, the engine design can be evaluated without the actual engine fabrication and testing or the time-consuming 3D simulations.

Taking one step further, some guidelines for the design stage can be suggested based on the trends of characterization results with a variation in design parameters. Since there can be numerous design parameters that affect the intake valve flow dynamics, it is quite difficult to examine or predict each of their influence individually. The characterization results, however, already reflects all impacts of major and minor design aspects combined. Thus, a few repetitions of the characterization method can offer comprehensive guidelines for determining the suitable design for particular objectives.

As one example, the intake port design variation with two design parameters of top and bottom curvatures is demonstrated. In addition to the Heads A, B, and C, which are previously introduced in section 2.2. Head characterization, the characterization is performed for three additional heads with different combinations

119

of top and bottom curvatures. The description of these additional heads (D, E, and F) are listed in Table 5.1, and again, the curvature is expressed in the same arbitrary measure, in which the positive value implies outward (convex) curvature. The six characterization results were then scattered on the axis of design parameters, which could further be produced as a contour map. Figure 5.1 and Figure 5.2 are the contour maps of total discharge coefficient and the fraction of uppermost mass flow rate, both at the valve lift of 8 mm.

As shown in Figure 2.17 and Figure 2.18, both discharge coefficient and the fraction of mass flow rate show quite linear relation with the valve lift beyond about 2 mm. This implies that these two contour maps can be considered to represent the general flow characteristics by engine design variation. These contour maps are not only comprehensive but they also provide great insight. At a glance, one can easily apprehend that the negative top curvature and positive bottom curvature are beneficial in concentrating more flow toward the upper side, thus create stronger tumble motion, but there follows the corresponding drop in discharge coefficient, i.e. charging efficiency.

Moreover, it is noteworthy that the borderlines of the two contour maps do not exactly coincide. This indicates that even among the curvature combinations with the equivalent discharge coefficient, there exist the one that generates stronger tumble flow. For instance, Heads B and C have equivalent discharge coefficient characteristics, but Head C is favorable for stronger tumble generation as it yields slightly higher flow concentration toward the upper side. Likewise, Heads C and F yield comparable flow concentration, but Head C is advantageous over Head D in terms of discharge coefficient. As seen here, these contour maps provide very

120

practical and intuitive insights for the engine designers. It is quite encouraging that such an effective tool described so far can be obtainable with no experiment or simulation but only a simple characterization process using CAD geometry of the head design.

Given a more specific engine geometry and operating conditions, further simulation can be carried on using the developed model and the contour map of the calculation results can be provided over the same domain. Figure 5.3 and Figure 5.4 illustrates the peak tumble momentum and turbulent intensity at firing TDC, respectively, at the condition of 1600 rpm and intake pressure of 1 bar. These calculation results are based on the characterization results in Figure 5.1 and Figure 5.2, and the other design parameters are kept consistent as listed in Table 2.1. It is easily observable that the tumble strength in Figure 5.3 shows very similar trends with the mass fraction through the uppermost area, and this confirms the close correlation between the tumble strength and the flow concentration. The turbulent intensity as well showed a similar trend overall, but some differences existed due to the combined effect of other factors that affecting TKE production other than tumble motion.

Generally speaking, the geometry of the engine components is determined at the manufacturing stage and unchangeable. However, the optimal geometry for the greatest performance may vary depending on the operating conditions. Thus, it is necessary to consider which range the engine would be mainly operated in and to select a design that gives the best performance in the interested region. Figure 5.5 shows the turbulent intensity results for different engine speed and intake pressure

121

conditions. This type of data can be very helpful in the engine designing stage as it summarizes the prediction on flow dynamic behavior of each design parameter combination at different operating conditions.

At the current status, the final results are presented as the turbulent intensities at TDC, a particular point in time. However, such results may not be very sufficient to represent the engine performance because (1) there can be quite a difference between the TDC timing and the critical timing for combustion process, namely the spark timing, depending on the operating condition, and (2) the turbulent intensity is one of many factors that determines the final performance of the engine. Thus, possible improvements definitely exist as higher turbulent intensity does not necessarily mean better engine performance. If the appropriate combustion model is integrated in the future, it would be available to provide a more intuitive reference data that shows how each design parameter would affect the performance-related parameters such as combustion speed, heat loss, thermal efficiency, and fuel consumption. Once such an achievement is reached, the model is expected to suggest the optimal engine design to fit the objectives of either a hybrid vehicle with the limited engine operating range or an internal combustion engine vehicle with a wide operating range.

Figure 5.1 Effect of intake port curvature combinations: Contour map of discharge coefficient (valve lift = 8mm, 1600 rpm, P_{int} = 0.55 bar)
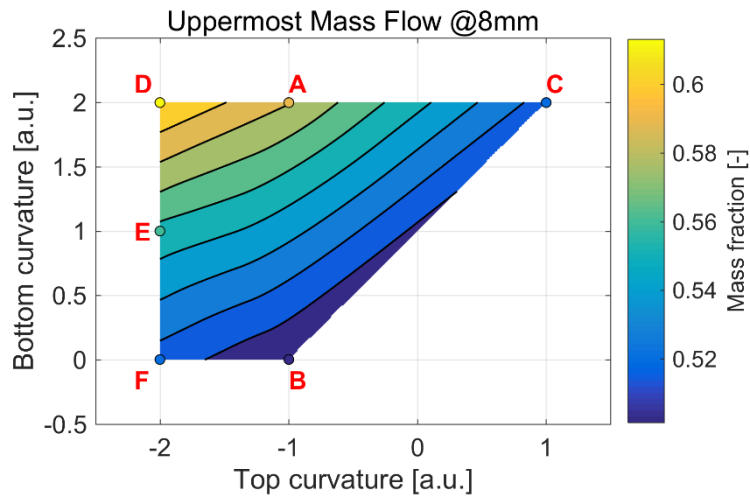
Figure 5.2 Effect of intake port curvature combinations: Contour map of intake mass fraction via uppermost area (valve lift = 8mm, 1600 rpm, Pint = 0.55 bar)
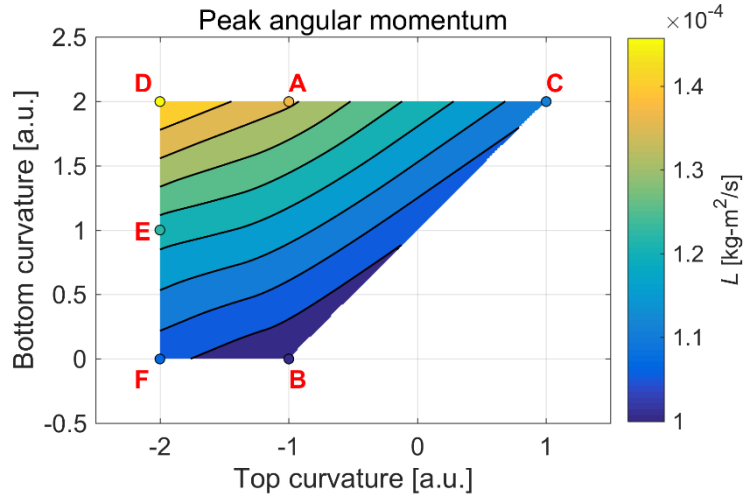
Figure 5.3 Effect of intake port curvature combinations: Contour map of peak tumble strength (valve lift = 8mm, 1600 rpm, P_{int} = 0.55 bar)
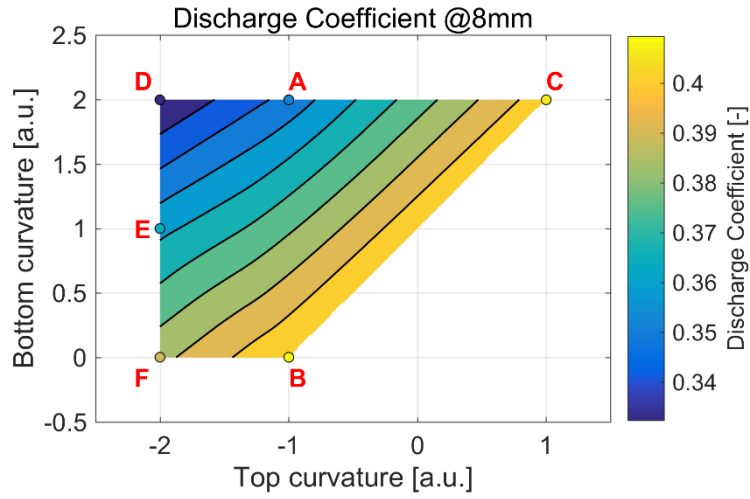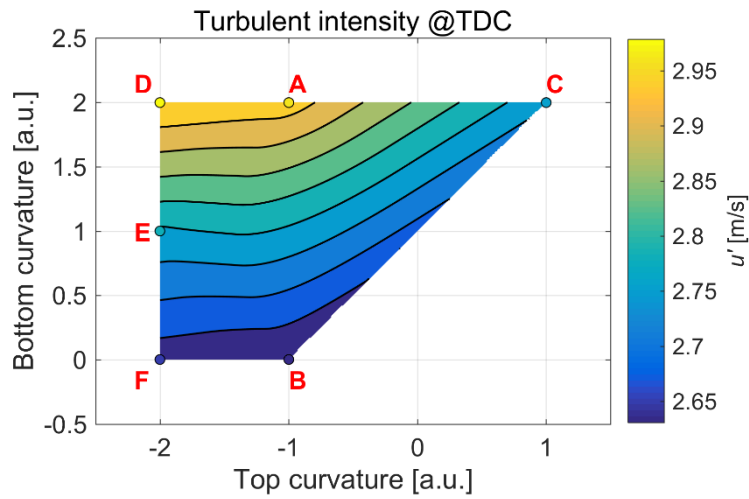

Figure 5.4 Effect of intake port curvature combinations: Contour map of turbulent intensity (valve lift = 8mm, 1600 rpm, P_{int} = 0.55 bar)
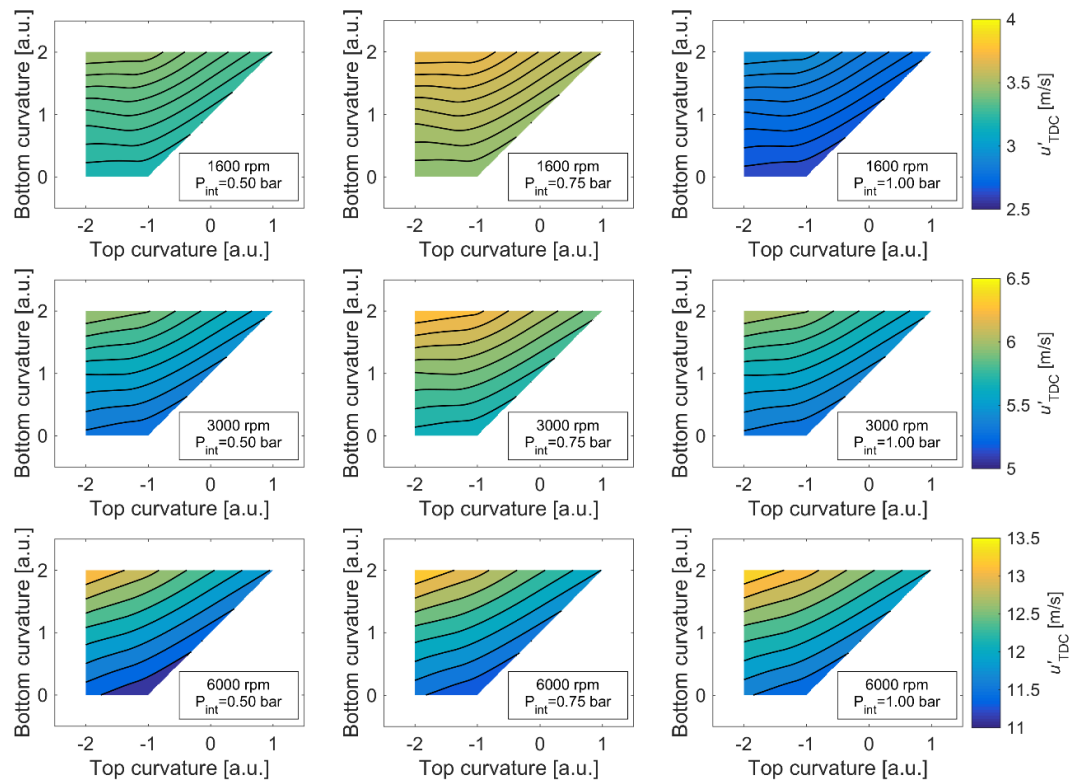
Figure 5.5 Results of calibrated 0D model compared with 3D CFD: Normalized tumble angular momentum (left) and turbulent intensity (right)

Table 5.1 Design specifications of additional heads

Head ID	Top curvature [a.u.]*	Bottom curvature [a.u.]
D	-2	2
E	-2	1
F	-2	0

* arbitrary unit. a positive value indicates curved outwardly (convex) and a negative

value indicates curved inwardly (concave)

Chapter 6. Conclusion

6.1. Conclusion

As an effort to develop a calibration-free predictive 0D tumble/turbulence model, a new physics-based approach is proposed based on phenomenological investigations on the tumble flow.

First, the generation of the tumble motion is modeled with consideration of the detailed valve flow structure. In summary, to complete this new tumble generation model,

- the valve curtain area is subdivided into multiple divisions, by which the intake flow in different directions could be considered

- the detailed information on the valve flow structure, including the discharge coefficient, the flow distribution, and the flow angles, is acquired by simple steady-state CFD simulations. It was confirmed that these are intrinsic characteristics of the head design and expressed as a function of only valve lift.

- the total and divisional flow rates could be calculated using the discharge coefficient and flow distribution. This approach was shown to predict flow rates of accuracy comparable to 3D CFD under variations of port curvatures and valve masking.

- the new formula for tumble generation rate is proposed, reflecting the individual effect of each division. The pentroof geometry is taken into account in addition to the divisional mass flow rates, and no adjustable

constant is included.

Next, the decay of tumble into the turbulence is modeled to consider the tumble structure:

- the flow field is assumed within the pentroof chamber, and the velocity profile is modified to be closer to the real situation
- the production of turbulent kinetic energy by internal shear is calculated and connected with the tumble decay rate. The formula of tumble decay rate is also free of adjustable constants.

Finally, the developed model is integrated with the 0D turbulence model and its predictability is validated:

- the validation with 3D CFD proves the developed model can correctly respond to the effect of the geometry variations
- the validation with experimental data implies the developed model properly captures the core physics and predicts the turbulence under the combined effect of engine design, engine speed, load, and valve timings

The final validation results verify the predictability of the new turbulence model, thus its potential as a part of a virtual engine. Moreover, it could be glimpsed possible improvements in the reliability of the model with the further advancement of other elements, which will be discussed in the following section.

6.2. Future work

In the current study, the predictive 0D engine model that can reflect the flow structure has been developed. The validation was performed to verify the functionality of the model, but it was only a preliminary level limited to the effect of the intake port, head, and cylinder design on the tumble and turbulent intensity. Therefore, there still remain various possibilities for further improvements.

One is to consider the effect of the piston geometry. The piston bowl geometry can influence (1) the conservative force of the tumble motion, (2) the center location of tumble vortex, and (3) the flame area over time, therefore the burn rate and heat transfer rate. In addition, the effect of squish, which also is determined according to the piston geometry, cannot be neglected in particular cases. The developed model currently assumes flat piston, and it is therefore encouraged that the consideration of piston geometry to be added.

The direct injection of the fuel is another factor that should be considered in the model because direct injection of gasoline, namely GDi, is quite commonly accepted in the modern SI engines and can cause significant impacts on tumble and turbulence behavior. Various injector characteristics (such as hole size, number of holes, cone angle, etc.) will be the key parameters when modeling its effect. In precedent studies, the effect of direct injection has been modeled by directly adding a source term in the TKE equation [40] or by calculating the amount of tumble generation based on considering the angle and position of the injector with respect to the tumble center [32], and with a similar approach, it is believed that the current model can be improved to reflect the GDi effects.

Another possible consideration for improvement is the detailed tumble center

location. One of the biggest assumptions of the current model is that the tumble center is deemed to be at the geometric center. This can cause a meaningful error in calculations of both the generation and the decay of the tumble motion. If it is possible to predict the tumble center location to some extent, either by 3D CFD simulation or experiments using an optically-accessible engine, it would possibly be applied to the 0D model. Nevertheless, in order to implement the moving tumble center in the calculation, a new approach may be required since the simple velocity profile proposed in section 3.1 would no longer be utilizable.

Finally, the most promising improvement would be the development and integration of a suitable predictive combustion model. If a highly accurate prediction on the combustion characteristics becomes available, the 0D model will ultimately be completed and allow the performance prediction with only given the CAD model, which can then be extended for development/testing of control logic or even the virtual engine calibration.

Bibliography

[1] Ritchie H, Roser M. CO_2 and other greenhouse gas emissions. 2018.

[2] Elgowainy A, Han J, Ward J, Joseck F, Gohlke D, Lindauer A, et al. Current and Future United States Light-Duty Vehicle Pathways: Cradle-to-Grave Lifecycle Greenhouse Gas Emissions and Economic Assessment. Environmental Science & Technology, 2018; 52: pp. 2392-9.

[3] Choi W, Yoo E, Jang JJ, Seol E, Song HH. Well-to-wheel greenhouse gas emissions of current (2017) and future (2030) passenger vehicle pathways: A South Korean Case study. Applied Energy Symposium: MIT A+B (AEAB2019)2019.

[4] Yang Z, Bandivadekar A. Light-duty vehicle greenhouse gas and fuel economy standards. 2017.

[5] Heywood J, MacKenzie D, Akerlind I, Bastani P, Berry I, Bhatt K, et al. On the road toward 2050: Potential for substantial reductions in light-duty vehicle energy use and greenhouse gas emissions. 2015.

[6] Light-Duty Automotive Technology, Carbon Dioxide Emissions, and Fuel Economy Trends Report: 1975 Through 2017. United States Environmental Protection Agency (EPA), 2018.

[7] Feneley AJ, Pesiridis A, Andwari AM. Variable geometry turbocharger technologies for exhaust energy recovery and boosting-A Review. Renewable Sustainable Energy Reviews, 2017; 71: pp. 959-75.

[8] Juergen G. Powertrain Development Trends to Meet Next Global Standards. AUTO JOURNAL : Journal of the Korean Society of Automotive Engineers, 2014; 36: pp. 41-4.

[9] Takemura S, Aoyama S, Sugiyama T, Nohara T, Moteki K, Nakamura M, et al. A study of a continuous variable valve event and lift (VEL) system. 2001: pp. 118-25.

[10] Cleary D, Silvas G. Unthrottled engine operation with variable intake valve lift, duration, and timing. SAE Technical Paper, 2007.

[11] Flierl R, Lauer F, Breuer M, Hannibal W. Cylinder deactivation with mechanically fully variable valve train. 2012; 5: pp. 207-15.

[12] Hirooka H, Mori S, Shimizu R. Effects of High Turbulence Flow on Knock Characteristics. SAE transactions, 2004: pp. 651-9.

[13] Berntsson AW, Josefsson G, Ekdahl R, Ogink R, Grandin B. The Effect of Tumble Flow on Efficiency for a Direct Injected Turbocharged Downsized Gasoline Engine. SAE International Journal of Engines, 2011; 4: pp. 2298-311.

[14] Ogink R, Babajimopoulos A. Investigating the Limits of Charge Motion and Combustion Duration in a High-Tumble Spark-Ignited Direct-Injection Engine. SAE International Journal of Engines, 2016; 9.

[15] Wheeler J, Polovina D, Ramanathan S, Roth K, Manning D, Stein J. Increasing EGR Tolerance using High Tumble in a Modern GTDI Engine for Improved Low-Speed Performance. SAE Technical Paper, 2013.

[16] Scheidt M, Brands C, Kratzsch M, Günther M, Combined Miller/Atkinson strategy for future downsizing concepts. 2014; 75: pp. 4-11.

[17] Kent J, Haghgooie M, Mikulec A, Davis G, Tabaczynski R. Effects of intake port design and valve lift on in-cylinder flow and burnrate. SAE Technical Paper1987.

[18] Achuth M, Mehta PS. Predictions of Tumble and Turbulence in Four-Valve Pentroof Spark Ignition Engines. International Journal of Engine Research,

2001; 2: pp. 209-27.

[19] Bozza F, Teodosio L, De Bellis V, Fontanesi S, Iorio A. Refinement of a 0D Turbulence Model to Predict Tumble and Turbulent Intensity in SI Engines. Part II: Model Concept, Validation and Discussion. SAE Technical Paper Series2018.

[20] Yoshihara Y, Nakata K, Takahashi D, Omura T, Ota A. Development of High Tumble Intake-Port for High Thermal Efficiency Engines. SAE Technical Paper2016.

[21] Heywood JB. Internal Combustion Engine Fundamentals. 1988.

[22] Ikeya K, Takazawa M, Yamada T, Park S, Tagishi R. Thermal Efficiency Enhancement of a Gasoline Engine. SAE International Journal of Engines, 2015; 8.

[23] Blizard NC, Keck JC. Experimental and theoretical investigation of turbulent burning model for internal combustion engines. SAE Technical Paper, 1974.

[24] Keck JC. Turbulent flame structure and speed in spark-ignition engines. Symposium (International) on Combustion. Elsevier1982. pp. 1451-66.

[25] Tabaczynski RJ, Ferguson CR, Radhakrishnan KJSt. A turbulent entrainment model for spark-ignition engine combustion. 1977: pp. 2414-33.

[26] Tabaczynski RJ, Trinker FH, Shannon BAJC, Flame. Further refinement and validation of a turbulent flame propagation model for spark-ignition engines. 1980; 39: pp. 111-21.

[27] Poulous S. The effect of combustion chamber geometry on SI engine combustion rates. MIT1982.

[28] Borgnakke C, Arpaci VS, Tabaczynski RJ. A model for the instantaneous heat transfer and turbulence in a spark ignition engine. SAE Technical Paper, 1980.

[29] Morel T, Mansour N. Modeling of turbulence in internal combustion engines. SAE Technical Paper1982.

[30] Mansouri SH, Heywood JB, Radhakrishnan KJST. Divided-Chamber Diesel Engine, Part I: A Cycle-Simulation which predicts performance and emissions. 1982: pp. 1101-32.

[31] Bozza F, Fontana G, Galloni E, Torella E. 3D-1D analyses of the turbulent flow field, burning speed and knock occurrence in a turbocharged SI engine. SAE Technical Paper, 2007.

[32] Dulbecco A, Richard S, Laget O, Aubret P. Development of a Quasi-Dimensional Kk Turbulence Model for Direct Injection Spark Ignition (DISI) Engines Based on the Formal Reduction of a 3D CFD Approach. SAE Technical Paper, 2016.

[33] Kim N. A Study on Phenomenological Quasi-Dimensional Combustion Modeling of Spark-Ignited Engine. 서울대학교 대학원, 2016.

[34] Kim N, Ko I, Min K. Development of a zero-dimensional turbulence model for a spark ignition engine. International Journal of Engine Research, 2018.

[35] Benjamin S. Prediction of barrel swirl and turbulence in reciprocating engines using a phenomenological model. Experimental Predictive Methods in Engine Research Development, 1993.

[36] Dai W, Newman CE, Davis GC. Predictions of in-cylinder tumble flow and combustion in SI engines with a quasi-dimensional model. SAE transactions, 1996: pp. 2014-25.

[37] Ramajo D, Zanotti A, Nigro N. Assessment of a zero-dimensional model of tumble in four-valve high performance engine. International Journal of Numerical Methods for Heat & Fluid Flow, 2007; 17: pp. 770-87.

[38] Falfari S, Forte C, Brusiani F, Bianchi GM, Cazzoli G, Catellani C. Development of a 0D Model Starting from Different RANS CFD Tumble Flow Fields in Order to Predict the Turbulence Evolution at Ignition Timing. SAE Technical Paper Series2014.

[39] Grasreiner S, Neumann J, Luttermann C, Wensing M, Hasse C. A quasi-dimensional model of turbulence and global charge motion for spark ignition engines with fully variable valvetrains. International Journal of Engine Research, 2014; 15: pp. 805-16.

[40] Grasreiner S. Combustion Modeling for Virtual SI Engine Calibration with the Help of 0D 3D methods. 2012.

[41] Grasreiner S, Neumann J, Wensing M, Hasse C. A Quasi-Dimensional Model of the Ignition Delay for Combustion Modeling in Spark-Ignition Engines. Journal of Engineering for Gas Turbines and Power, 2014; 137.

[42] Grasreiner S, Neumann J, Wensing M, Hasse C. Model-based virtual engine calibration with the help of phenomenological methods for spark-ignited engines. Applied Thermal Engineering, 2017; 121: pp. 190-9.

[43] Fogla N, Bybee M, Mirzaeian M, Millo F, Wahiduzzaman S. Development of a K-k-ε Phenomenological Model to Predict In-Cylinder Turbulence. SAE International Journal of Engines, 2017; 10: pp. 562-75.

[44] Bozza F, De Bellis V, Berni F, D'Adamo A, Maresca L. Refinement of a 0D Turbulence Model to Predict Tumble and Turbulent Intensity in SI Engines. Part I: 3D Analyses. SAE Technical Paper Series2018.

[45] Kent J, Mikulec A, Rimal L, Adamczyk A, Mueller S, Stein R, et al. Observations on the effects of intake-generated swirl and tumble on combustion duration. SAE Transactions, 1989: pp. 2042-53.

[46] Yang Q, Grill M, Bargende M. A Quasi-Dimensional Charge Motion and Turbulence Model for Diesel Engines with a Fully Variable Valve Train. SAE Technical Paper, 2018.

[47] Kim M, Kim Y, Song HH. Development of Zero-Dimensional Spark Ignition Engine Model Considering Turbulence Formation in Various Intake Pressure Conditions and Intake Manifold Designs. The 56th KOSCO Symposium2018.

[48] Hadded O, Denbratt I. Turbulence characteristics of tumbling air motion in four-valve SI engines and their correlation with combustion parameters. SAE Technical Paper1991.

[49] Kim Y, Kim M, Kim J, Song HH, Park Y, Han D. Predicting the Influences of Intake Port Geometry on the Tumble Generation and Turbulence Characteristics by Zero-Dimensional Spark Ignition Engine Model. SAE Technical Paper2018.

[50] Oh S, Cho S, Seol E, Song C, Shin W, Min K, et al. An Experimental Study on the Effect of Stroke-to-Bore Ratio of Atkinson DISI Engines with Variable Valve Timing. J SAE International Journal of Engines, 2018; 11.

국문 초록

해를 거듭하며 강화되고 있는 내연기관 자동차에 대한 연비 규제에 대응하기 위해 지속적인 신기술 개발이 다방면으로 이루어지고 있다. 이러한 신기술들이 최대 효용으로 엔진에 적용되기 위해서는 각 운전 조건에서의 구동 전략은 물론 그에 맞는 엔진 형상 설계도 최적화가 이루어져야 한다. 이렇게 다양한 기술이 연루된 최적화 작업을 실험적으로 수행하기에는 지나치게 많은 시간과 노력이 소요되며, 실용적인 최적화를 위해서는 시뮬레이션의 활용이 필수적이다. 1차원 시뮬레이션 모델은 전반적인 엔진 시스템 구동을 빠른 계산속도로 분석할 수 있는 툴이기 때문에 이러한 최적화 작업에 적합하다. 하지만 엔진 성능을 좌우하는 실린더 내부 현상에 대한 모사는 대개 보정계수에 의존하는 0차원 모델을 통해 이루어지게 되며, 이는 보정작업 없이는 특정 엔진에 대한 분석을 수행하기 어렵기 때문에 미개발 엔진에 대한 예측에는 활용될 수 없다는 단점이 있다.

0차원 모델이 예측력을 갖기 위해서는 한층 물리적인 접근방법을 통해 실린더 내부 현상과 관련된 물리를 반영할 수 있도록 개선되어야 한다. 그 중에서도 난류 특성은 불꽃점화 엔진에서 화염전파속도와 열전달률, 연료 혼합 등에 결정적인 영향을 미치기 때문에 모델이 정확한 성능을 예측하기 위해서는 반드시 잡아내야 하는 아주 주요한 요인이다. 최근에는 난류 강화에 용이한 텀블의 활용이 보편화 되는 추세이며, 이러한 텀블 유동은 엔진의 형상과 구동 전략 모두에 의해

민감하게 달라질 수 있기 때문에 이를 잘 예측할 수 있는 모델에 대한 필요성이 분명하게 존재한다.

따라서 본 연구에서는 엔진의 형상 및 구동 전략에 따른 텀블 유동과 그에 따른 난류 특성을 보정 계수 없이도 예측할 수 있는 0차원 모델의 개발을 목표로 하였다. 우선 흡기가 실린더 내로 유입되며 텀블 유동을 형성하는 과정에 대해 분석하여 텀블 형성 모델을 개발하였다. 기존 모델에서는 총 흡기유량에 대해 텀블 계수를 적용함으로써 텀블 강도를 추산하였지만, 이러한 텀블 계수를 얻기 위해서는 유동 측정실험이 요구되었다. 이 연구에서는 밸브 유동이 특정 방향으로 집중될 때 더 강력한 텀블이 형성된다는 점을 반영함으로써 텀블 계수를 대체하고자 하였다. 특정 실린더 헤드 형상을 특성화 할 수 있는 정상상태 3차원 전산유체해석 방법을 제안하였으며, 이로부터 얻은 밸브 유동 특성을 0차원 모델에 적용함으로써 여러 방향의 밸브 유동이 텀블 형성에 미치는 개별적인 영향을 고려할 수 있도록 하였다. 이렇게 형성된 텀블이 난류로 변환되는 현상에 대해서 역시 보정 계수를 이용하여 텀블의 감쇄율을 조정하는 것이 아닌, 주어진 연소실 형상에서의 속도 유동장을 가정하고 그 때 내부전단에 의해 발생하는 난류 생성량을 텀블 감쇄와 결부 짓는 방법을 택하였다. 실제의 실린더 내 유동구조를 더 정확하게 모사하는 유동장을 제시하였으며, 한층 현실적인 연소실 형상을 반영하도록 모델을 개선하였다.

이렇게 개발된 텀블 모델은 $k-\varepsilon$ 난류모델과 결합되어 최종적인 0차원 난류모델을 완성하였으며, 이 모델은 한 차례의 교정 시 다양한

운전 조건 및 엔진 형상에 대해서 3차원 모델에 준하는 예측을 할 수 있다는 것이 확인되었다. 추가적으로 실험결과와의 검증도 수행되었으며, 다양한 엔진 형상과 속도, 부하 및 밸브 타이밍에 대한 총 194개의 실험점들에 대해 모델 예측 난류값과 실험 측정 연소주기의 상관관계를 하나의 피팅곡선으로 충분히 표현할 수 있음을 확인하였다.

이 연구의 최종적인 결과물은 핵심 물리를 담은 실용적인 모델로서 형상 변화에 따른 성능 예측을 통해 설계 최적화를 도우며, 나아가서는 가상엔진의 일부로 자리매김할 수 있을 것으로 기대된다.